# ELECTROMAGNETIC FORMING AND PERFORATION OF TUBES

*A Thesis Submitted in Partial Fulfillment of the*

*Requirements for the Degree of*

**DOCTOR OF PHILOSOPHY**

*Submitted by*

**Sagar Hanamant Pawar**

**(Roll No. 166103021)**

DEPARTMENT OF MECHANICAL ENGINEERING
INDIAN INSTITUTE OF TECHNOLOGY GUWAHATI,
GUWAHATI - 781039, ASSAM, INDIA.
JAN 2021

भारतीय प्रौद्योगिकी संस्थान गुवाहाटी
Indian Institute of Technology Guwahati

Dedicated to

***My parents***

*Mr. Hanamant Narayan Pawar,*

*Mrs. Kamal Patil-Pawar*

*&*

***My beautiful wife***

*Dr. Rutuja Chavan-Pawar*

for their **SUPPORT**, **LOVE** and **PATIENCE**

DEPARTMENT OF MECHANICAL ENGINEERING
INDIAN INSTITUTE OF TECHNOLOGY GUWAHATI
GUWAHATI 781039, ASSAM, INDIA

# DECLARATION

I hereby declare that the information presented in the dissertation "**Electromagnetic Forming and Perforation of Tubes**" is entirely my own account of research performed under the guidance of Prof. Sachin D. Kore and Dr. Arup Nandy. Any part of this work has not earlier been submitted for the award of any degree, diploma, associate-ship, fellowship or its equivalent to any University or Institution. I have not violated any copyright and plagiarism law. All text and figures are my own.

Date:

**Sagar Hanamant Pawar**
Roll No. 166103021
Department of Mechanical Engineering
Indian Institute of Technology Guwahati,
Guwahati-781039, Assam,
India.

DEPARTMENT OF MECHANICAL ENGINEERING
INDIAN INSTITUTE OF TECHNOLOGY GUWAHATI
GUWAHATI 781039, ASSAM, INDIA

# CERTIFICATE

It is certified that the work contained in this thesis entitled "**Electromagnetic Forming and Perforation of Tubes**" submitted by **Mr. Sagar Hanamant Pawar to** the Indian Institute of Technology Guwahati for the award of the degree of Doctor of Philosophy has been carried out under our supervision in the Department of Mechanical Engineering, Indian Institute of Technology Guwahati. This work has not been submitted elsewhere for the award of any other degree or diploma.

Date:

**Prof. Sachin D. Kore**
**Professor**
School of Mechanical Sciences,
Indian Institute of Technology Goa,
Ponda–781039, Goa
India

**Dr. Arup Nandy**
**Assistant Professor**
Department of Mechanical Engineering,
Indian Institute of Technology Guwahati,
Guwahati- 781039, Assam,
India.

# Acknowledgments

It is a pleasure to express my thanks wholeheartedly to everyone who contributed to making my doctoral research work achievable. Before presenting my research work, I would like to take the opportunity to humbly acknowledge all of them for their constant support and guidance.

First and foremost, I would like to express my sincere gratitude to my supervisors Prof. Sachin D. Kore and Dr. Arup Nandy for their support and guidance during my Ph.D. study. Special thanks to Prof. Sachin D. Kore for showing tremendous confidence in me and was very patient, for which I shall always be indebted to him. His amazing skills of organization, planning and management thought me a lot. I feel fortunate to have him as a mentor of my thesis and I indeed appreciate his parental supervision. I would like to extend my thanks to Dr. Arup Nandy for his guidance and intellectual inputs during the completion of the research work. I would like to appreciate all his contributions, time and ideas to make my doctoral research productive and stimulating.

I would like to thank my doctoral committee members, Prof. S. Senthilvelan, Prof. R Ganesh Narayanan and Prof. Harshal B. Nemade for their valuable suggestions and encouragement during the period of my research work.

I also like to express my heartful gratitude to the Director, all Deans, and other management of IIT Guwahati whose collective efforts has made this institute a place for world-class studies and education. I am grateful to the former head of the Department of Mechanical Engineering, Prof. S. K. Dwivedy for extending various facilities during the tenure of my doctoral program. My sincere thanks to all members of the central workshop and mechanical department office staff for their help in conducting my experimental work and official requisite.

I am thankful to my seniors Dr. Chandrahas Patel, Dr. J. K Doley, Dr. Ashish Rajak, Dr. Ramesh Kumar, and Dr. Getu Tilahun Areda for stimulating discussions and motivating to overcome any problems either in work and otherwise. I express my sincere thanks to my lab mates Mr. Deepak Kumar, Mr. Avinish Tiwari, Mr. Sanjay Raj, Mr. Pradeep Pankaj, Mr. L N Dhara for brotherhood and all the fun we had.

My special appreciation goes to the Maharashtra Mandal IIT Guwahati fraternity and I am much obliged to my friends cum family Harshad, Ankush, Shweta, Sandesh and Hardika for all the cherish moments we had together.

Most importantly, none of this would have been possible without the love and patience of my family. I would like to thank my parents, Mr. Hanamant Pawar (Pappa) and Mrs. Kamal Pawar (Aai), for their unconditional love, support, and encouragement during my research work. I would like to thank all family members for encouragement, specially my brother, Mr. Manoj Pawar for his support and my sweet niece Meera for giving me a reason for a smile. I would also thanks to my in-laws Prof. Jyoti Chavan (Aai) and Prof. M. D. Chavan (Pappa) and brother-in-law Darshan (Dadu) for their love and guidance.

I would especially like to thank my dear wife, Dr. Rutuja Chavan-Pawar, who has stood by me through all my travails, my absences, my fits of pique, and impatience. She gave me support and help, discussed ideas and prevented several wrong turns. She also supported the family during much of my doctoral studies. Thank you for being my muse, editor, proofreader, and sounding board. But most of all, thank you for being my best friend. I owe you everything.

This thesis becomes a reality with the kind support and help of many individuals, I would like to extend my sincere thanks to all of them.

Finally, I bow my head to the God almighty in deepest gratitude and seek blessings.

**January 2021** **Sagar Hanamant Pawar**

# Abstract

Among different metal forming processes, the high strain rate forming is very challenging as it involves the application of high energy for a short duration of time, which enables to deform large size parts easily. In case of electromagnetic shearing it has advantage of reduced burrs and slivers. High strain rate deformation improves formability of the material. Electromagnetic forming (EMF) is a high strain rate forming process which utilizes electromagnetic forces to deform the metal workpieces such as sheets and tubes. Some of the researchers have found that the forces generated in the electromagnetic forming are higher enough to shear the material easily. Here in this work, a feasibility study on Electromagnetic forming and perforation (EMFP) of the tube technique has been carried out. In the conventional manufacturing of perforated tubes, the metal sheet is first perforated by blanking, then rolled and welded into the tube. This process is time-consuming as it involves multiple operations, and also it leads to some weld defects. To overcome this problem, a novel EMFP technique is developed where simultaneous expansion and perforation of the tube can be possible. This will result in near net shape product with faster rate of production. The optimum discharge energy is determined with experimental trials that lead to successful forming and perforation of the tube. Experimental results show that the concave punches are more suitable for perforation as complete removal of slug took place, which results in clear perforation.

For the comparison of conventional (low strain rate) and electromagnetic (high strain rate) shearing, a setup for quasi-static die-less perforation is developed, and experiments are carried out. Here, we have studied different sheared edge zones for EM as well as Quasistatic forming with both pointed and concave punches. The results obtained during this study show the capability of electromagnetic perforation to obtain perforated holes with better edge surface finish and material properties over the quasi-static perforation process.

Further, the experimental and numerical study on the electromagnetic forming of muffler tube with a die has been carried out. In traditional manufacturing techniques of muffler tubes, the metal sheet is formed by conventional practices, then it is rolled and welded into desired shape. The welded zone in the muffler tube is more brittle, and it has less fatigue strength, which may result in failure. In this part of work, experiments are carried out on Al6061 tubes, which results in a single piece of component of the desired shape (muffler), hence it eliminates the weld zone and the working life of muffler may extend. In conventional muffler the tube used is steel and it adds to the weight of automobile. Use of aluminium is difficult due to poorer formability at low strain rate. EM forming being high strain rate can form Al muffler tube and reduce the weight of the automobile. The FE analysis is carried out for both EM forming of muffler tube and EMFP process. The coupled and non-coupled simulation algorithms are developed and used for the FE analysis. Advanced techniques and meshing methods available in non-coupled simulation software's are used for more accuracy. In the case of FEA of EM forming of muffler tube, a coupled simulation method is used, and a good agreement with deformation obtained experimental results is observed. Optimum discharge energy is determined for maximum die filling for EM forming of the muffler tubes.

On the other hand, in the FEA of EMFP, both simulation methods are used. At lower discharge energy, the coupled model results are found in 96% agreement with diameter of perforated hole obtained in experimental results. While on the other side, at the same discharge energy, although the non-coupled simulation shows a 94% agreement, it has succeeded in better capturing of the initiation of perforation. Stress variations along the tube during forming and perforation are thoroughly studied for both type of punches. Also, the shearing mechanism and slug separation for punchless EM perforation is studied with FE simulations.

In general, the good agreement of FEA results with findings in the experiment shows the prediction capability of developed numerical models. Overall, the presented study concluded that the EM techniques are advantageous over conventional processes. Finally, by modifying the parameters as per requirement in this study, one can commercialize these applications of EM forming processes.

**Keywords:** Electromagnetic forming; Perforation; Muffler; Finite element analysis; Simulation; Modeling; High strain rate; Shearing

# Content

**Abstract** .... i

**Content** .... iii

**List of Figures** .... ix

**List of Tables** .... xvii

**1. Introduction** .... 1

1.1 Conventional Forming Process .... 1

1.2 High Energy Rate Forming Processes .... 1

1.2.1 Explosive Forming .... 2

1.2.2 Electro-Hydraulic Forming .... 2

1.2.3 Electromagnetic Forming (EMF) .... 3

1.3 Physics and Principle of Electromagnetic Forming Process .... 3

1.4 Advantages and Limitations of Electromagnetic Forming Process .... 7

**2. Literature Review** .... 9

2.1 Introduction .... 9

2.2 Electromagnetic Tube Forming .... 11

2.2.1 Electromagnetic Tube Expansion .... 12

2.2.2 Electromagnetic Tube Compression .... 14

2.3 Perforation of Tube .... 18

2.3.1 Conventional Manufacturing of Perforated Tubes .... 18

2.4 Experimental and FEM Study on High Strain Rate Perforation .... 19

2.4.1 FEM and Experimental Study on Perforation of Tubes .... 19

2.4.2 FEM and Experimental Study on Perforation of Sheets .... 20

2.4.3 Advantages of High Strain Rate Perforation .... 23

2.5 Failure Modes and Material Model .... 23

2.5.1 Failure Modes .... 23

2.5.2 Johnson-Cook Material Model .... 24

2.5.3 Failure Model .... 25

2.6 Motivation .... 26

2.7 Objectives of Work .... 27

2.8 Structure of Thesis .... 27

**3. Experimental Methodologies and Simulation Procedures** .... 29

3.1 Introduction .... 29

3.2 Experimental Methodology .... 29

3.2.1 Electromagnetic Forming Machine .... 29

3.2.2 Electromagnetic Forming and Perforation Setup and Working Principle .... 31

3.2.3 Electromagnetic Forming of Muffler Tube Setup and Working Principle .......33
3.2.4 Experiments on Quasi-Static Die-less Perforation of Tubes ...............................35
3.3 Simulation Models ........................................................................................ 36
3.3.1 Coupled Simulation Model ..................................................................37
3.3.2 Non-Coupled Simulation Model ..........................................................40
3.4 Properties of the Materials................................................................................ 43
3.5 Equipment for Post-Processing.......................................................................... 45
**4. Electromagnetic Forming and Perforation of Al Tubes: Experimental Study [I] ................ 49**
4.1 Introduction ........................................................................................ 49
4.2 Results and Discussions ................................................................................ 49
4.2.1 Micro Hardness Tests and SEM Examination ........................................57
4.3 Conclusion .............................................................................................. 59
**5. Comparison of Electromagnetic and with Quasi-Static Die-Less Perforation[II] ................ 61**
5.1 Introduction ........................................................................................ 61
5.2 Materials and Methods ................................................................................ 61
5.2.1 Materials..............................................................................................61
5.2.2 Experiments on EM and Quasi-Static Die-less Perforation of Al Tubes ...........62
5.3 Results and Discussion.................................................................................. 62
5.3.1 Comparison of EM Perforation with Quasi-Static Die-less Perforation............62
5.4 Conclusions.............................................................................................. 69
**6. EM Forming and Perforation of Tubes: Modeling, Simulation and Validation[III]............ 71**
6.1 Introduction ........................................................................................ 71
6.2 Methodology .............................................................................................. 71
6.2.1 Non-coupled Simulation.........................................................................71
6.2.2 Coupled Simulation................................................................................72
6.3 Results and Discussions ................................................................................ 72
6.3.1 Electromagnetic Forming and Perforation (EMFP) Experiments .....................72
6.4 Validation and Comparison .............................................................................. 72
6.4.1 Magnetic Pressure and Radial Displacement ...........................................72
6.4.2 Material Movement and Process Parameter Distribution.................................74
6.5 Conclusion .............................................................................................. 84
**7. FEA to Study the Shearing Mechanism in Punch-less EM Perforation of Aluminium Tubes[VI]..........................................................................................................85**
7.1 Introduction ........................................................................................ 85
7.2 Principle of Electromagnetic Punch-less Perforation.......................................... 85
7.3 FE Analysis of Electromagnetic Punchless Perforation of Aluminium Tubes........ 86
7.3.1 3D Electromagnetic Simulation using LS-DYNA...............................................87

7.4 Results and Discussion for EM Perforation ........ 88

7.4.1 Transient nonlinear numerical simulation of shearing mechanism involved during EM perforation ........ 90

7.4.2 Simulation of slug separation ........ 92

7.4.3 Results of Simulation of 2 mm Al6061 Tube ........ 94

7.5 Conclusion ........ 97

**8. FE and Experimental Analysis on EM Punchless Forming of Muffler$^{V}$ ........ 99**

8.1 Introduction ........ 99

8.2 Experimental Methodology ........ 100

8.2.1 Strain Measurement for Formability Analysis ........ 100

8.3 Finite Element Model ........ 100

8.3.1 Modeling of EM Forming of Muffler Setup ........ 100

8.4 Results and Discussion ........ 102

8.4.1 Effect of variation in the length of the coil ........ 102

8.4.2 Effect of Coil Position (along tube length) on Deformation Pattern ........ 104

8.4.3 Effect of Discharge Energy on Gap Filling ........ 107

8.4.4 Formability Analysis ........ 111

8.4.5 Influence of Discharge Energy on Major Strain and Minor Strain ........ 112

8.4.6 Effect of High Strain Rate Forming on the Hardness ........ 113

8.5 Conclusion ........ 113

**9. Conclusion and Scope of Future Work ........ 115**

9.1 Conclusion ........ 115

9.2 Future Work ........ 116

9.2.1 Electromagnetic Forming and Perforation ........ 116

9.2.2 Electromagnetic Forming of Muffler Tube ........ 116

**List of Publications ........ 119**

**References ........ 123**

# List of Figures

**Figure 1.01** Explosive forming 2

**Figure 1.02** Electrohydraulic forming 2

**Figure 1.03** (a) Electromagnetic forming of the tube and (b) Equivalent circuit diagrams 3

**Figure 2.01** Different coils for different application in EM forming process 9

**Figure 2.02** Energy transfer during electromagnetic forming 11

**Figure 2.03** (a) EM expansion and (b) EM compression of the tube 11

**Figure 2.04** (a) Use of field shaper for tube expansion and (b) Current directions 13

**Figure 2.05** (a) Conical, (b) Cylindrical, (c) Convex, (d) Concave 15

**Figure 2.06** Loose coupled and sequential coupled model 17

**Figure 2.07** Common failures occurring in projectile impact (a) Fracture due to initial stress wave, (b) Radial fracture, (c) Spall failure, (d) Petaling (Frontal), (e) Petaling (Rewarding), (f) Fragmentation, (g) Ductile hole enlargement and (h) Plugging 24

**Figure 3.01** Electromagnetic processing system (a) Oscilloscope, (b) Control unit, (c) EM forming machine and (d) Safety stick 31

**Figure 3.02** Inside of EM processing system 31

**Figure 3.03** Schematic representation of EM perforation of tube setup 32

**Figure 3.04** (a) M5 Allen screw, (b) Pointed punch, (c) Concave punch and (d) Punch geometries 32

**Figure 3.05** (a) Exploded assembly view, (b) Cross section of the setup 33

**Figure 3.06** Die (a) Top view, (b) Front view and (c) Setup ready for the experiment 33

**Figure 3.07** Schematic representation of EMF of tractor muffler setup 34

**Figure 3.08** Muffler (All dimensions are in mm) 34

**Figure 3.09** EM forming setup model (a)3D model, (b) Front view, (c) Cross section side view 35

**Figure 3.10** (a) Die, (b) Setup prepared for the experiment 35

**Figure 3.11** Coils 36

**Figure 3.12** Quasi-static die-less perforation setup, (a) Model and, (b) Experimental setup 37

**Figure 3.13** Current curve obtained at 5.0 kJ discharge energy 38

**Figure 3.14** Coupled behavior in LS-DYNATM 39

**Figure 3.15** Different simulation zones in the coupled simulation process 39

**Figure 3.16** Cross-section views of the 3D model used in coupled simulations of EM forming and perforation of tube 40

**Figure 3.17** Cross-section views of the 3D model used in coupled simulations of EM forming of muffler tube 40

**Figure 3.18** Boundary conditions applied 41

**Figure 3.19** Flowchart of the non-coupled simulation 41

**Figure 3.20** 3D model used in ANSYS Maxwell (a) Top view, (b) Front view 43

**Figure 3.21** (a) Full 3D model of setup, (b) Symmetrical cross-sectional view 43

**Figure 3.22** Symmetrical boundary conditions (a) Selected section AOB, (b) Front view 44

**Figure 3.23** 3D model used in Ansys explicit dynamics (a) Isometric, (b) Front and (c) Cross-section view. 44

**Figure 3.24** EDS analysis of as-received Al alloy, (a) Sample for analysis and, (b) EDS analysis result. 45

**Figure 3.25** (a) Oscilloscope for current measurement and (b) RLC measuring equipment 47

**Figure 3.26** Metallographic specimen molding unit (a) Manual and (b) Automatic 47

**Figure 3.27** (a) Manual and (b) Automatic sample polishing machines 47

**Figure 3.28** (a) Optical microscope and (b) Digital microscope 48

**Figure 3.29** (a) Universal Testing Machine and (b) Vickers hardness testing machine 48

**Figure 4.01** Variation of discharge energy for the different discharge current 50

**Figure 4.02** Current waveforms for various discharge energy 50

**Figure 4.03** Tubes after the experiment at different discharge energy for 12-pointed punch arrangement 50

**Figure 4.04** All 12 pierced holes at 6.2 kJ discharge energy for 12-pointed punch arrangement 51

**Figure 4.05** Variation of forming diameter with an increase in discharge energy for 12-pointed punch arrangement 51

**Figure 4.06** Tubes after the experiment for 12 concave punch arrangement at (a) 5.7 kJ and (b) 6.2 kJ 52
**Figure 4.07** Cross section of perforated holes, (a) Pointed punch, (b) Concave punch 52
**Figure 4.08** (a) Variation of number of holes and (b) Diameter of perforated holes with discharge energy for 12 pointed and concave punch arrangements 52
**Figure 4.09** Tubes after the experiment for 36-pointed punch arrangement 53
**Figure 4.10** Tubes after the experiment at different discharge energies for 36 concave punch arrangement 54
**Figure 4.11** (a) Spacer placed in the die, (b) Spacer geometry and (c) Stand of distance with and without a spacer 54
**Figure 4.12** Tubes after the experiment for 36-pointed punch with spacer arrangement 55
**Figure 4.13** Variation of forming diameter with an increase in discharge energy for 36-pointed punch with spacer arrangement 55
**Figure 4.14** Tubes after experiment for 36 concave punch with spacer arrangement 56
**Figure 4.15** (a) Variation of number of holes and (b) Diameter of perforated holes with discharge energy for 36 pointed and concave punch arrangements 56
**Figure 4.16** (a) Hardness value measurement lines and average hardness values at (b) 5.8 kJ discharge energy (c) 6.2 kJ discharge energy (d) 6.6 kJ discharge energy 57
**Figure 4.17** Hardness values obtained for EM perforated hole at 5.8 kJ, 6.2 kJ, and 6.6 kJ discharge energy 58
**Figure 4.18** Optical microscope image of cutting edge of the slug 58
**Figure 4.19** (a)-(e) SEM investigation of the crack zone 59
**Figure 5.01** (a, b) Samples after EM die-less perforation process for, (a) Concave punch, (b) Pointed punch, and (c) Slug obtained after EM concave punch perforation 62
**Figure 5.02** Samples after the Quasi-static perforation for, (a) Concave punch, (b) Pointed punch, and (c) Petals at higher magnification in case of pointed punch 63

**Figure 5.03** Cross section of perforated holes by the pointed punch, (a) EM perforation process and (b) Quasi-static die-less perforation process 63

**Figure 5.04** Cross section of perforated holes by the concave punch, (a) EM perforation process and (b) Quasi-static die-less perforation process 63

**Figure 5.05** Punch exit hole side for quasi-static perforation: (a) Pointed punch and, (b) Concave punch 64

**Figure 5.06** Different zones of sheared edge 64

**Figure 5.07** Sheared edge zones for, (a) EM perforations and (b) Quasi-static die less 65

**Figure 5.08** Effect of the process and punch type on roll-over depth (A), Smooth sheared depth (B), Fracture height (C) and Burr height (D) Values for concave punch (Cp) and pointed punch (Pp) 65

**Figure 5.09** Quantitative measurements of sheared edge: (a) Quasi-static pointed punch, (b) EM pointed punch, (c) Quasi-static concave punch, and (d) EM concave punch 66

**Figure 5.10** Secondary crack formation during Quasi-static die-less perforation with a concave punch 66

**Figure 5.11** Smooth sheared edge during EM die-less perforation with a concave punch 67

**Figure 5.12** Vickers Hardness test of perforated holes: (a) Measurement points, and (b) Hardness values 67

**Figure 5.13** SEM images of the exit side of the hole in quasi-static perforation with a concave punch: (a) Images taken at region A in the crack zone (b) At 2.00 KX magnification, (c) At 3.00 KX magnification and (d) Parabolic fracture profile at 5.00 KX magnification 68

**Figure 5.14** 2.81 KX magnified images of dimple formation in (a) EM perforation, (b) Quasi-static die-less perforation 69

**Figure 6.01** Cross-sections of perforated holes by (a) Pointed and (b) Concave punch 72

**Figure 6.02** Variation of (a) Magnetic field, and (b) Magnetic pressure with time 73

**Figure 6.03** Variation of displacement along the length (measured from symmetry Z face i.e. punch location to the end of the tube) (a) Pointed punch and (b) Concave punch 74

**Figure 6.04** Perforation stages of tubes at different time instances at 5.0 kJ discharge energy for pointed punch in (a) Coupled and (b) Non-coupled simulations with von-Mises stress distribution (in Pa) 74

**Figure 6.05** Perforation stages of tubes at different time instances at 5.7 kJ discharge energy for pointed punch in (a) Coupled and (b) Non-coupled simulations with von-Mises stress distribution (in Pa) 75

**Figure 6.06** Perforation stages of tubes at different time instances at 6.2 kJ discharge energy for pointed punch in (a) Coupled and (b) Non-coupled simulations with von-Mises stress distribution (in Pa) 75

**Figure 6.07** Maximum von-Mises stress at different discharge energies for pointed punch perforation 76

**Figure 6.08** Comparison of perforated holes at (a) 5.0 kJ, (b) 5.7 kJ and (c) 6.2 kJ 76

**Figure 6.09** Perforation stages of tubes at different time instances at 5.0 kJ discharge energy for concave punch in (a) Coupled and (b) Non-coupled simulations with von-Mises stress distribution (in Pa) 78

**Figure 6.10** Perforation stages of tubes at different time instances at 5.7 kJ discharge energy for concave punch in (a) Coupled and (b) Non-coupled simulations with von-Mises stress distribution (in Pa) 78

**Figure 6.11** Perforation stages of tubes at different time instances at 6.2 kJ discharge energy for concave punch in (a) Coupled and (b) Non-coupled simulations with von-Mises stress distribution (in Pa) 79

**Figure 6.12** Maximum von-Mises stress at different discharge energies for concave punch perforation 79

**Figure 6.13** Comparison of perforated holes by concave punch at (a) 5.0 kJ, (b) 5.7 kJ and (c) 6.2 kJ 80

**Figure 6.14** Diameter of the perforated holes in case of concave punch 80

**Figure 6.15** Element selection to obtained variation of different parameters 81

**Figure 6.16** Variation of (a) Radial displacement, (b) von-Mises stress, and (c) Resultant velocity 81

**Figure 6.17** Variation of strain with time 82

**Figure 6.18** Variation of Lorentz force with time at different discharge energies for (a) Pointed and (b) Concave punch perforation 83

**Figure 6.19** Maximum Lorentz force obtained at different discharge energy in coupled 83

**Figure 6.20** Tubes after perforation (a) Experiment and (b) Coupled simulations at 6.2 kJ discharge energy with pointed punch 83
**Figure 7.01** (a) Process setup of EM shearing, (b) Deformation in the workpiece and (c) Shearing of the workpiece 86
**Figure 7.02** Flowchart of simulation process 87
**Figure 7.03** 3D model of setup used in LS-DYNA 88
**Figure 7.04** Deformed workpiece at 300 µs in LS-DYNA at 7.668 kJ discharge energy 88
**Figure 7.05** Variation of current with time at different energy levels 89
**Figure 7.06** EM perforation setup with points denoted for EM pressure readings 89
**Figure 7.07** Variation of pressure with time at three different points on the tube 90
**Figure 7.08** Quadrant meshed 2D model of tube showing the EM pressure applied 91
**Figure 7.09** Showing tool surface contact with internal slug nodes 92
**Figure 7.10** Fringe pattern of JCCRT at (a) 61 µs, (b) 65 µs, (c) 69 µs and (d) 71 µs 93
**Figure 7.11** Variation of pressure with time obtained from perforated tube 93
**Figure 7.12** Plastic strain fringe when (a) 80 die angle, (b) 50 die angle, (c) no die angle 94
**Figure 7.13** Simulation results at different fillet radius (a) 30 µm, (b) 100µm 94
**Figure 7.14** (a) Front view, (b) Side view and (c)Magnified image showing elements where pressure is measured 95
**Figure 7.15** Variation of pressure with time obtained from the simulation of 2 mm tube at four different points (A, B, C, D shown in Figure 7.14) 95
**Figure 7.16** Variation of averaged pressure with time 96
**Figure 7.17** Numerical model of the EM perforation process in Abaqus/Explicit 96
**Figure 7.18** Final deformed shape the 2 mm perforated tube 96
**Figure 8.01** (a) Muffler, (b, c) Failure at the weld zone 99
**Figure 8.02** Grid imprints (a) Before the experiment, (b) After the experiment and (c) Measurement 100
**Figure 8.03** Different coils (a) 80 mm, (b) 100 mm and (c) 120 mm 101
**Figure 8.04** Current waveform obtained at 6.5 kJ discharge energy 101
**Figure 8.05** Magnetic field distribution obtained at the center of the tube using different (a) at 5.0 kJ, (b) at 5.6 kJ and (c) at 6.2 kJ 102

**Figure 8.06** Magnetic pressure distribution at 6.2 kJ discharge energy for (a) Coil 1, (b) Coil 2 and (c) Coil 3 103

**Figure 8.07** Deformation obtained at 6.2 kJ discharge energy for (a) Coil 1, (b) Coil 2 103

**Figure 8.08** Velocity distribution obtained at 6.2 kJ discharge energy for (a) Coil 1, (b) Coil 2 and (c) Coil 3 104

**Figure 8.09** Validation of simulation model for deformation obtained 104

**Figure 8.10** Coil positions (a) Coil covers tube length, (b) 1 turn outside from left end, (c) 1 turn outside from right end (d) 2 turn outside from right end of the tube 105

**Figure 8.11** Lorentz force distribution along the length obtained in simulation (a) Coil covers tube length, (b) 12 mm outside from left end, (c) 12 mm out from right end (d) 24 mm out from right end of the tube 105

**Figure 8.12** Tubes after the experiments and after simulation where coil (a) Covers tube length, (b) 1 turn outside from left end, (c) 1 turn outside from right end (d) 2 turn outside from right end of the tube (Fringe level shows stress in Pa) 106

**Figure 8.13** Validation of simulation results with experimental for coil (a) Covers tube length, (b) 1 turn outside from left end, (c) 1 turn outside from right end (d) 2 turn outside from right end 107

**Figure 8.14** Tubes after the experiments at different discharge energies 107

**Figure 8.15** Variation of deformation with discharge energy 108

**Figure 8.16** Effective plastic strain distribution at various discharge energies 108

**Figure 8.17** Zones of measurement (a) On tube using CMM and (b) During simulation measurement 109

**Figure 8.18** % gap filling with discharge energies in experimental runs 109

**Figure 8.19** % gap filling with discharge energies, validation of simulation results with experimental (b) at 5.0 kJ, (c) at 5.6 kJ and (d) at 6.2 kJ discharge energies 110

**Figure 8.20** The magnetic field distribution in the tube at various discharge energies (Fringe level unit is Tesla) 110

**Figure 8.21** Resultant velocity obtained at various discharge energies (a) Measurement points (b) 5.0 kJ, (c) 5.6 kJ and (d) 6.2 kJ 111

**Figure 8.22** Major and minor strain values 112

**Figure 8.23** The effect of discharge energy on the maximum major and minor strains 113

**Figure 8.24** Variation of hardness with discharge energy 113

# List of Tables

**Table 3.1** Specification of coils 36

**Table 3.2** Details of system and software used 37

**Table 3.3** Material properties [47] 45

**Table 3.4** Properties of ceramic material [47] 46

**Table 3.5** Parameters used in Steinberg-Guinan strength model [47] 46

**Table 3.6** Johnson-Cook strength model parameters [47] Al 6061 47

**Table 3.7** Damage constants used in the Johnson-Cook failure model [47] 47

**Table 4.1** EDS analysis result (composition) 50

**Table 6.1** Diameter of the perforated hole in case of pointed punch 79

**Table 7.1** FEA Input Parameters 90

**Table 7.2** Input EM pressure varying with time 94

**Table 8.1** Elements and nodes 102

**Table 8.2** Simulation conditions applied in LS-DYNA™ 103

# Chapter 1

# Introduction

Since the beginning of the industrial revolution, researchers have been continuously involved in converting the conventional way of manufacturing into an advanced and useful way. To remain competitive with other manufacturing processes, the metal forming processes are being improved by using advanced forming techniques and by developing novel tooling designs to increase the formability of the material and precision. As we know that in metal forming process, external forces are applied on the metal in such a way that the induced stresses are higher than the yield stress and less than the ultimate stress so that the metal is experiencing plastic and permanent deformation. The external force applied during forming is called a deforming force. Typically forming processes are classified into two types, conventional forming process and high strain rate forming processes.

## 1.1 Conventional Forming Process

In the conventional forming process, the raw materials like slabs, billets or blooms are processed through the traditional forming methods like rolling, forging or extrusion to produce materials in standard forms such as plates, sheets, rods, tubes, and structural sections. In these processes, time required for forming will be high, and spring back is also high, this can be overcome by the concept of high energy rate forming processes which are faster and spring back problem can be eliminated.

## 1.2 High Energy Rate Forming Processes

In all of the sub-disciplines of metal forming, high energy rate forming is perhaps more important as it involves the application of high energy for the short duration of time, which enables us to deform large part easily. Many metals tend to deform more rapidly under extra and fast application of a load, which results in the usefulness of these processes to deform large parts out of most metals, including those who are difficult to deform. The parts are deformed at a fast rate, so these processes are called as high-speed or high velocity forming processes. The high strain rates are involved in these processes. Explosive forming, Electrohydraulic forming, and Electromagnetic forming are some of the examples of high strain rate forming processes.

### 1.2.1 Explosive Forming

In explosive forming, as shown in figure 1.1, punch used in conventional forming is replaced by an explosive charge. An explosive can be defined as a substance that produces a high-pressure burst of gas. Explosives used are made up of high explosive chemicals and gaseous mixtures. The working principle of this forming process is very simple, which does not require complicated setup and results in less setup costs. Explosive forming requires specialized process knowledge and a skilled operator for the handling of explosives.

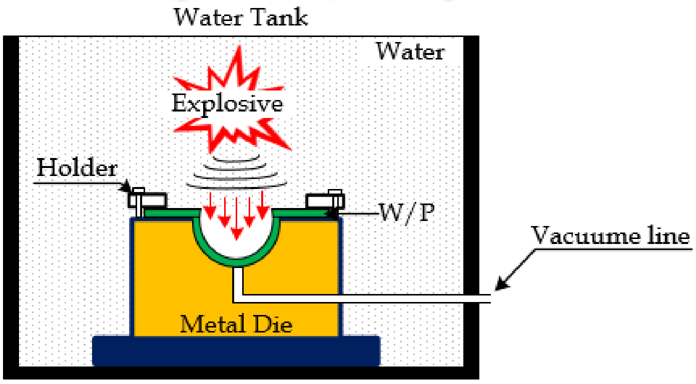

***Figure 1.1*** *Explosive forming*

This forming process is used in the aerospace industries, manufacturing of automotive-related components and forming large size components where the use of conventional forming processes is not possible.

### 1.2.2 Electro-Hydraulic Forming

Electrohydraulic forming (EHF) is considered as the link between electromagnetic forming and chemical explosive forming. EHF is a process in which for the forming of metallic parts, electric energy is converted into mechanical energy.

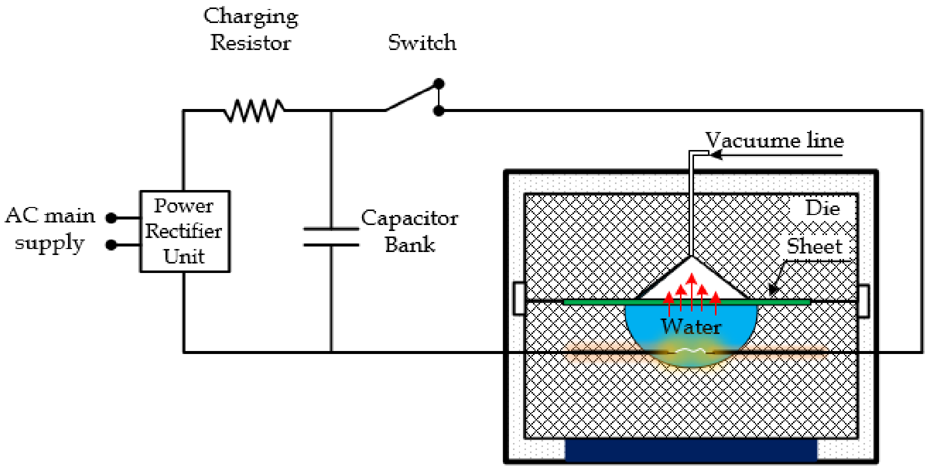

***Figure 1.2*** *Electrohydraulic forming*

Figure 1.2 shows the EHF process setup. A bank of the capacitor is first charged to a high voltage and then discharged across a gap between two electrodes, causes an explosion inside the hollow workpiece. The hollow workpiece is filled with some suitable medium, generally water. The shocks produced by explosion travels rapidly through all directions at high velocity, and they deforms the workpiece. Piercing odd-shaped holes in tubes is a difficult operation for conventional equipment, but it is easier with the EHF process.

### 1.2.3 Electromagnetic Forming (EMF)

The process is also called the magnetic pulse forming process. To study the principle of electromagnetic forming, consider a tubular workpiece. The coil is placed inside the workpiece, as shown in figure 1.3(a). A high charging voltage is supplied for a brief timeframe to a bank of capacitors connected in parallel (The amount of electrical energy stored in the bank can be increased either by adding capacitors to the bank or by increasing the voltage). When the charging is completed, which takes little time, a high voltage switch triggers the stored electrical energy through the coil. A high-intensity magnetic field is established, which induces eddy current into the conductive workpiece, resulting in the establishment of another magnetic field. There would be a robust Lorentz force between the coil and the metal plate. Because of Lenz's Law, the magnetic fields created within the metal workpiece and work coil actively repel each other. The coil creates a strong magnetic force that easily overcomes the yield strength of the metal workpiece, causing permanent deformation. Figure 1.3 (a) shows the electromagnetic forming of the tube, and figure 1.3 (b) shows equivalent circuit diagrams for the process. The process works best with good electrical conductors such as copper or aluminum, but it can be adapted to work with poorer conductors such as steel.

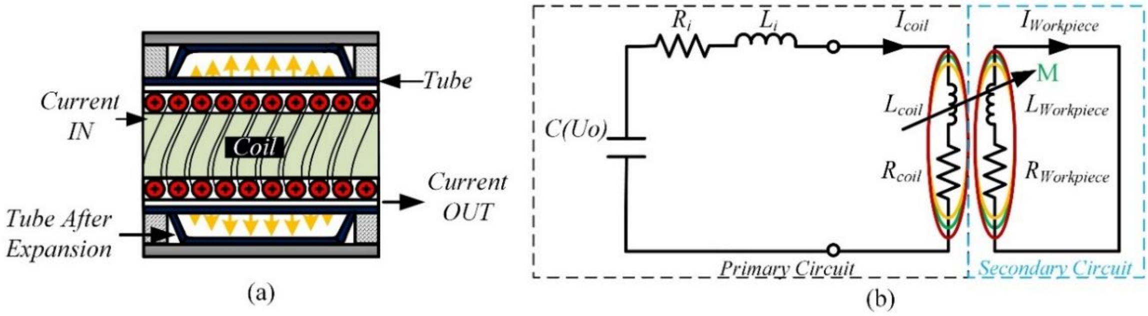

***Figure 1.3*** *(a) Electromagnetic forming of the tube and (b) Equivalent circuit diagrams*

## 1.3 Physics and Principle of Electromagnetic Forming Process

Electromagnetic forming is mainly governed by three physical effects [1], first is a changing magnetic flux in a closed-loop develops a time-dependent current in the loop, as long as the magnetic flux keeps changing, i.e., Faraday's Law. Second, the inductive current has always tended to oppose the change in the magnetic field inducing it and hence produces an opposing current in the coil, i.e., Lenz's law. In the third physical effect, these two opposite direction currents always repel each other, i.e., Lorentz's force. This physics in the process can further be explained by an example given in the above figure of the electromagnetic forming of the tube. A tool coil is placed coaxially inside a metal tube; the coil is connected to a capacitor by a high voltage switch. A high charging voltage is supplied to the capacitor bank for a short time. As charging is completed, a high voltage switch triggers the stored electrical energy through the coil. This current generates a transient alternating magnetic field about the coil; consequently, this field induces an eddy current in the metal tube according to the Faraday's Law. The current in the coil and the workpiece flow in opposite directions obeying Lenz's law and repels each other.

### (i) Faradays Law of Electromagnetic Induction

Faraday's law of Electromagnetic induction states that, whenever magnetic flux passed through coil changes, a current induces in the coil, which is called induced current and the corresponding potential difference is called induced emf. The mathematical expression for induced emf is given by equation 1.1,

$$\varepsilon_b = -\frac{d\phi_B}{dt} \tag{1.1}$$

### (ii) Lenz Law

Lenz law states that the polarity (or the direction of induced current) of the induced emf is in such a way that the magnetic field produced by the induced current opposes the factor producing it. Lenz law is given by the equation 1.2,

$$\varepsilon_{ind} = -\frac{d\phi_B}{dt} \tag{1.2}$$

### (iii) Lorentz Forces

A stationary charged particle only has an electric field in its vicinity. However, whenever it moves, it also creates a magnetic field around its vicinity. So, whenever an electric charge moves through an external magnetic field, there will be an interaction between the external magnetic field and the magnetic field of the charged particle, this interaction (force) is called Lorentz force. The mathematical expression for the Lorentz force is given by the equation 1.3.

$$\vec{F} = \text{Electric Force} + \text{Magnetic Force}$$

$$= q\vec{E} + q\vec{v} \times \vec{B} \tag{1.3}$$

The above expression is a complete equation for the Lorentz force. If there is no external electric field, then the electrical term will get eliminated. Moreover, if we write the same expression in terms of force density and charge density, then the expression is given by the equation 1.4,

$$f = \rho\vec{E} + J \times \vec{B} \tag{1.4}$$

The electromagnetic forming setup can be elaborated with a simple RLC circuit, as shown in figure 1.3 (b). where *R* is the total resistance, *L* is the inductance and *C* is the capacitance of capacitor bank. The high charging voltage (*V*) is supplied to the capacitor bank (*C*). The following equation calculates the stored energy (E) in the capacitor bank,

$$E_c(t) = \frac{1}{2} C V^2 \tag{1.5}$$

The charging of the capacitor bank takes some time; after charging, the energy is discharged through the coil connected to the output. The current flowing through the circuit is damped sinusoidal current and can be described through following equations,

$$L_c \frac{\partial I_c(t)}{\partial t} + M \frac{\partial I_c(t)}{\partial t} + R_c I_c + \frac{1}{C} \int I_c\,(t)\,dt = 0 \tag{1.6}$$

$$\frac{\partial (L_w I_w)}{\partial t} + \frac{\partial (M I_c)}{\partial t} + R_w I_w = 0 \tag{1.7}$$

By solving the above equations with the initial conditions $I(0) = 0$and $L\frac{dI}{dt}(0) = V$gives the following equation of current as a function of time,

$$I(t) = I_m e^{-\beta t} \sin(\omega t) \tag{1.8}$$

$$\text{Where, } \beta = \frac{R}{2L}, \ \omega = 2\pi f = \sqrt{\frac{1}{LC} - \beta^2} \ \text{ and } I_m = \frac{V}{\omega L} \tag{1.9}$$

where $I_m$ is the maximum intensity of the current, $\beta$is the damping coefficient and $\omega$ is the angular frequency. The capacity of a capacitor bank and charging voltage are basic controllable parameters in the EMF system.

The electromagnetic phenomenon involved in the electromagnetic forming process is taken care by the following Maxwell's equations,

$$\nabla \cdot D = \rho_v \tag{1.10}$$

$$\nabla \times \vec{H} = \frac{\partial D}{\partial t} + \vec{J} \tag{1.11}$$

$$\nabla \times \vec{E} = -\frac{\partial}{\partial t}\vec{B} \tag{1.12}$$

$$\nabla \cdot \vec{B} = 0 \tag{1.13}$$

Where $D$ is electric flux density, $\rho_v$ is electric volume charge density, $\vec{H}$ is the magnetic field, $\vec{B}$ is the magnetic flux density, $\vec{E}$ is the electric field, and $J$ is the current density. These all parameters included in equation (1.11) to equation (1.13) are dovetail with magnetization law and ohms law given in equation (1.14) and equation (1.15), respectively.

$$\vec{B} = \mu\vec{H} \tag{1.14}$$

$$\vec{J} = \gamma\vec{E} \tag{1.15}$$

where $\mu$ is the permeability and $\gamma$ is the electric conductivity of the material.

To solve the equation (1.14) and equation (1.15), the magnetic vector potential ($A$) is involved as a system variable, i.e., from equation (1.12) $\nabla \times \vec{A} = \vec{B}$. According to equation (1.12), we can get,

$$\vec{E} = -\frac{\partial A}{\partial t} - \nabla V \tag{1.16}$$

and by substituting this value off $\vec{E}$ to equation (1.15), we can get,

$$\vec{J} = -\gamma\frac{\partial A}{\partial t} - \gamma\nabla V \tag{1.17}$$

where $V$ is the scalar electric potential.

The conservation of current density is zero, i.e. $\nabla \cdot \vec{J} = 0$. The magnetic vector potential can be calculated by solving the following equation (1.18).

$$\nabla \times \left(\frac{1}{\mu}\nabla \times \vec{A}\right) + \gamma\frac{\partial A}{\partial t} = -\gamma\nabla V \tag{1.18}$$

The term $-\gamma\nabla V = \vec{J}_0$ is considered as the external source of current density applied to the medium, and it is zero for the workpiece and the air. After calculating the value of magnetic vector potential ($\vec{A}$) the magnetic flux density ($\vec{B}$) and current density ($\vec{J}$) in the workpiece can be determined and subsequently the Lorentz forces ($\vec{F}$) can be calculated by the equation (1.19),

$$\vec{F} = \vec{J} \times \vec{B} \tag{1.19}$$

For capturing the material behaviour, the relation between stress and deformation for a solid body will give the equation of motion,

$$\rho \frac{\partial^2 u}{\partial t^2} = \nabla \bullet \sigma + F \tag{1.20}$$

Where $\rho$ is the density, $u$ is the displacement, $\nabla \bullet \sigma$ represents materials constitutive law (stress-strain relation), and $\vec{F}$ is the Lorentz force where the magnetic force is considered. Lippmann and Schreiner (1964) [2] developed the relationship between magnetic pressure and the inertia force of the tube. It depends on the density ($\rho$) and thickness of the workpiece.

The acceleration of workpiece is given by equation (1.21),

$$\frac{d^2 u}{dt^2} = \frac{1}{2\mu_0 \rho s} {B_z}^2 \tag{1.21}$$

Where $B_z$ represents the axial component of magnetic flux density and $\mu_0$ is the permeability of free space.

$$v = \frac{du}{dt} = \frac{{B_m}^2}{2\mu_0 \rho s} t \tag{1.22}$$

The integration of the above equation gives the velocity and presented by equation (1.22). After integrating the above equation, deformation ($u$) is obtained.

$$u = \frac{{B_m}^2}{2\mu_0 \rho s} t^2 \tag{1.23}$$

## 1.4 Advantages and Limitations of Electromagnetic Forming Process

The EMF has many advantages over conventional forming techniques, which makes this process an alternative technology for traditional manufacturing processes. The main benefits of EMF are listed as follows,

- It is a high-speed forming process. The materials which have very low formability can also be formed by using this technique

- The system requires low maintenance and short process time which significantly increases the productivity
- It is easy to automate EMF operation in combination with the mechanization of setup
- The input parameters of EM forming are current, voltage, and discharge energy. So, this process has a very high repeatability
- Electromagnetically formed products show less spring-back compared to conventional formed products, thus creating products with a better accuracy
- Improved surface hardness due to EM peening effect
- The process is environmentally friendly

It has some drawbacks also like,

- Significant requirements regarding safety aspects are necessary because of the involvement of high current and high voltages.
- EM forming is suitable only for the electrically conductive material because the extent of induced eddy current depends upon the property of the material. However, this can be overcome by using driver plates or field shaper of conductive materials
- Only a small part of the charging energy is used for the plastic deformation resulting in comparable bad efficiency.
- The initial cost of the process is high as EM forming machine is costly as compared to a conventional setup

# Chapter 2

# Literature Review

## 2.1 Introduction

Electromagnetic forming is an impulse or high-speed forming technology using the pulsed magnetic field to apply Lorentz's forces to the workpiece, preferably made of a highly electrically conductive material without mechanical contact and a working medium. Psyk. et al. [3] studied the electromagnetic forming. They identified that different applications of electromagnetic forming like a compression of the tube, expansion of tubes, and sheet metal forming could be achieved by different geometries and arrangements of the coils, as shown in figure 2.1.

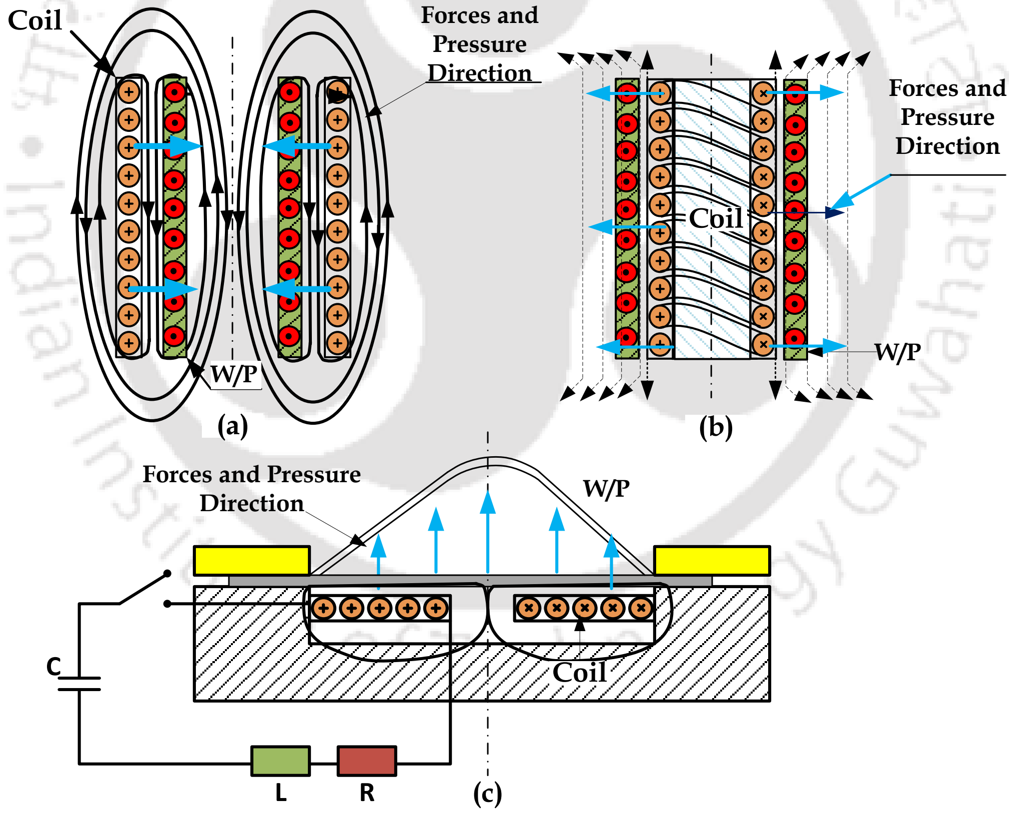

***Figure 2.1*** *Different coils for different application in EM forming process*

The numerical and experimental work on high-speed free forming of the clamped circular disk in an electromagnetic forming system using a flat spiral coil was presented by Takstsu et al. [4]. The penetration of the magnetic field of coil into the disk was formulated as a boundary value problem for the diffusion equation.

The magnetic field possesses the radial component $B_r$, axial component $B_z$, circumferential eddy current $J_f$, force density both radial $F_r$and axial $F_z$are calculated by the following equations,

$$-\frac{1}{\mu_0\sigma_w}\left(\frac{\partial^2}{\partial r^2}+\frac{1}{r}\frac{\partial}{\partial r}+\frac{\partial^2}{\partial z^2}-\frac{1}{r^2}\right)B_r+\frac{\partial B_r}{\partial t}=-\frac{\partial}{\partial z}(v_zB_r-v_rB_z) \tag{2.1}$$

$$-\frac{1}{\mu_0\sigma_w}\left(\frac{\partial^2}{\partial r^2}+\frac{1}{r}\frac{\partial}{\partial r}+\frac{\partial^2}{\partial z^2}\right)B_z+\frac{\partial B_z}{\partial t}=\frac{\partial}{\partial z}\{r(v_zB_r-v_rB_z)\} \tag{2.2}$$

$$J_{f^\theta}=\frac{1}{\mu_0}\left(\frac{\partial B_r}{\partial z}-\frac{\partial B_z}{\partial r}\right) \tag{2.3}$$

$$F_r=J_{f^\theta}\cdot B_z \tag{2.4}$$

$$F_z=-J_{f^\theta}\cdot B_r \tag{2.5}$$

where $J_f$ is the current density, $\sigma_w$ is the conductivity, $\mu$ is the permeability, $v$ is the velocity of the medium, $t$ is the time, and $r$ is the radius of the disk.

The authors concluded that the numerical method developed in this work could be used for the prediction of electromagnetic forming of sheets [4]. Gayakwad et al. [5] presented the state of the art of electromagnetic forming subjected to parameters related to workpiece deformation, the interaction between load parameters and behaviour of materials, energy interaction during the process, and research regarding the principle and application of electromagnetic forming. By study, they proposed the challenges for the widespread application of the electromagnetic forming process. During electromagnetic forming initially, the energy stored in the pulsed power generator as capacitive energy. This capacitive energy is used to deform the workpiece at the end of energy transfer, as shown in figure 2.2.

Bay et al. [6] studied the electromagnetic forming process, material behavior, and computational modeling. A procedure has been developed to deal with the identification of material behaviour. Electromagnetic forming experiments were performed for free forming and cavity fill operations by Oliveira et al. [7]. The experiments were performed on a 1 mm and 1.6 mm aluminium alloy sheet. Numerical solutions of high rate deformation and structural impact were presented in this study. Two-Way loose coupling with elastic-plastic structural analysis was utilised and concluded that the loosely coupled numerical models provide reasonable predictions of deformation and strain distribution.

Still, it is required to have other damage based constitutive models before they can be used for formability prediction.

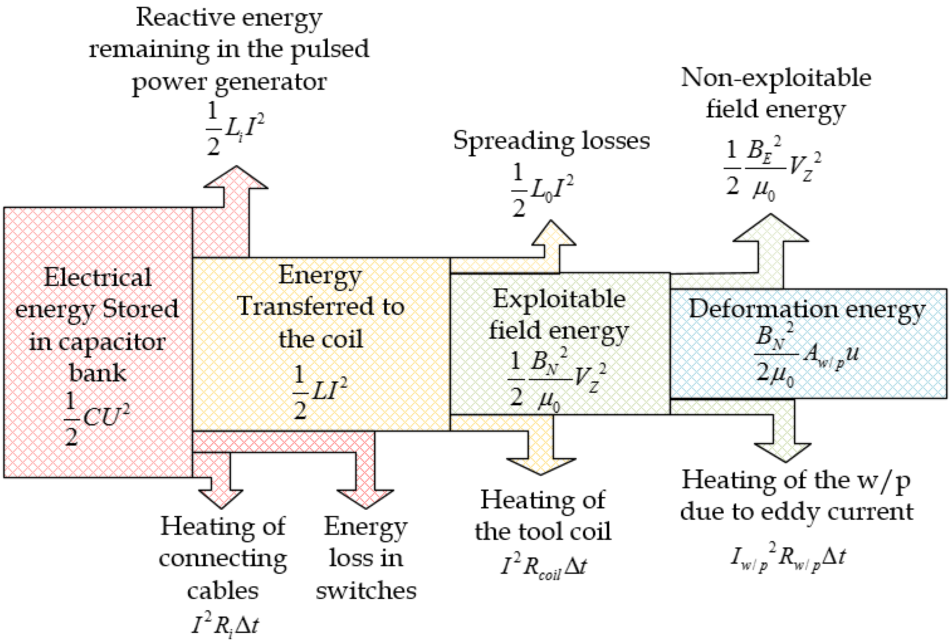

***Figure 2.2*** *Energy transfer during electromagnetic forming*

Alle Navee Kumar and Mashuq-Un-Nabi [8] had presented a study on FEM and simulation of electromagnetic forces in electromagnetic forming of a thin metal sheet using a coil configuration with uniform spacing between the turns using COMSOL Multiphysics. They observed that magnitude of forces is high enough for shearing of the material.

## 2.2 Electromagnetic Tube Forming

The arrangement of the tool coil and the workpiece defines the process type. In the experiment of electromagnetic forming, as shown in figure 2.3, for tube expansion, coil is placed inside the tube while for compression, the tube is placed inside the tool coil.

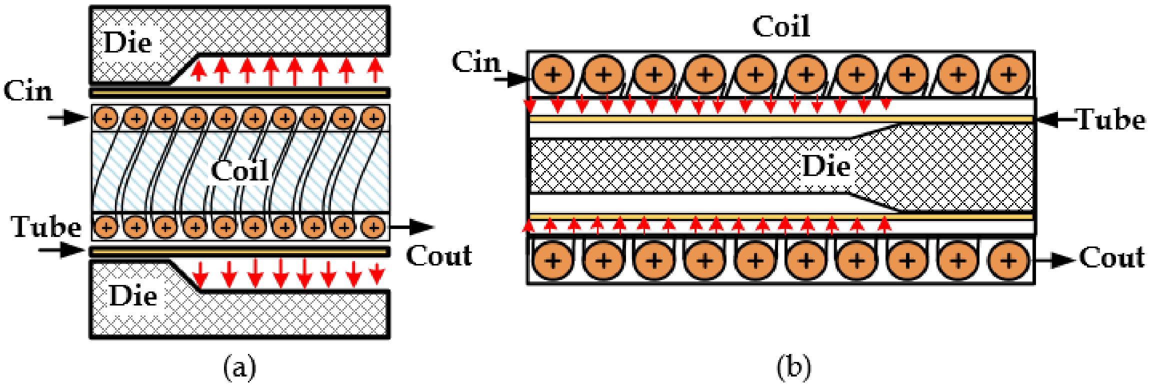

***Figure 2.3*** *(a) EM expansion and (b) EM compression of the tube*

### 2.2.1 Electromagnetic Tube Expansion

For the electromagnetic tube expansion, the coil is placed inside the metal workpiece. A huge pulse of current is forced through the work coil by rapidly discharging a high voltage capacitor bank using an ignition or a spark gap as a switch; this creates an electromagnetic field around the work coil. The high work coil current creates magnetic forces that easily overcome the yield strength of the metal workpiece, causing permanent deformation. The metal forming process occurs extremely quickly, and because of the large forces, portions of the workpiece undergo high acceleration. Analytical and experimental investigation of tube forming was carried out by Zang et al. [9]. They concluded that longer lengths of the coil and smaller capacity of capacitors are more efficient, and the efficiency of forming is maximum when skin depth is 0.9 mm. Pravin Ghatule and Sachin D. Kore [10] studied the electromagnetic expansion of the tube for analyzing the electromagnetic field and deformation pattern. With the help of simulation, they studied EM expansion of Al tubes using LS DYNA™ Multiphysics software. They concluded that the maximum electromagnetic field was present at the middle of the coil, and hence the maximum deformation was obtained at the middle of the workpiece.

The study of the electromagnetic expansion of thin metal rings was presented by Gourdin et al. [11]. Electrodynamic calculations for copper, tin, and lead rings were calculated and compared with experimental results. They found that for copper, which is a good conductor, the maximum useful strain rate will be limited by Joule heating of specimen. Materials which have large resistivity and strength, direct expansion of rings is difficult. By using the composite ring as the driver made up of highly conductive material, the low conductive material can be expanded.

Song et al. [12] investigated the effect of the relative position of workpiece and coil on the distribution of transient magnetic pressure experimentally in the case of the aluminium tube using a 14-kJ electromagnetic forming machine. The effect of varying axial position of the deformation patterns obtained in tubes with respect to uniform and non-uniform forces was observed in this paper. Their experimental result showed that a variety of deformed shapes of the tube could be obtained by adjusting the relative position of the coil and workpiece. They concluded that the two main factors contributing to the magnetic intensity between workpiece and coil are coil parameters and relative position of coil and workpiece. Shang et al. [13] presented a comparative study between experimental and numerical results of electromagnetic tube expansion. The experiments were carried out on the Al 6061-T6 tubes, and a numerical study was done with the LS-DYNA EM module. Photon Doppler Velocimetry (PDV) was used to measure the velocity during tube expansion. They concluded that the combination of PDV and EM module simulation could be applied for verification of parameters of constitutive models in high strain rate and to study the dynamic behaviour at high strain rates.

In an electromagnetic expansion of a low conductive metal tube, the requirement of voltage or capacitance of a capacitor bank is significant. With the increase in the voltage, electromagnetic pressure also increases, but also it leads to an increase in temperature. The study of Shin et al. [14] concluded that the increase in temperature could be avoided by using a high conductive driver layer to deform a low conductive metal tube effectively. According to Siddiqui et al. [15], the working range for tube expansion for capacity was observed to be between 200µF and 800 µF for 1 KJ charging energy. They developed an in-house code in FORTRAN for electromagnetic tube expansion. The results obtained by in-house code were compared with those obtained from finite element software FEMM. These verified results are in agreement with available experimental results, and they concluded that this developed method could predict the electromagnetic tube expansion process. Magnetic pressure analysis is the foundation of theoretical analysis in Electromagnetic forming as it is a high energy rate forming process. Chunfeng et al. [16] carried out a numerical simulation of the magnetic pressure acting on the workpiece during EM forming of the tube by the use of FEA software ANSYS. They concluded that during bulging, for the penetration of the magnetic field, the whole workpiece is subjected to the radially outward expansive force.

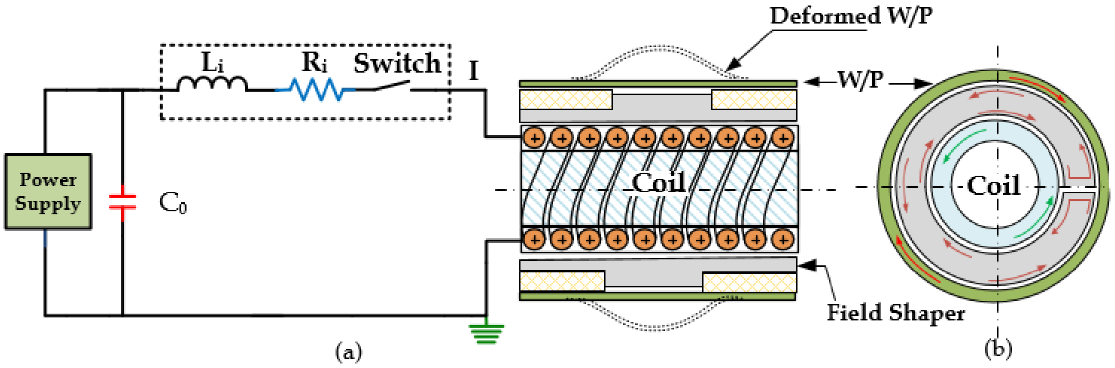

***Figure 2.4*** *(a) Use of field shaper for tube expansion and (b) Current directions*

Suzuki et al. [17] performed experiments to investigate the effect of different geometries of field shaper in electromagnetic tube bulging. The experimental setup for tube bulging using a forming coil with a field shaper is shown in figure 2.4. They concluded that with the help of a combination of field shaper geometry and charged energy in the capacitor bank, an approximate prediction of the final shape of bulged could be possible. The patent, electromagnetic shape calibration of tubes developed by Bradley et al. [18] helps in reshaping the tube ends, which is the part of the manufactured product rather than scrapping out that part.

### 2.2.2 Electromagnetic Tube Compression

A.G. Mamalis et al. [19] studied free compression of an Aluminum tube inside a solenoid coil. The most significant mechanical as well as electromagnetic time-varying or spatially distributed parameters of the process were figured efficiently in the same modeling environment. They concluded that only the first half of the pulse is responsible for deformation, rest of the pulse does not have sufficient energy to deform the workpiece. Bartels et al. [20] did the finite element analysis of EM forming on the tubular workpiece, with two different discharge velocities. The deviations between the two methodologies increase with time and may yield significant overestimations of the loosely coupled model. Therefore, they concluded that the simple loose coupled approach could be used for relatively fast deformation processes. Otherwise, the more accurate sequential coupled model should be used.

Vivek et al. [21] observed significant deformation in electromagnetic compression of the tube; they found about 8% reduction in diameter for 16kJ and 15% reduction in diameter 24 kJ discharge energies. They measured velocity, primary and secondary current during EM compression of steel tubes. Simulation of wrinkle formation during electromagnetic tube compression was carried out by Demir et al. [22]. Compression results in wrinkles; it is also known as the imperfection trigger buckling. They introduced the imperfection of the tube contour into the FE model. With this approach, it is possible to simulate the wrinkle, which results in good agreement with experimental results. A fully coupled numerical procedure and the equivalent electric circuit of the EMF charging machine, electromagnetic field propagation, heat transfer, and dynamic elastoplastic deformation has been developed based on finite element package ANSYS by Karch, et al. [23]. Gharghabi et al. [24] studied the electromagnetic tube forming process by using simulations based on finite element methods. They also investigated the impact of workpiece thickness and field shaper geometry on the performance of the process. They concluded that the thickness of the workpiece should be at least equal to the skin depth of the workpiece, and for better results high frequency of the discharged current is required.

Chaharmiri et al. [25] investigated the effects of geometrical specifications of stepped field shaper on radial displacement and magnetic pressure. Experiments were carried out at various discharge voltages using two different coils (C53 of internal diameter 53 mm, C100 of internal diameter 100mm), and results were compared with simulations. They concluded that with the help of C100 coil with a stepped field shaper, the magnetic pressure concentration ratio increased from 23 to 85 % in comparison with C53 direct coil, and radial displacement increased by 8% in simulation and 6% in the experiment.

Arezoodar et al. [26] studied the effects of various field shapers with different geometries on the distribution of the magnetic flux densities. They applied force on the workpiece in the Electromagnetic inward tube compression forming with the help of FEA software. The FEA model is verified with experimental results. Experiments were carried out on multiple stepped field shaper, having different shapes like conical, cylindrical, concave, and convex shapes. Figure 2.5 shows the different shapes of field shapers.

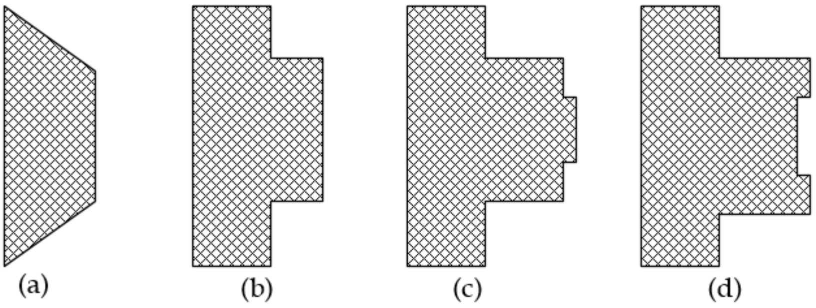

***Figure 2.5*** *(a) Conical, (b) Cylindrical, (c) Convex, (d) Concave*

They concluded that field shaper height near the coil has a positive effect on the magnetic field; it increases with an increase in height. They recommended that keep the depth of step nearest to the coil small and to have a maximum magnetic field in a three-step field shaper keeping the height of the third step small. Experimental and numerical study of the inside bead forming of an aluminium tube by using a compressive coil was carried out by Murakoshi et al. [27]. The influence of the discharge voltage and the bead geometry was investigated and compared with the simulation results. They found that the bead geometry and longitudinal strain of the aluminium tube are affected by the discharge voltage and dimensions of the groove at the beading die. Electromagnetic tube compression simulation was performed by Haiping et al. [28] using finite element software ANSYS by considering sequential coupling. In this method, simulation accuracy is improved by considering the effect of tube deformation on the electromagnetic geometry in the electromagnetic model.

Yu and Li [29] investigated the effects of coil length on tube compression, both numerically and experimentally. The effect of coil length on the waveform of coil current and deformation of the workpiece, the value of equivalent magnetic pressure, energy efficiency were studied. Three coils C1, C2, and C3 of reducing orders of lengths respectively were used for experiments. The equivalent inductance (L) of the discharge circuit can be expressed by the equation 2.6.

$$L = L_{\mathrm{i}} + L_{\mathrm{c}}\left(1 - {a^2}/{c^2}\right) \tag{2.6}$$

Where $a$ is the tube middle radius (m), $c$ is the inner coil radius (m), $L_{\mathrm{i}}$ is the inherent inductance of circuit (H), the coil inductance $L_{\mathrm{c}}$ is given by,

$$L_c = \lambda \mu_0 \pi c^2 T^2 l \tag{2.7}$$

Where $\mu_0$ is the vacuum permeability (H/m), $\lambda$ is the Nagaoka coefficient, $T$ is the number turns of the coil, $l$ is the coil length (m).

From the equation 2.7, $L$ mainly depends on coil inductance; therefore, an increase in the length of the coil causes an increase in equivalent inductance of the circuit. The primary current waveform is dependent on the coil length, with an increase in coil length, the current pulse reduces, and the period of it increases. They concluded that the distribution of magnetic force acting on the tube is inhomogeneous when the tube is longer than the coil, and the shortened coil length causes an increase of the maximum deformation and energy efficiency.

Bartels et al. [30] compared two different simulation algorithms for the electromagnetic compression of the tube. A comparison between the custom loose coupled simulation model and the sequential coupled simulation model is studied in this work. The flow chart of both models is shown in figure 2.9. They concluded that the deviation between the two-simulation model increases with time. The loosely coupled approach leads to an overestimation of the final deformation, while the sequential coupled model shows better results.

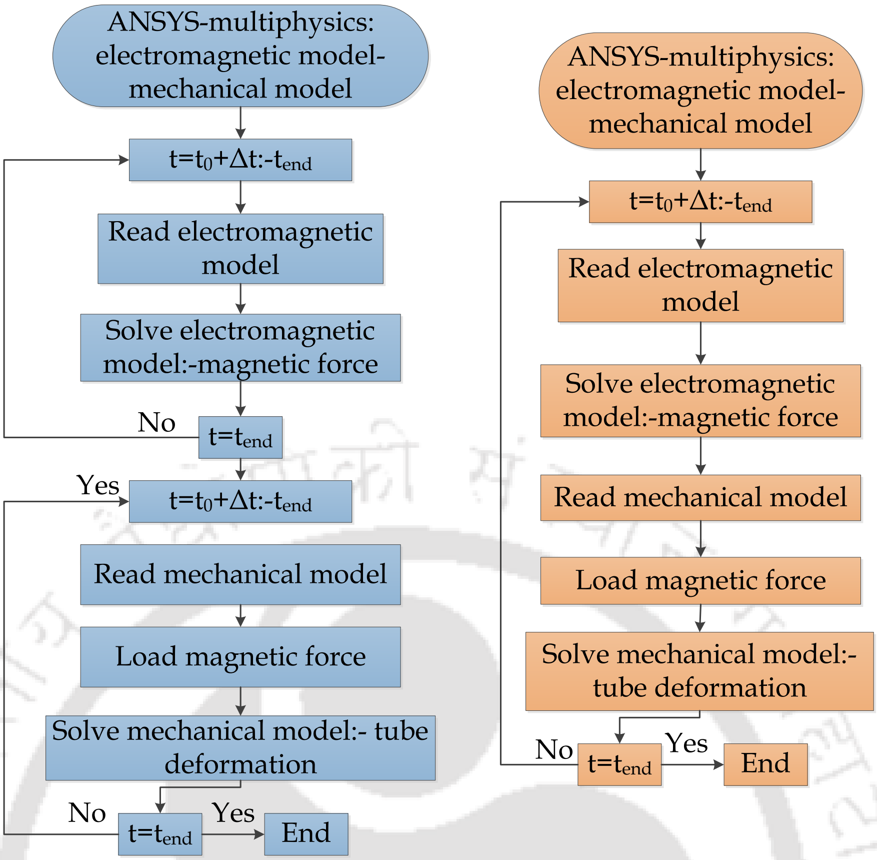

(a) (b)

***Figure 2.6** Loose coupled and sequential coupled model*

With the help of sequential coupling numerical simulation and keeping discharge energy constant, the effects of the current frequency on electromagnetic tube compression were analyzed by Haiping et al. [28].

The following equation can be derived by substitution of the constitutive equations of the electromagnetic field into Maxwell's equations

$$\nabla \times \left( \frac{1}{\mu} \Delta \times \vec{A} \right) = -\gamma \frac{\partial \vec{A}}{\partial t} \tag{2.8}$$

where $\mu$ is the magnetic permeability, $\gamma$ is the conductance of the medium (S/m), $-\gamma \frac{\partial \vec{A}}{\partial t}$ Is the induced current density in the tube (A/m$^2$).

According to Maxwell's equation, the magnetic force $\vec{f}$ in a unit volume of medium is given by the following equation,

$$\vec{f} = \vec{J} \times \vec{B} = \frac{1}{\mu} \left( \Delta \times \vec{B} \right) \times \vec{B} \tag{2.9}$$

Hence the magnetic forces acting on the tube and expressed with magnetic vector potential $\vec{A}$ can be obtained by substituting $\nabla \times \vec{A} = \vec{B}$ into the equation and used as the input load in the mechanical model. They concluded that the current period increases, and its amplitude reduces with decreasing the frequency. The result of this causes an increase in the total time of the forming process. A method for reducing the wrinkles produces after the electromagnetic compression of the tube by using mandrels was analyzed and introduced with the help of an impact contact algorithm by the Min et al. [31]. For the theoretical calculation of a number of wrinkles, some assumptions were made by the author. It is observed that the number of wrinkles has a linear relationship with ratio of radii to thickness of the tubes. From the study, they concluded that the basic assumptions and analysis methods used in the study are beneficial for the electromagnetic tube compression process.

### 2.3 Perforation of Tube

Perforation is a common practice for producing an array of holes in the metal across many industries. Perforated tubes not only used in automobiles but in the machinery where the exhaust system is present. Some applications of perforated tubes are,

- ✓ Acoustical dampening
- ✓ EMI shielding
- ✓ Oil rig filtration
- ✓ Structural support
- ✓ Safety guards
- ✓ Liquid, gas, or vapour diffusor
- ✓ Grills or trim
- ✓ Liquid filtering
- ✓ Light diffusion
- ✓ Decorative items
- ✓ Structural members
- ✓ Agricultural strainers

### 2.3.1 Conventional Manufacturing of Perforated Tubes

In the conventional manufacturing of perforated tubes, the metal sheet is perforated by traditional practices, then rolled and welded into the tube. There are some manufacturers of perforated tubes, like Accurate Perforated Pipe Co. Ltd., Spiral Manufacturing Co., Mille Miglia Engineering, Bauer Welding & Metal Fabricators. Perforated tubes incorporated companies lead to manufacturing straight seam welded perforated pipe by a perforated metal sheet which is cut to the desired size, then rolled and welded into a tube. A spiral-welded perforated tube which is helically formed and automatically welded from the continuous perforated sheet.

#### 2.3.1.1 Aluminium Perforated Tubes

Perforated tube made up of aluminium material is mostly used in screens, filters, shields, guards of engineering, construction, and material handling industries. It is also used for low-temperature applications when its strength increases and ductility retains. However, for very high-temperature usage aluminium tube tends to lose some strength. One of the unique advantage of the use of perforated aluminium pipe is its ideal corrosion resistance and strength-to-weight ratio. Nowadays, for some applications, weight should be kept at a low level to ensure smooth operation. Under this condition, the use of a perforated aluminium tube is the best option. It provides enough strength as well as less weight compare to other metals like stainless steel or mild steel.

An exhaust baffle is a simple device that is placed inside a motorcycle's exhaust pipes. A baffle is a motorcycle exhaust pipe, a sort of muffler designed to reduce engine noise. The baffle is a perforated metal tube that restricts the airflow coming from the exhaust. The reduced airflow from the baffle creates a differential in air pressure that forces some of the exhaust back into the engine. This not only reduces sound but also helps the engine perform better. Unburned fuel gets pushed back into the engine along with the exhaust and is utilized, improving both fuel consumption and horsepower. The material used for baffles depends on the application. Aluminum is a lightweight material that works well for rimfire silencers. Rimfire silencer is a part of the barrel of an air gun. Aluminium baffles are not strong enough to handle high pressure. Stainless steel is probably the most popular material used for automobile exhaust baffle and also for high-pressure applications. Baffles are manufactured by the conventional perforation process, as explained earlier.

## 2.4 Experimental and FEM Study on High Strain Rate Perforation

### 2.4.1 FEM and Experimental Study on Perforation of Tubes

Experiments were carried out on the perforation of cylindrical tubes by quasi-statically and dynamically moving projectiles. For the dynamic tests, the kinetic energies of the projectiles were far more than that required to penetrate the tube. In all the cases, the tubes were penetrated. The comparison shows that there is no hinge formation in case of the dynamic test. In contrast, statically tested tubes show structural deformation, which is characteristic of that produced by traveling plastic hinges [32]. Water filled aluminium tubes subjected to impact by different size projectiles at impact velocities of 40-200m/s were studied by Nishida et al. [33]. The effect of diameter of projectiles and material properties of the tubes on cracking and perforation were discussed. Perforation limit velocities for both water-filled and empty tubes decreased with increasing diameter of the projectiles; however, crack limit velocities are not directly correlated with the diameter of projectiles. Results show water decreases the strength of the tube wall, and the impact velocity at which a steel projectile passes through the tube wall decreases with the increasing diameter of the projectiles. Using the velocities at which a steel projectile perforates the tube wall, the empirical equation of the energy required to perforate the tube wall was derived. The derived equation for the perforation limit energy and the crack limit energy can be described by the equation 2.10

$$E_p = 4.8 \times 10^{-2}(\sigma_u \partial)^{1.5} d^{1.95} t^{1.43} D^{-0.19} \tag{2.10}$$

Following relationships concerning the perforation limit energy were derived for the 8 mm steel projectile, for water-filled tubes,

$$E_p = 1.4 \times 10^{3}(\sigma_u \partial)^{0.8} d^{1.98} t^{1.22} D^{-0.12} \tag{2.11}$$

For the empty tube,

$$E_p = 4.8 \times 10^{-2}(\sigma_u \partial)^{1.5} d^{1.95} t^{1.43} D^{-0.19} \tag{2.12}$$

$$\left(0.14 < \frac{d}{D} < 0.25, 50 < \frac{D}{t} < 100\right)$$

Where $E_p$ is the energy required for perforation of tubes, $t$ is the thickness of the tube, d is the projectile diameter, $D$ is the diameter of the tube, $\sigma_u$ is the ultimate strength of the material, $\partial$ is the total elongation, and the values of indices and constants were obtained from previous experiments.

### 2.4.2 FEM and Experimental Study on Perforation of Sheets

The focus of work done by Schwer et al. [34] was to assess a new class of numerical methods to offer alternative analytical techniques for the ballistic problem. They compare projectile residual speeds provided by various techniques used to simulate a ballistic impact experiment. These techniques are the meshfree methods known as Smooth Particle Hydrodynamics, a multi-material Arbitrary Lagrange Eulerian (MM-ALE) technique, and Lagrangian with material erosion. For the present study, a 12.7 mm aluminium plate target was impacted by the blunt projectile made from Al 6061-T6. Projectiles observed exit speed was 345 m/s. Projectile deformation increases as it perforates thicker plates. The Johnson-cook failure criteria is necessary for Lagrange models and Smooth Particle Hydrodynamics models. The Johnson-cook material is used to represent the constitutional behaviour of the Al 6061-T6 of both projectile and target. In MM-ALE simulation, the projectile has not fully perforated the target plate because it has minimal residual speed. The addition of the spall criterion increases the projectile residual speed. Residual speeds obtained by SPH are quite close to experimental value, but as particles mesh refines the projectile speed increases, it diverges from experimental observations.

Experiments were carried out with the help of a gas gun using projectiles with three different nose shapes (blunt, hemispherical, and conical) to penetrate a 12 mm thick steel plate at 300 m/s ballistic limit velocity by Borvik et al. [35]. It was found that the shape of the nose plays a significant role, and it affects both the energy absorption mechanism as well as the failure mode of the target during penetration. Mainly blunt projectile caused failure by plugging, which is dominated by shear banding, while hemispherical and conical projectiles penetrate the plate by pushing the material. The cross-section of target plates perforated by projectiles and macroscopic view of the perforation zone shows a localized shear band during blunt projectile perforation.

A constitutive model of viscoelasticity and ductile damage for the projectile has been developed and implemented using LS-DYNA. Numerical simulations are carried out, and the results are compared with the experimental data. Minimal deformation takes place outside the localized shear zone for the blunt projectile. The difference between the final cross-section of the hemispherical and conical projectile is small in case of simulation, while this difference is more in an experimental study. The values of maximum target deformations during experimental work and obtained from the simulation in close agreement. The maximum deformation is found to be higher numerically than experimentally at identical impact velocity. The target deformation is found to decrease from a maximum value at the ballistic limit to minimal value at high impact velocity [36].

The study of experimental and numerical analysis of the failure process of mild steel sheet subjected to the normal impact by hemispherical projectile presented by Rusinek et al. [37]. For force measurement, the Hopkinson tube was used. The petalling phenomenon is observed when the projectile is lubricated while for dry condition radial neck along with a hole enlargement was seen which reduces the formation of petalling. The formation of multiple necks and cracks around perforations in the ductile material was investigated by Atkins et al. [38]. They developed the expressions for the number of plane strain radial necks formed by conical penetrators and by round ended projectiles into flat targets. They derived the expressions for the number of radial cracks, which form subsequently in both the cases, which lead to petalling.

Number of radial cracks propagated from $r_0$ to $r_c$ by conical projectile $N_{\text{cone}}$ given by equation 2.13,

$$N_{\text{cone}} = \frac{2\pi Y r_0 \varepsilon_f}{R} \tag{2.13}$$

where $Y$ is yield strength, $r_0$ is the starter hole radius in the target, $r_c$ is the radius at the crack front and $\varepsilon_f$ is the effective fracture strain.

Number of cracks propagated from $r_0$ to $r_c$by ball projectile $N_{\text{ball}}$ given by equation 2.14,

$$N_{\text{ball}} = \frac{2\pi Y r_0 \varepsilon_f}{R} \tag{2.14}$$

The expression of both conical and ball projectile is same. For conical projectile, the result is independent of cone angle; for the ball projectile, the result is independent of ball diameter. No. of necks forms during the conical projectile can be predicted by following equation 2.15,

$$N_{\text{neck\_cone}} = 2\pi\left(\exp n - \sin\alpha\right)/(dt/dr) \tag{2.15}$$

Number of necks forms during the ball projectile can be predicted by given equation 2.16,

$$N_{\text{neck\_ball}} = 2\pi\left(\exp n - \cos\omega_n\right)/(dt/dr) \tag{2.16}$$

where t is the thickness of the sheet, $n$ is the work hardening index, $\alpha$ is the semi-angle of cone penetrator, and $\omega_n$ is the coordinate of the location of first necking. They concluded that the number of cracks is smaller than the number of necks, and numerical analysis is in agreement with experimental analysis.

Different thickness metal plates of Al 6061-T6 impacted by two different armor-piercing projectiles were studied from the metallographic view by Manes et al. [39]. The material behaviour after impact was investigated by optical and scanning electron microscope (SEM) as well as by microhardness tests. The SEM investigation provides information about the morphology obtained after the high-velocity impact. The kinetic energy of the projectile is dissipated during the impact in two different ways; one part causes the plastic deformation. Also, it results in an increase in temperature due to plastic work converts into heat. The second part is directly dissipated in friction effect as heat; this effect seems more pronounced in the tungsten carbide core bullet. Both effects result in instant melting of alloy, which is then re-solidified on the internal part of hole. The 25 mm plates impacted by steel core bullet have been analyzed, the entry hole features have an evident ductile hole enlargement with a clear petalling phenomenon. The absence of petalling phenomenon and noticeable microstructure alteration indicates that the tungsten bullet transfers more thermal energy to the Al 6061 T6 plates. Hardness study concluded that steel core projectiles produce a stable trend of hardness along the three lines while the tungsten core projectile modifies the hardness value.

### 2.4.3 Advantages of High Strain Rate Perforation

High strain rate perforation or shearing has many advantages over conventional shearing. Some of them are listed below,

- Some of the materials are not easy to perforate; perforation in this type of material with a conventional process is difficult. In case of high strain rate perforation, the kinetic energy of the projectiles or flayer is far more than that required to penetrate the workpiece because of this perforation in difficult to perforate materials is easily possible.
- High strain rate shearing processes can overcome the disadvantage of conventional perforation by eliminating the burrs and slivers in the sheared part. High strain rate perforated workpieces are dominated by localized penetration, so structural deformation of the workpiece is less as compared to low strain rate processes.

## 2.5 Failure Modes and Material Model

### 2.5.1 Failure Modes

The metals are isotropic materials. They have same properties in all directions. When an impact occurs, the kinetic energy of the projectile is impacted on the plate or tube. Imparted energy is divided into parts. Some of the energy is used to deform the plate; some part of the energy is converted into heat and light. The last part, i.e., the remainder is imparted to the fragments as kinetic energy. The impacted target materials may fail by a combination of different modes like spalling, plugging, petalling, ductile or brittle fracture or by adiabatic shearing [40]. Figure 2.26 consists of the mode of fractures resulting from the initial stress wave, fracture in the radial direction, spalling, scabbing, plugging, petalling, fragmentation, and ductile hole enlargement.

Fracture due to initial stress value is because of excessive stress wave having value more than ultimate compressive strength, and it could probably occur in weak, low-density targets. Radial fracture is limited to the elements whose tensile strengths are lower than corresponding compressive values. Plugging develops nearly cylindrical slug having same shape and size as those of the projectile. In this case, fracture occurs due to large heat produced by the moving slug. The heat generated by the shear deformation is restricted to a narrow annulus, which decreases the material strength resulting in instability; this is called an adiabatic shearing process. Mostly plugging is found in the case of the blunt projectile, which penetrates thin, hard plates. Petalling is produced by high radial and circumferential tensile stresses. In this, the deformation is resulting in a bending moment created by forward motion of plate material being pushed ahead of the striker and by inhomogeneities of a target.

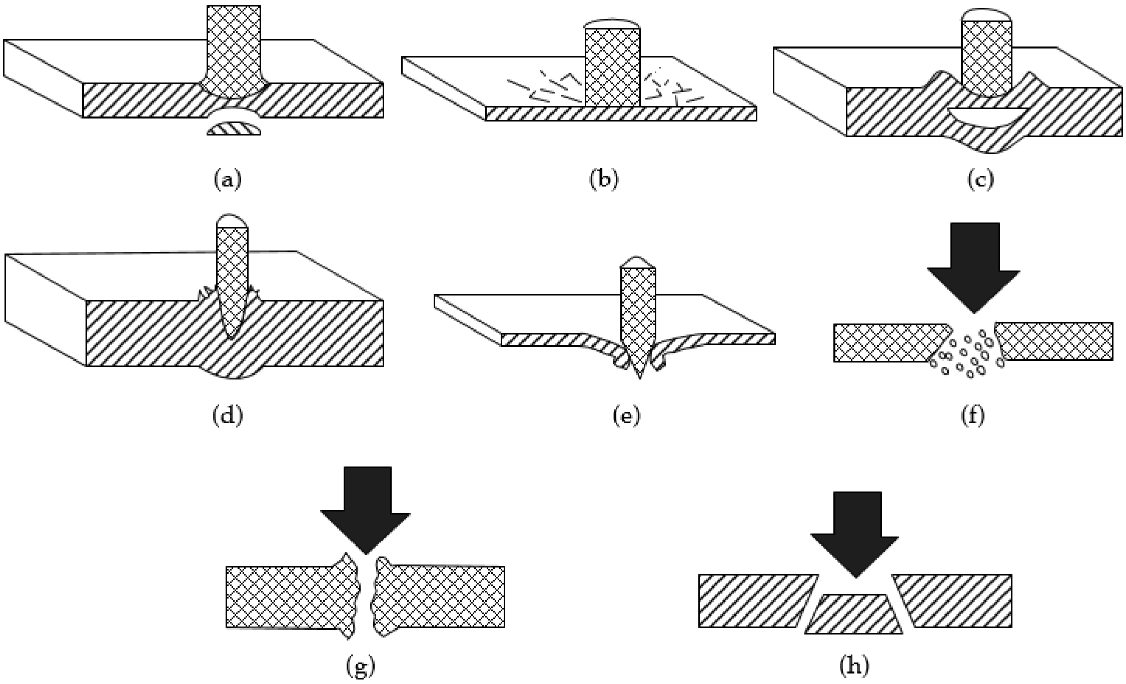

***Figure 2.7*** *Common failures occurring in projectile impact (a) Fracture due to initial stress wave, (b) Radial fracture, (c) Spall failure, (d) Petaling (Frontal), (e) Petaling (Rewarding), (f) Fragmentation, (g) Ductile hole enlargement and (h) Plugging*

### 2.5.2 Johnson-Cook Material Model

Johnson and cook [41] developed a constitutive model and data for metal subjected to large strains, high strain rate, and high temperature. Johnson-cook constitutive equations were used to model the behaviour of tubes. This relation is pre-implemented in FE codes. The equations can be described as,

$$\sigma = (A + B\varepsilon^{n})\left(1 + C\,ln\,\dot{\varepsilon}_{p}\right)(1 - T^{*m}) \tag{2.17}$$

where the $\sigma$is the yield stress, $\varepsilon$is the equivalent plastic strain, $\dot{\varepsilon}_p$ is the plastic strain rate for $\varepsilon_0 = 1$ and $T^*$is the absolute temperature and given by equation 2.18,

$$T^* = \frac{T - T_{\text{room}}}{T_{\text{melt}} - T_{\text{room}}} \tag{2.18}$$

$A$, $B$, $C$, $m$, $n$ are constants and obtained by a mechanical test such as isothermal tension and torsion tests. $A$ and $B$ is the yield strength parameters, $n$ represent the effects of strain hardening, m is the thermal softening index, $T_{\text{room}}$ is the room temperature, $T_{\text{melt}}$ is the melting point temperature, and $C$ is the strain rate constant,

The equation of state is required to simulate material behaviour accurately. Johnson-cook material model requires an equation of state to define pressure as a function of density. EOS is characterized by very high strain rates, and material pressure is more than the yield stress. A linear polynomial is used to simulate the FE model and given by equation 2.19,

$$P = C_0 + C_1\mu + C_2\mu^2 + C_3\mu^3 + (C_4 + C_5\mu + C_6\mu^2)E \tag{2.19}$$

where terms $C_2\mu^2$ and $C_6\mu^2$ are set to zero if $\mu < 0$, $\mu = \rho/\rho_0 - 1$, and $\rho/\rho_0$ is the ratio of current density to reference density, $\rho$ is a nominal or reference density and E is internal energy per unit reference volume.

### 2.5.3 Failure Model

Fracture prediction within the numerical models can be handled by the failure models. Failure models are fundamental elements in numerical simulation for material failures in a high strain rate. The models are divided into two categories one is microscopic models based on continuum mechanics and macroscopic constitutive models based on experimental data. A large number of failure models are available in the literature, but some of them gained more applications in the numerical simulations. Few macroscopic failure models such as Johnson-Cook, Bao-Wierzbicki, Modified Cockcroft-Latham, and Wilkins failure models are described and implemented into ABAQUS and applied to model the failure process of steel and an aluminium target plate by a high-speed projectile by Teng and Wierzbicki [42]. A two-dimensional finite element model was built using an axisymmetric element. The authors examined the numerical results with experimental results that are available in the literature. They concluded that the Wilkins fracture model predicts the spallation of the impacted zone; this unrealistic result is due to its power-law form of pressure term. Material fracture properties cannot be fully characterized by the modified Cockcroft-Latham fracture model as the various tensile test on round bars do not give consistent critical damage. The Johnson-Cook and Bao-Wierzbicki fracture models formulated in the space of stress triaxiality and the equivalent plastic strain to fracture are capable of predicting the realistic fracture pattern and correct residual velocities. Amongst all other models, the JC fracture model predicts two clean cuts through the target thickness, and the whole impacted zone is ejected as a plug. The capture failure patterns are consistent with experimental observations. The residual velocities are close to the experimentally measured ones.

#### 2.5.3.1 Johnson-Cook Failure Model

Johnson-Cook (JC) model is described by equation 2.20, it expresses the strain to fracture as a function of the strain rate, temperature, and pressure [43].

$$\varepsilon_f = \left(D_1 + D_2\, exp\left(D_3\left(\frac{P}{\sigma_y}\right)\right)\right)(1 + D_4 ln\dot{\varepsilon})(1 + D_5 T^*) \tag{2.20}$$

Where $\varepsilon_f$ is the fracture strain, $P/\sigma_y$is stress triaxiality parameter, $\dot{\varepsilon}$ is strain rate, and $T^*$ is the absolute temperature. The constants $D_1$to $D_5$ are material constants and obtained from the experiment. Damage parameter $D$ is described by equation 2.21,

$$D = \sum \frac{\Delta\varepsilon^p}{\varepsilon_f} \tag{2.21}$$

The damage parameter D, i.e., Di ($D_1$, $D_2$…etc.), is calculated using equation 2.21. In this relationship plastic strain increment in each repetition given by

$$\Delta\varepsilon^p = \frac{\sqrt{2}}{3}\left[\sum (d\varepsilon_1 - d\varepsilon_2)^2\right]^{\frac{1}{2}} \tag{2.22}$$

When the damage parameter reaches unity, failure will occur, and the failed element will vanish.

### 2.6 Motivation

The detailed studies and investigation in the literature survey show Electromagnetic perforation of tubes had not been studied. A large amount of FEA and experimental work had been done on EM forming of tubes, including compression and expansion of tubes. Even for the forming and perforation of the tube, no direct mechanical method is available in literature besides some punching machines. In the conventional manufacturing of perforated tubes, the metal sheet is perforated by traditional practices, then rolled and welded into a tube, which is time-consuming. Electromagnetic forming and perforation is a high strain rate perforation process where simultaneous forming and perforation of the tube is possible. In addition to that, now a day the near-net shape manufacturing of components is a need of industrial revolution. The muffler is one kind of example where a deformed shape is required. In conventional manufacturing of muffler tubes, the metal sheet is formed by traditional practices, then rolled and welded into a muffler tube. The muffler produced by this process mostly fails in the region of the weld zone. In this study, experiments are carried out on the EM forming of Al muffler, which results in a single piece of component of the desired shape, hence eliminating the round and linear weld zone to extend the working life of the muffler. Also, by reducing the weld zone weight of muffler is reduced which results in increase in fuel efficiency.

## 2.7 Objectives of Work

The main objective of this work is to design an experimental setup for electromagnetic forming and perforation and to develop a finite element model which can simulate the experimental findings. The primary objective is divided into the following subpart for the accomplishment.

1. Feasibility study of electromagnetic forming and perforation of aluminum tubes.
2. Comparative study and metallographic characterization of aluminum tubes subjected to conventional (low strain rate) and electromagnetic (high strain rate) forming.
3. Finite element analysis to study the shearing mechanism in electromagnetic perforation of aluminum tubes.
4. Experimental investigation and numerical analysis of electromagnetic forming of muffler.

## 2.8 Structure of Thesis

This thesis is organized in seven different chapters. The first chapter provides the introduction along with the working principle of the electromagnetic forming and perforation process. Each chapter in this thesis ends with a summary outlining the achievements and findings which have been either obtained through experimental investigations or verified by numerical simulations. The remainder of this thesis is organized as follows:

- In the chapter 3, the different experimental setup developed during this study, and their working principles are explained. Also, the simulation algorithms used for analysis are described with the help of flow charts for a better understanding of the readers.

- Chapter 4 presents the feasibility study of electromagnetic forming and perforation (EMFP) of Al tubes. The detailed discussion on the study of effect of process parameters on EMFP of Al tubes has been included in this chapter. This chapter concludes that the EMFP combines electromagnetic forming with electromagnetic perforation, which can replace the conventional manufacturing of deformed perforated tube.
- In chapter 5, a comparison of EMFP with a quasi-static or low strain rate process is reported. In particular, the detailed comparison of sheared edge zones developed in electromagnetic and Quasistatic die-less perforation is included in this chapter.
- In chapter 6, the FEA analysis of electromagnetic forming and perforation process has been carried out with the help of a non-coupled and coupled simulation method separately. The comparison of these methods is carried out, and numerical results are validated with experimental results. The numerical analysis will help to study the failure mechanism and the material movement of the EMFP process.
- Earlier the feasibility study of electromagnetic forming of tube is carried out where punches were used. In the chapter 7, a novel approach for modeling the electromagnetic perforation has been used to study the shearing mechanism involved, optimum energy and the pressure required for punch-less electromagnetic perforation. The punch-less shearing process can eliminate the burrs and slivers from the sheared part.
- Chapter 8 consists of the experimental and numerical investigation of electromagnetic forming of muffler tube. The muffler is a part of the noise reduction system placed in the IC engine. This study aims to develop EM forming of Al muffler setup, which results in a single piece of component of desired shape, hence eliminating the disadvantages of conventional manufacturing of muffler and ultimately to extend the working life of muffler.
- Conclusions and scope of future work are presented in Chapter 9, followed by a list of publications and reference

# Chapter 3

# Experimental Methodologies and Simulation Procedures

## 3.1 Introduction

In this thesis work three different experimental setups are developed and used for the experiments. First, the electromagnetic forming and perforation setup is used for the feasibility study of electromagnetic forming and perforation of Aluminium tubes. Second, the electromagnetic forming setup is used for the muffler tubes expansion and third, a supportive punch holder, v die arrangement is developed and used for quasi-static perforation experiments. For the numerical analysis, two different simulation models are developed for electromagnetic forming and perforation process. One is coupled simulation model and other is non-coupled simulation model. In this chapter the different experimental setup and their working principles are explained. Also, the simulation algorithms used for analysis are explained with the help of flow charts for the better understanding of the readers.

## 3.2 Experimental Methodology

### 3.2.1 Electromagnetic Forming Machine

The EM forming machine is used for the experiment. It has a capacitor bank of 90 μF capacitance which can be charged up to 15 kV. The EM forming system consists of an energy store unit, control unit, coil, and measurement unit. Two capacitors having 45 μF capacitance are used for storing the energy. An oscilloscope is used in measurement unit which displays the variation of current with time. The EM processing system used for this study is shown in figure 3.1. The display control unit is also called as Human Machine Interference (HMI). The control unit displays the control for controlling the energy to be discharged through coil. After closing the connection, the capacitor bank discharges current through the coil for the required forming operation. The coil is used for transferring the energy through the workpiece and provides the interaction with workpiece. The coil is made out of pure Cu material and turns are properly insulted to avoid spark generation. The shape and dimensions of the coil are decided as per the requirement of forming operations. A Rogowski coil, an integrator and oscilloscope are used in measurement unit. Rogowski coil is used for the measurement of alternating current. The integrator is connected to the Rogowski coil to provide voltage proportional to current. The output of integrator is further connected to the oscilloscope input channel and the current waveform is displayed.

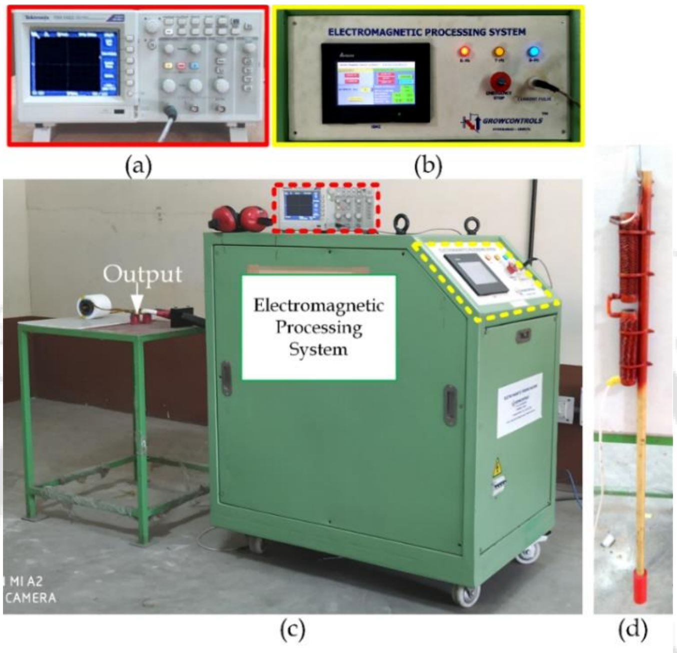

(a) (b) (c) (d)

***Figure 3.1*** *Electromagnetic processing system (a) Oscilloscope, (b) Control unit, (c) EM forming machine and (d) Safety stick*

The figure 3.2 shows the inside of EM processing system. The machine circuit is referred as primary system circuit and the induced circuit is called as secondary circuit. the detailed working principle of the EM forming process is explained in chapter 1 section 1.2.3.

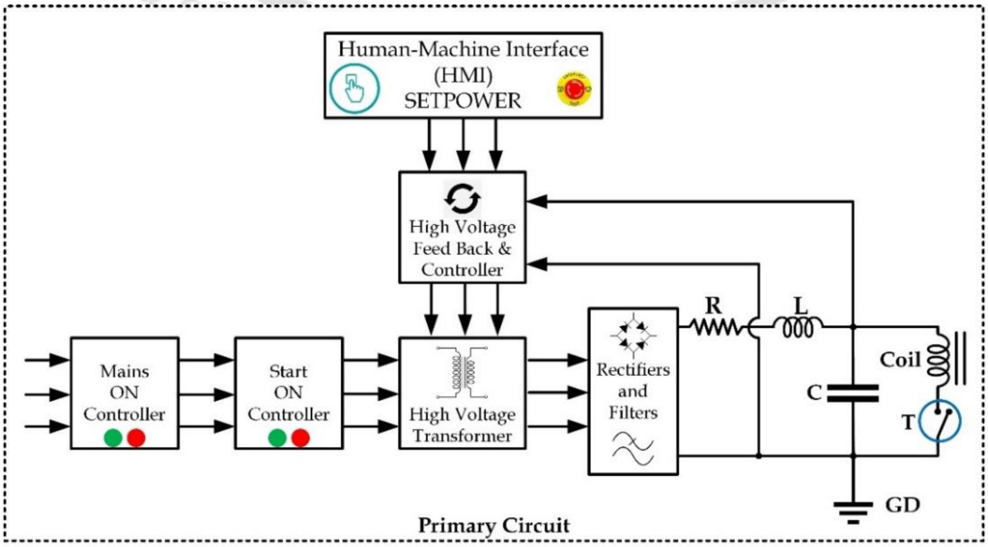

***Figure 3.2*** *Inside of EM processing system*

### 3.2.2 Electromagnetic Forming and Perforation Setup and Working Principle

The schematic representation of electromagnetic forming and perforation setup is shown in figure 3.3. The electromagnetic perforation setup comprises high voltage discharge unit, coils, punches and specially designed die. The coil is used as a tool to use EM field; die is used for getting the desired shape and perforation is done by using a punch.

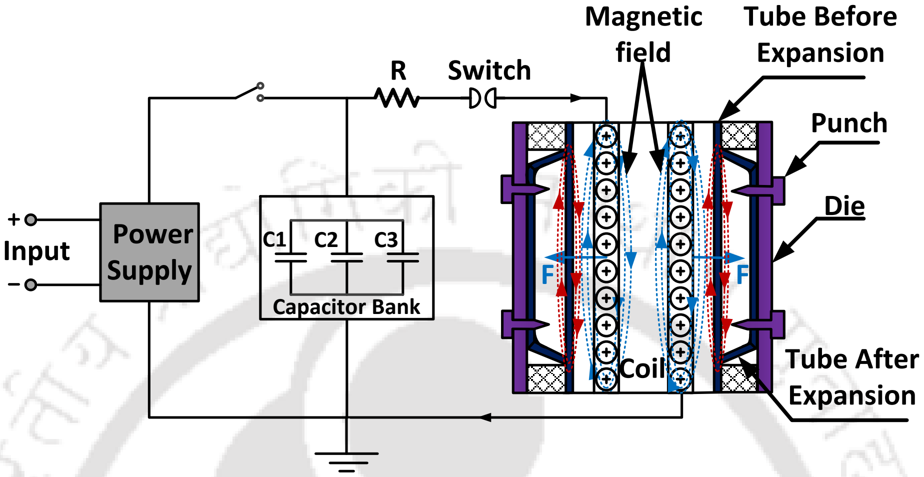

**Figure 3.3** Schematic representation of EM perforation of tube setup

The capacitor bank is charged from a DC power supply. The stored discharge energy in the capacitor bank is discharged through the work coil in short time. This current flowing through the coil produces a magnetic field. This magnetic field induces eddy current into the conductive workpiece resulting in the establishment of another magnetic field. The two magnetic fields oppose each other, the repelling force between the coil and tube (workpiece) causes the expansion of the tube. Punches were located around the tube using a die. While the expansion of tube, it gets perforated by the punches.

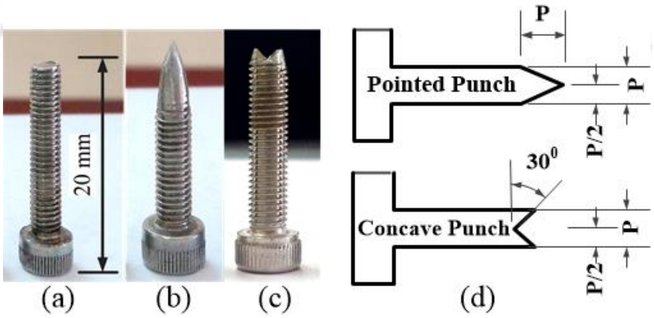

***Figure 3.4** (a) M5 Allen screw, (b) Pointed punch, (c) Concave punch and (d) Punch geometries*

Al tube having 50 mm outer diameter, 1.5 mm thickness and 100 mm length was used as workpiece. The copper coil of 46 mm outer diameter with 10 number of turns and 100 mm in length was used for the experiment. The copper end lugs were used to connect the coil to high voltage terminals leading from capacitor bank. Two types of punches were manufactured named pointed punch and concave punch respectively. By grinding and filing operations, screws were sharpened to get the geometry as shown in Figure 3.4. After the preparation of punches, they were fitted in the array of holes drilled on the die.

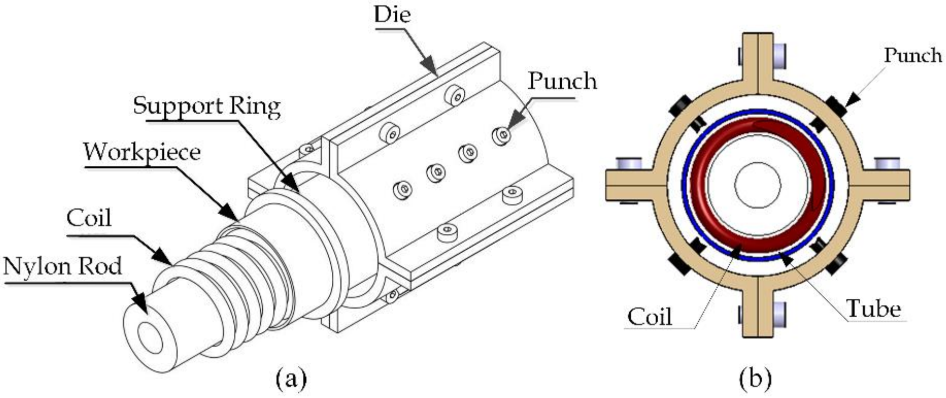

***Figure 3.5*** *(a) Exploded assembly view, (b) Cross section of the setup*

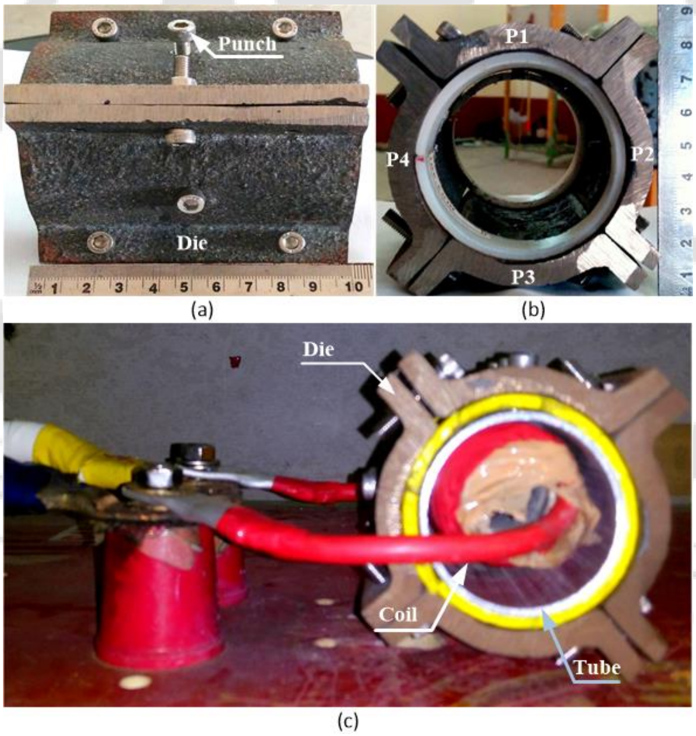

***Figure 3.6*** *Die (a) Top view, (b) Front view and (c) Setup ready for the experiment*

Assembly drawing and an exploded view of EMFP of tube setup are shown in Figure 3.5. Die was manufactured by a casting process. The material used for the die is cast iron. The length of the die is 100 mm, and total 12 holes were drilled on the periphery of the die. Holes were tapped with 5 mm tapping tool. For easy removal of the tube after the operation, die is divided into four parts. Figure 3.6 shows the coil, die front view and complete setup ready for the experiment.

### 3.2.3 Electromagnetic Forming of Muffler Tube Setup and Working Principle

Equivalent circuit diagram for electromagnetic forming of tractor muffler process is shown in figure 3.7. A high voltage power supply is used for charging the capacitor bank. After the charging, the stored energy is discharged through the coil. The resultant current flowing through the coil produces the electromagnetic field around the coil. The magnetic field produced by the coil induces the eddy current into the conductive workpiece which results in a secondary magnetic field. The magnitude of the secondary magnetic field is in the opposite direction of the primary one. The interaction of these two magnetic fields with eddy current produces Lorentz force. For large current the magnitude of produced force overcomes the yield strength of workpiece to fill the gap between the tube and die.

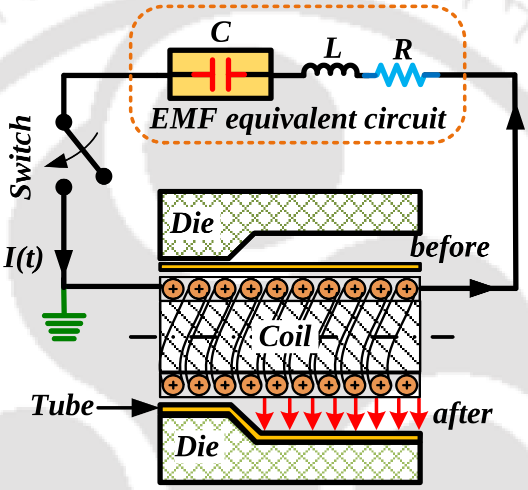

***Figure 3.7*** *Schematic representation of EMF of tractor muffler setup*

The setup of electromagnetic forming of muffler tube consists of a capacitor bank, Cu cable coil, Al tube as a workpiece and the cast iron die. Here, for the expansion of the tube the coil is placed inside the tube and tube is placed inside the die.

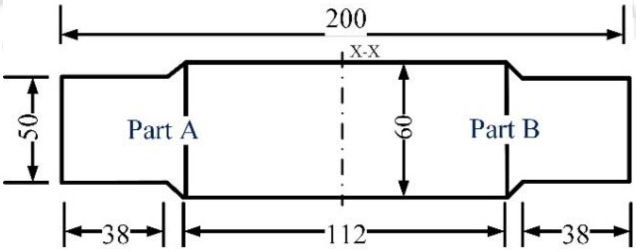

***Figure 3.8*** *Muffler (All dimensions are in mm)*

Figure 3.8 shows the muffler to be manufactured with an electromagnetic forming process. The muffler is symmetric about the X-X cross section. In the present study, the manufacturing of muffler is done in two stage. In the first stage, part A is formed, and in the next stage, part B is formed. Al 6061-T6 tube with the outer diameter 50 mm and 1 mm wall thickness is used as a workpiece. The coil is connected to the high voltage terminal with the help of Cu lugs. The gap between tube and coil, the pitch and cross section of coil effects the deformation. Based on the previous observation the coil has been designed. The experiments are carried out with the help of 47 mm diameter coil made out of 16 mm$^2$ Cu cable and having a length of the 100 mm. The gap between the coil and tube is 1 mm. The 3D model and the cross-section view of die is shown in figure 3.9.

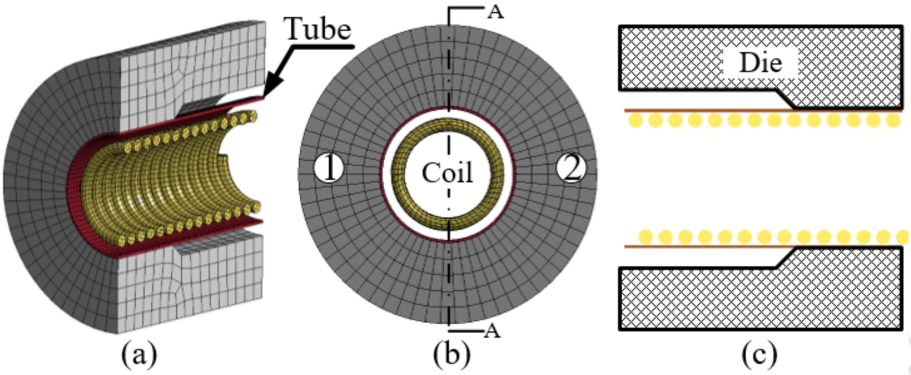

***Figure 3.9*** *EM forming setup model (a)3D model, (b) Front view, (c) Cross section side view*

The cast iron die is manufactured by casting for the experiments. For the easy removal of workpiece, die is divided into two halves and the parts are put together with nut and bolt arrangement. The metal die after manufacturing, and the complete setup are shown in figure 3.10.

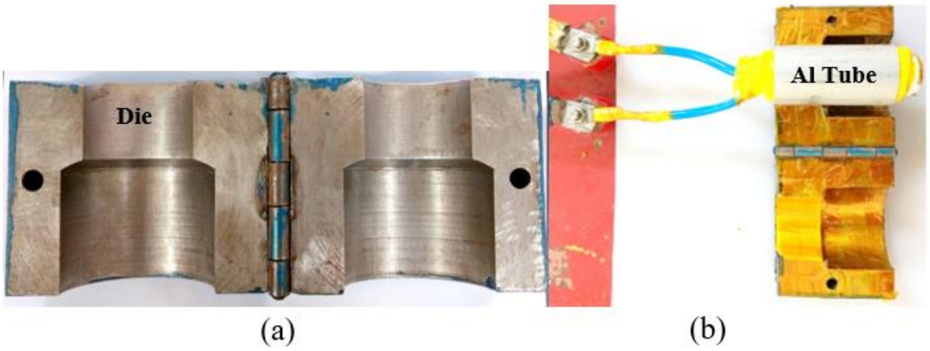

***Figure 3.10*** *(a) Die, (b) Setup prepared for the experiment*

In addition to above for finding out the optimum number of turns of the coil and the optimum stand of distance, different experiments run are carried out with the help of available setup. Figure 3.11 shows the different coils used for the experimental trial runs, and their specification is given in table 3.1. After the successful experimental runs on different coils, it is found that the coil with 10 number of turns having 47 mm external diameter and 100 mm length, the maximum deformation is possible. Hence, for further study, the same coil is used. Experiments are carried out at different discharge energies. Discharge energies are varied from 5.0 kJ to 6.5 kJ for finding out the optimum energy for maximum deformation. It is observed that the minimum energy required to deform the tube is 5.0kJ, and the maximum gap-filling is observed at 6.2 kJ discharge energy. Further increase of discharge energy leads to failure of the tube. The obtained current values are further used as input in Ansys Maxwell and LS-DYNA for magnetic field analysis.

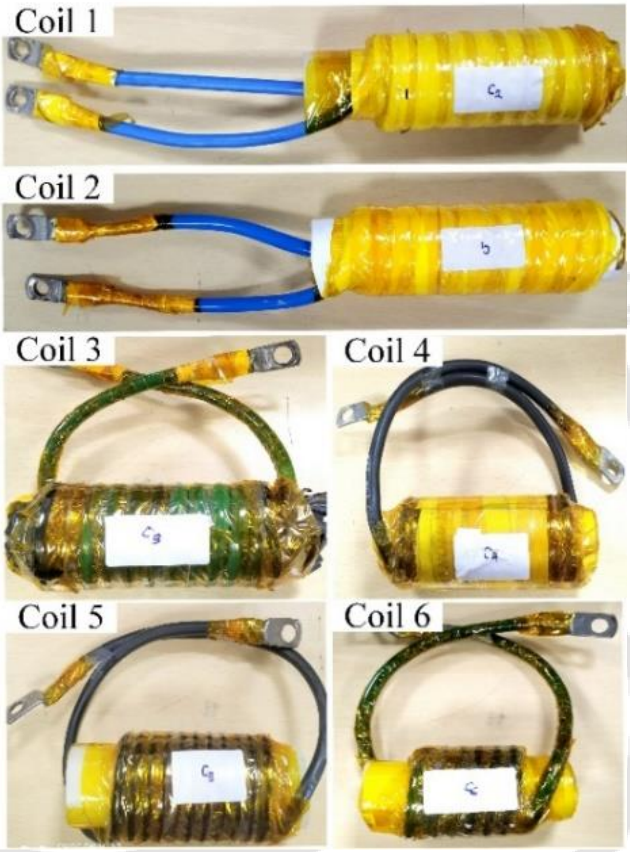

***Figure 3.11*** *Coils*

***Table 3.1*** *Specification of coils*

| Coil | Length | No. of turns | Outer Diameter (OD) |
|---|---|---|---|
| 1 | 100 | 10 | 45 |
| 2 | 100 | 10 | 46 |
| 3 | 100 | 10 | 47 |
| 4 | 90 | 9 | 46 |
| 5 | 80 | 8 | 46 |
| 6 | 60 | 6 | 46 |

### 3.2.4 Experiments on Quasi-Static Die-less Perforation of Tubes

In this section, conventional perforation at the quasi-static loading rate (10mm/min) is studied with a separate experimental setup built using a Universal Tensile Machine (UTM).

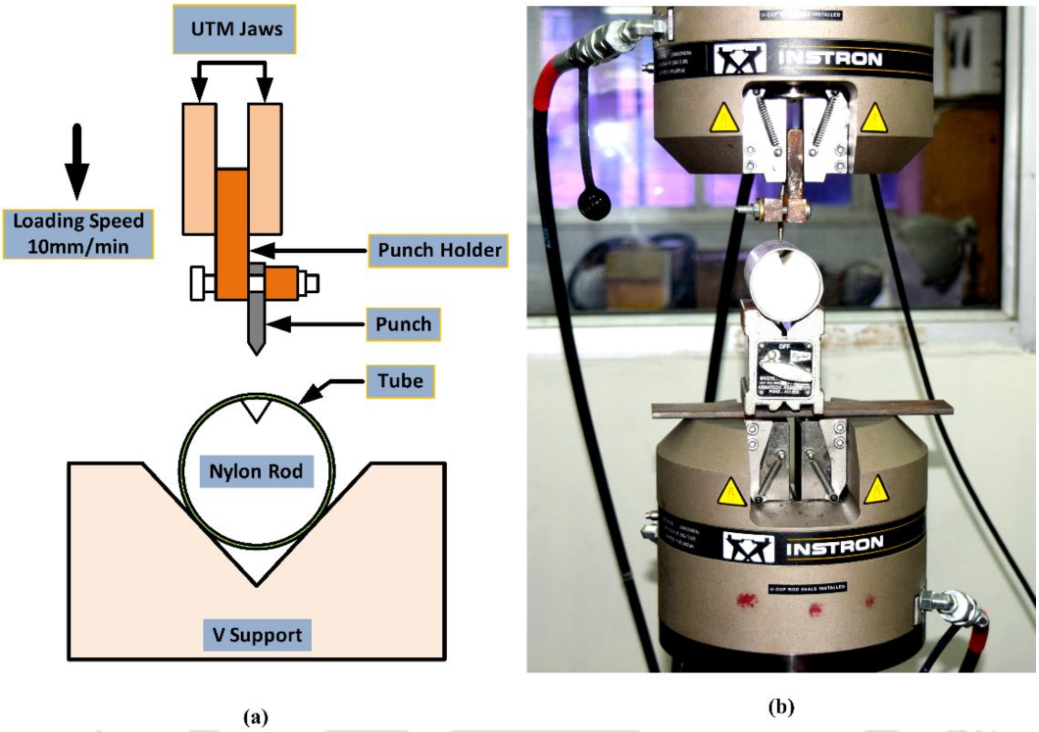

(a) (b)

***Figure 3.12*** *Quasi-static die-less perforation setup, (a) Model and, (b) Experimental setup*

The setup consists of punches, punch holder to hold punches, V support, nylon rod, and Al tube as shown in Figure 3.12 (a) and (b). A nylon rod having diameter same as the internal diameter of the tube is used to support the Al tube, and V support is used for resting and holding the workpiece. A slot is created on the nylon rod for the easy travel of punch.

### 3.3 Simulation Models

EM forming is carried out within microseconds, and it is very difficult to find out the strain behavior, the velocity of workpiece and deformation pattern experimentally. To estimate these parameters numerically, two different simulation algorithms namely coupled simulation model and non-coupled simulation model are developed. The details about both the simulation model and their working principle is discussed in this section. The details of the computer system and computational softwares used are as mentioned in Table 3.2.

***Table 3.2*** *Details of system and software used*

| **Information** | **Details** |
|---|---|
| System | HP Z4 G4 Workstation, Intel$^R$ Xeon$^R$ W2145 Processor, Intel C422 Chipset and 64 GB ECC DDR4 RAM. |
| Softwares | LS-DYNA$^{TM}$ Version R11 EM Module, Ansys Explicit Dynamics and Ansys Maxwell. |

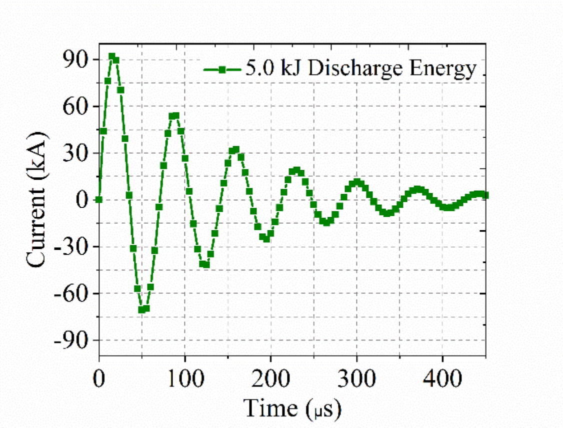

***Figure 3.13*** *Current curve obtained at 5.0 kJ discharge energy*

The current waveform obtained from the oscilloscope during the experiment is used as input in both coupled and non-coupled simulation model. Figure 3.13 shows the current waveform obtained at 5.0 kJ discharge energy. The exponential decay of the current peaks is because of the resistance of the circuit. The current is maximum during the first half period of the waveform. To balance the zero resistance assumptions and for the simplicity of numerical calculations, the first half of the sine curve is considered for the simulations. The reason behind this consideration is the work hardening of the material and high damping current makes the effect of further oscillation insignificant for producing plastic strain required for further deformation.

### 3.3.1 Coupled Simulation Model

As discussed in literature review it is observed that for more accurately simulating the electromagnetic forming processes, many researchers have used coupled simulation model. Here in this research work this coupled simulation model has been used for finite element analysis of electromagnetic forming as well as perforation process. For simulating above processes, the EM module available in the LS-DYNA™ explicit dynamics software is used. In LS-DYNA™, both electrical, as well as mechanical solution takes place, so it is called a coupled simulation. The dynamics of the electromagnetic field is taken care by the electromagnetic module, and the mechanical module deals with the structural deformation.

The detailed flow chart of coupled behavior is given in figure 3.14. In the coupled simulation, FEA analysis of EM forming and perforation is carried out in two loops as shown in the flow chart. Here, in this model at every time step, the Lorentz forces are evaluated at each node and simultaneously, they are automatically transferred as an input load for structural deformation. In mechanical solver, applied pressure deforms the tube and the deformed geometry is updated in EM module which again modifies the electromagnetic field. Further, this modified EM field affects the structural deformation and these iterations continue until convergence is achieved.

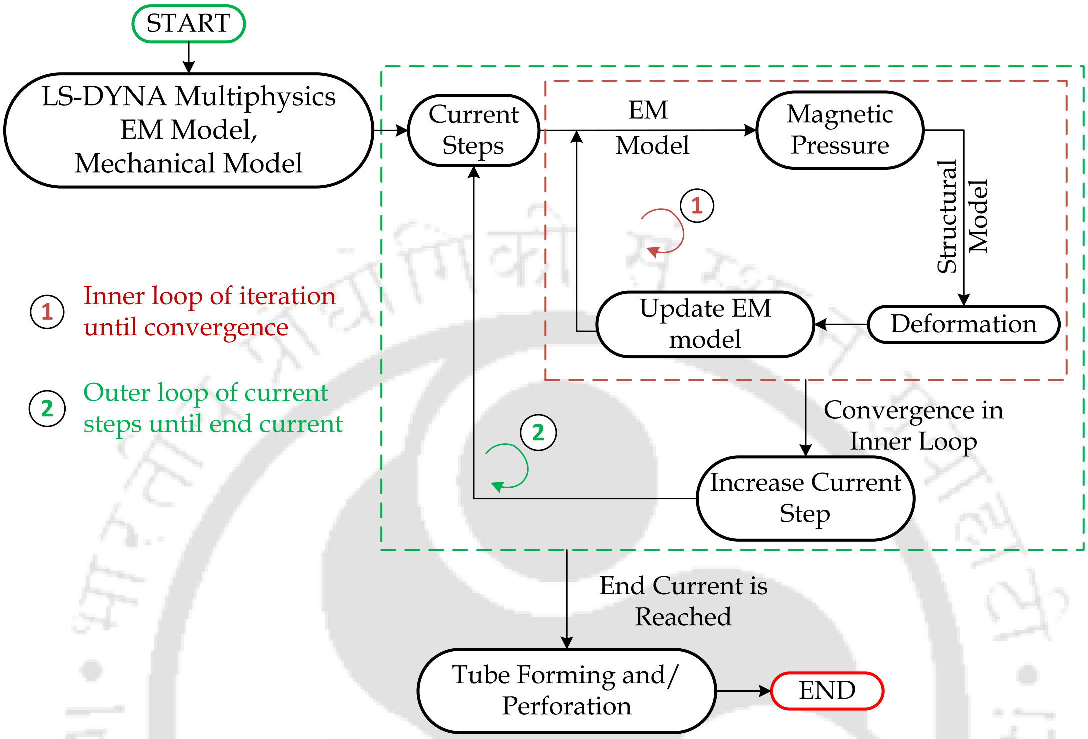

***Figure 3.14*** *Coupled behavior in LS-DYNA™*

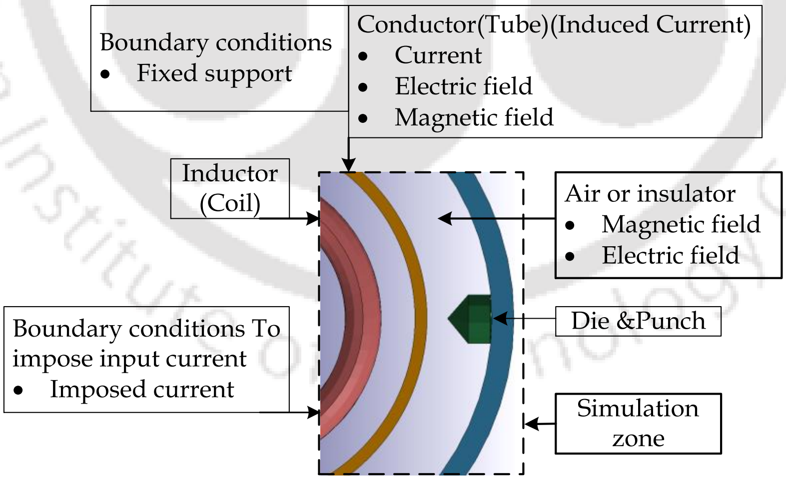

***Figure 3.15*** *Different simulation zones in the coupled simulation process*

The different simulation zones in the coupled simulation are shown in figure 3.15. In LS-DYNA, the electromagnetic field is solved using a Finite Element Method (FEM) combined with the Boundary Element Method (BEM). Here, BEM is used for surrounding air or insulator. The significant advantage of using the BEM for the air analysis is that it does not require air mesh, which avoids the mesh complications. A finite element formulation is used for solving the thermo-mechanical problem. The equation of motion is given and addressed in an explicit model of LS-DYNA as explained in the manual [44].

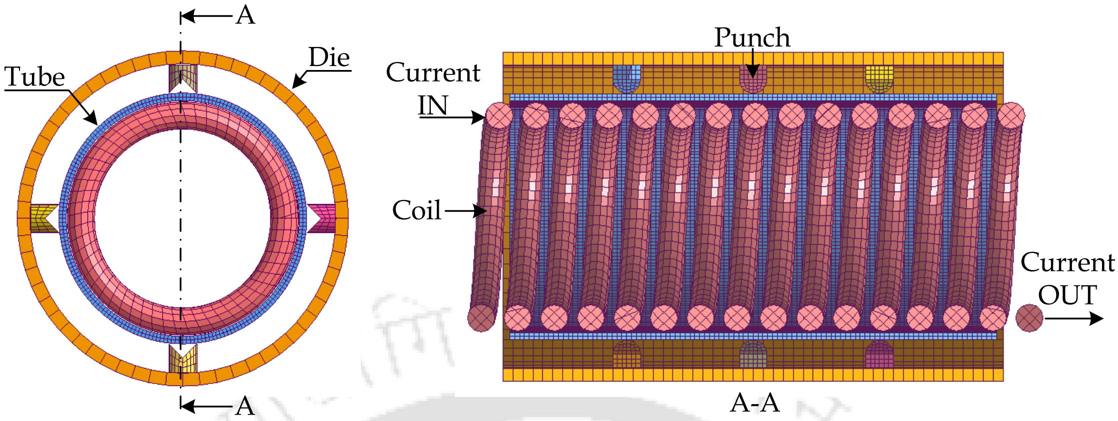

***Figure 3.16*** *Cross-section views of the 3D model used in coupled simulations of EM forming and perforation of tube*

As shown in figure 3.16, 3D model used for electromagnetic forming and perforation of tubes, consists of tube, coil, punches and die. The current input and output segments have to be specified in LS Dyna. Because of the limitation of coupled simulation software, only quad type of elements is used for meshing all parts [45]. Time step and mesh convergence study is carried out and optimum mesh size and time steps are used for all the simulations. Al 6061-T6 material is used for the tube, Cu is used for the coil and SS-304 is used for the punch.

Fracture prediction within the numerical models can be handled by the failure models. Here, the Johnson-cook failure model is used where, the equivalent strain is the function of strain rate, stress, temperature and damage constants. The constitutive equation of the failure model is given by eqn. (2.20).

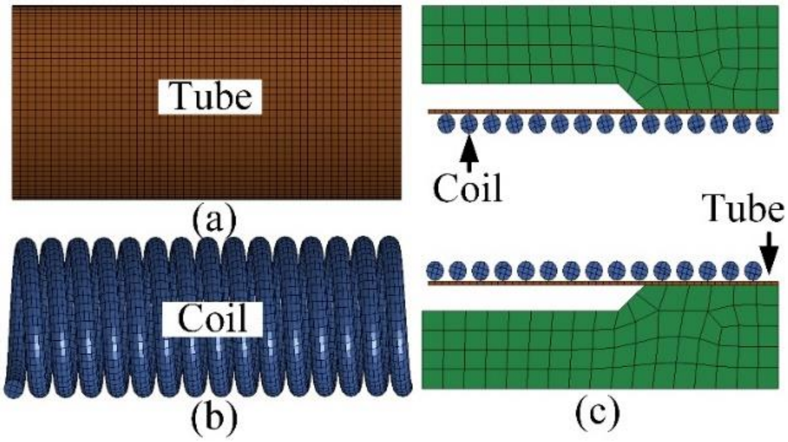

***Figure 3.17*** *Cross-section views of the 3D model used in coupled simulations of EM forming of muffler tube*

The cross-section views of the 3D model used in coupled simulations of EM forming of muffler tube is shown in figure 3.17. It consists of die, coil and tube. The current applying procedure is same as that of explained in above. The coil and die are made rigid as we are interested in tube deformation. The boundary conditions applied are shown in figure 3.18.

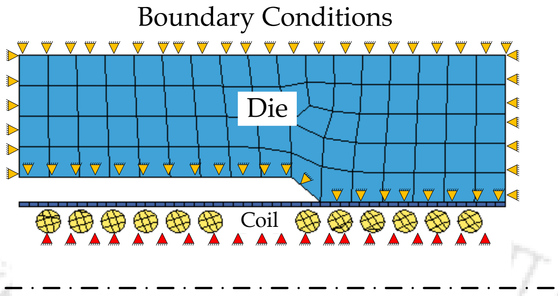

***Figure 3.18*** *Boundary conditions applied*

### 3.3.2 Non-Coupled Simulation Model

In non-coupled simulation approach, two simulation softwares, Ansys Maxwell and Ansys Explicit Dynamics are used, where the electromagnetic part is simulated by ANSYS Maxwell and structural part is solved in ANSYS Explicit Dynamics. The flow chart of non-coupled simulation is shown in figure 3.19.

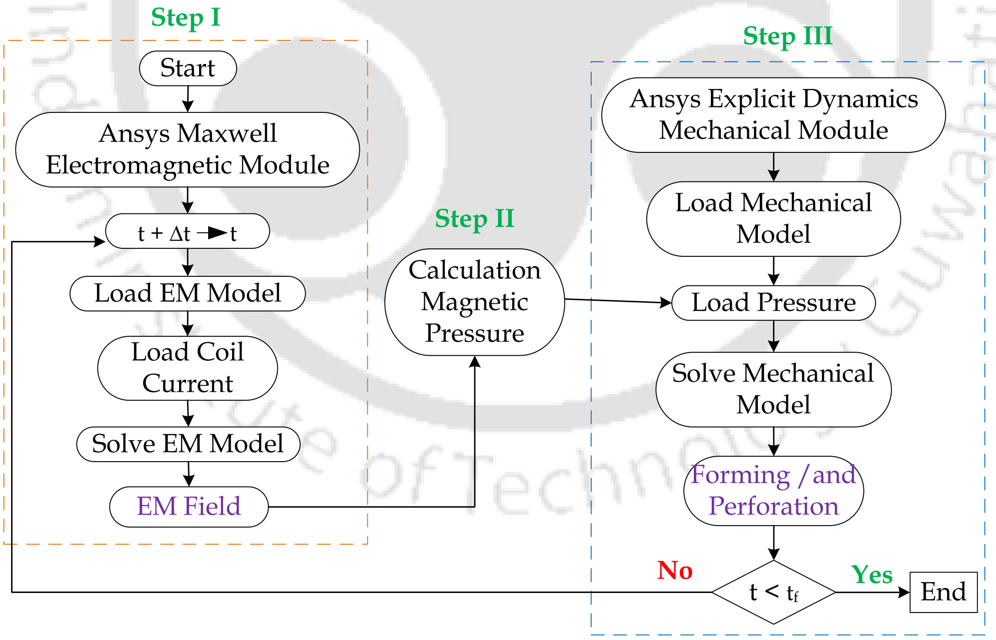

***Figure 3.19*** *Flowchart of the non-coupled simulation*

The magnetic field generated around the coil is determined in ANSYS Maxwell software. The current obtained from oscilloscope is applied through terminals of the coil. Figure 3.20 shows the coil-tube setup used in Ansys Maxwell. In the experiment, for deforming the tube, the electromagnetic forming system is used. It consists of a capacitor bank $C_0$, output terminal, connection lines with resistance, inductance $L_c$, and coil. The forming coil ($R_1$, $L_1$) is coupled with the tube ($R_2$, $L_2$). The equivalent circuit diagram of the EMF process is presented in figure 1 (b) The following equation (3.1) and equation (3.2) describes the coupled behavior between coil and tube [45].

$$(L_1 + L_c)\frac{di_1}{dt} + \frac{d}{dt}(Mi_2) + (R_1 + R_c)i_1 + \frac{1}{C_0}\int_0^t i_1 dt = 0 \tag{3.1}$$

$$\frac{d}{dt}(L_2 i_2) + \frac{d}{dt}(Mi_1) + R_2 i_2 = 0 \tag{3.2}$$

where $M$ is the mutual induction between the coil and the tube, $i_1$ is the current passing through the coil, $i_2$ is the total current induced in the tube. The initial conditions used for solving equation (3.1) and equation (3.2) are given as,

$$i_1 = 0, (L_1 + L_c)\frac{di_1}{dt} = V_{0,}\ i_2 = 0 \tag{3.3}$$

where $V_0$ is the initial voltage.

Mutual inductance $M$ used in equation (3.1) and equation (3.2) represent the magnetic coupling between the coil circuit and the workpiece circuit. In the coupled analysis, the mutual inductance $M$and workpiece inductance $L_2$ changes with structural deformation of the workpiece and vice versa this deformation dependent on $M$ and $L_2$. Solving these complex equations is very difficult and time-consuming. Hence, to simplify this problem in non-coupled simulation, it is assumed that the workpiece inductance and mutual inductance does not depend on the workpiece deformation. After this assumption, the equation of the current is reduced to equation (3.4) [44].

$$L_T\frac{di_c}{dt} + R_T i_c + \frac{1}{C_c}\int_0^t i_c dt = V_0 \tag{3.4}$$

with initial conditions,

$$i_c = 0, \left[L_T\frac{di_c}{dt}\right]_{t=0} = V_0$$

By solving equation (3.4), the resultant current passing through the coil can be obtained by following equation (3.5).

$$i(\mathrm{t}) = \frac{V_0}{\omega L_\mathrm{T}}e^{-\beta t}\sin(\omega \mathrm{t}) \tag{3.5}$$

where, $\omega = \sqrt{\frac{1}{L_T C_T} - \left(\frac{R_T}{2L_T}\right)^2}$

where $R_T$ ,$L_T$, $C_c$ are the total resistance, inductance and capacitance of the system, respectively and $i_c$ is the current passing through the coil. Further, the Maxwell's equations can be used for the describing electromagnetic behavior within a conductive medium.

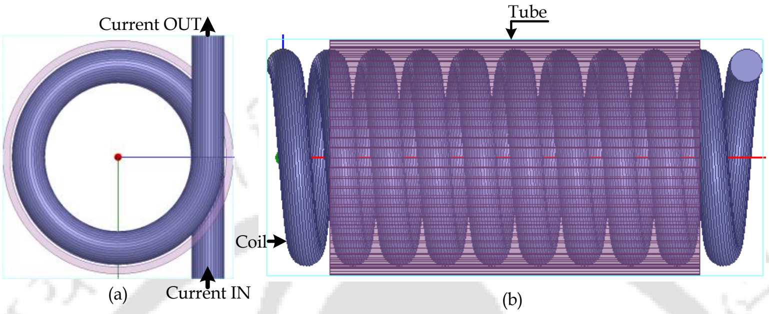

***Figure 3.20** 3D model used in ANSYS Maxwell (a) Top view, (b) Front view*

The magnetic field intensity obtained from Ansys Maxwell is converted into its equivalent transient magnetic pressure using analytical relation between magnetic field and pressure as given in equation (3.6) [46].

$$P = \frac{1}{2}\mu_0 H^2 \tag{3.6}$$

This magnetic pressure is directly applied in ANSYS Explicit Dynamics simulations for expanding the tube. The 3D model used in Ansys Explicit Dynamics for the simulation of EM forming and perforation is shown in figure 3.21.

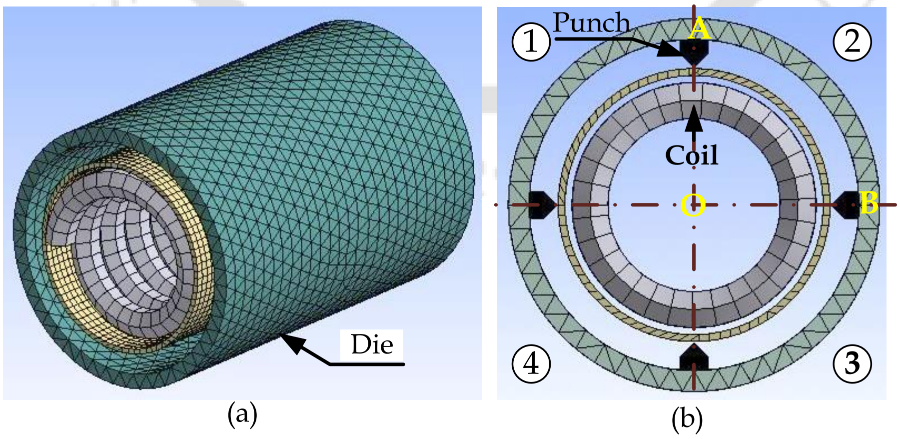

(a) (b)

***Figure 3.21** (a) Full 3D model of setup, (b) Symmetrical cross-sectional view*

To reduce the computational cost and time, the symmetry of the problem is used with proper boundary condition., which gives the freedom to do the simulation on the quarter-cylindrical part. The axial and radial symmetry boundary conditions applied to the quarter model are shown in figure 3.22.

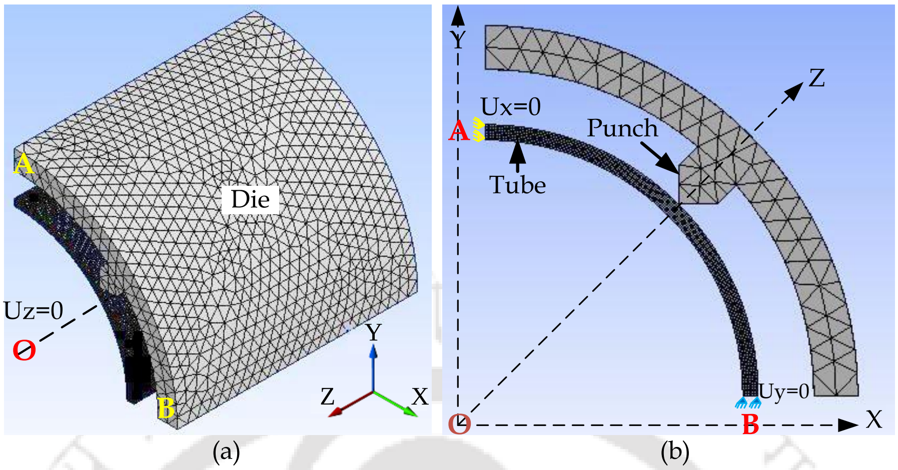

***Figure 3.22*** *Symmetrical boundary conditions (a) Selected section AOB, (b) Front view*

In the simulation of EM forming of muffler tube, the magnetic pressure is calculated in the similar way and applied inside the workpiece in the Ansys Explicit Dynamics. The 3D model used in Ansys Explicit Dynamics simulation is shown in figure 3.23. Here die is fixed in all the directions.

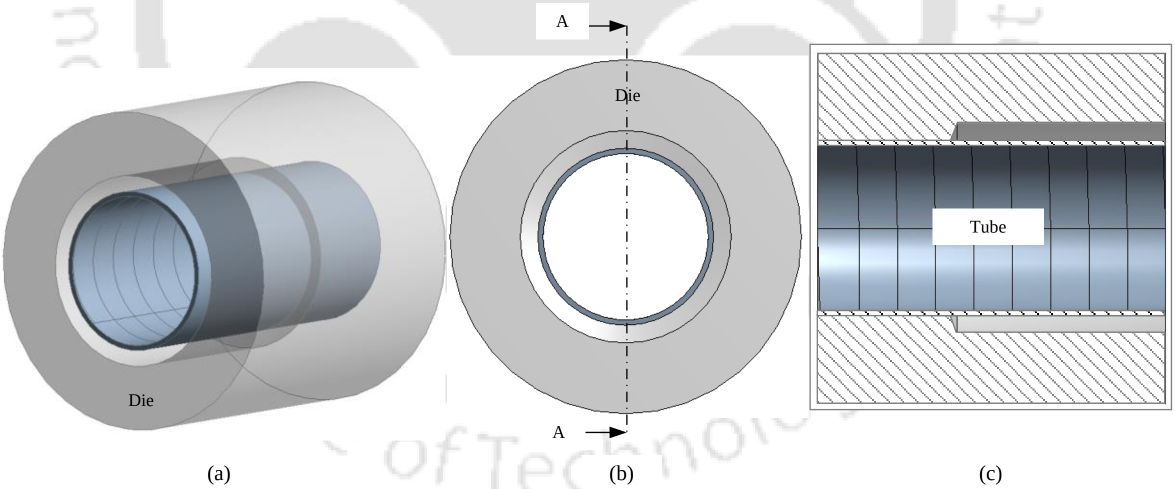

***Figure 3.23*** *3D model used in Ansys explicit dynamics (a) Isometric, (b) Front and (c) Cross-section view.*

## 3.4 Properties of the Materials

In this section different materials and their properties used in the simulations are tabulated in table form. Al 6061-T6 tube is used as workpiece, Cu cable is used to manufacture the coil and dies are made up of ceramic material. The properties of all these materials are given in table 3.3 and table 3.4. EDS analysis is carried out to detect the material composition of the as-received aluminum alloy as shown in figure 3.24.

EDS analysis shows that the as-received aluminum tube has an elemental chemical composition in the range same as Al 6061 T6 [10] alloy.

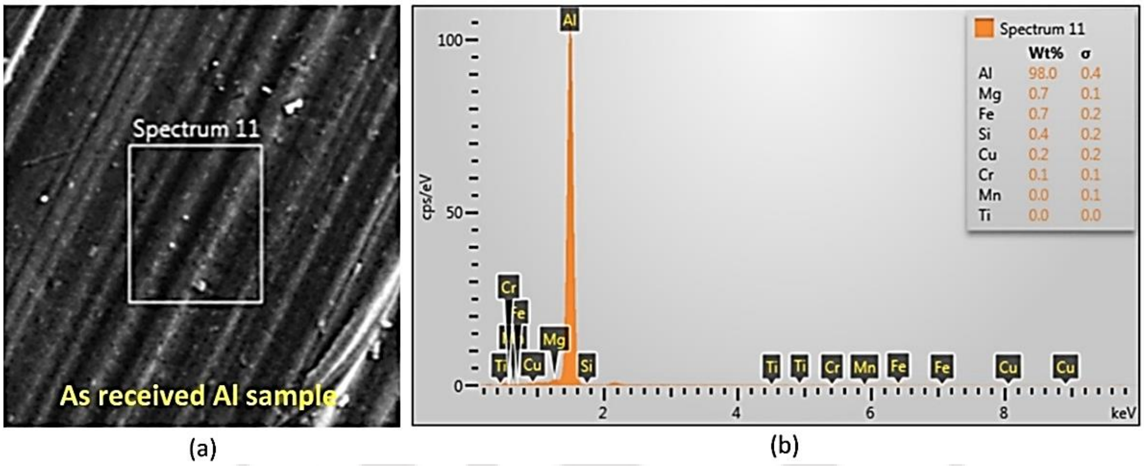

***Figure 3.24*** *EDS analysis of as-received Al alloy, (a) Sample for analysis and, (b) EDS analysis result.*

***Table 3.3*** *Material properties [47]*

| **Material Properties** | **Al 6061-T6** | **Cu** | **SS-304** |
|---|---|---|---|
| Poisson's Ratio ($\gamma$) | 0.33 | 0.33 | 0.3 |
| Melting Temperature (K) | 925 | 1355 | 1673 |
| Density ($kg/m^3$) | 2703 | 8940 | 7900 |
| Specific Heat ($J/kg\ K$) | 885 | 3.935 | 423 |
| Modulus of Elasticity ($GPa$) | 69.8 | 97 | 210 |
| Electrical Conductivity (MS/m) | 25 | 58 | 1.4 |
| Modulus of Rigidity (GPa) | 26 | 45 | 70 |
| Thermal Conductivity (W/m-K) | 126 | 391 | 14 |

***Table 3.4*** *Properties of ceramic material [47]*

| **Material Properties** | **Value** | **Unit** |
|---|---|---|
| Density ($\rho$) | 8940 | kg/m$^3$ |
| Modulus of Elasticity ($E$) | 97 | GPa |
| Poisson's Ratio ($\gamma$) | 0.31 | |
| Heat Capacity ($C$) | 3.935 | J/kg-K |
| Thermal Conductivity ($k$) | 391 | W/m-K |
| Electrical Conductivity ($\sigma$) | 58 | MS/m |

In non-coupled simulation analysis Steinberg-Guinan strength model [20] is used for tube material. The Parameters used in this model are given in table 3.5. The constitutive relations for shear modulus G and yield stress Y for high strain rates are given below,

$$G = G_0\left\{1 + \left(\frac{G_p'}{G_p}\right)\frac{P}{\eta^{\frac{1}{3}}} + \left(\frac{G_t'}{G_0}\right)(T - 300)\right\} \tag{3.7}$$

$$Y = Y_0 \left\{ 1 + \left( \frac{Y_p'}{Y} \right) \frac{P}{\eta^{\frac{1}{3}}} + \left( \frac{G_t'}{G_0} \right) (T - 300) \right\} (1 + \beta\varepsilon)^n \tag{3.8}$$

Subjected to $Y(1 + \beta\varepsilon)^n \leq Y_{max}$

where $\eta$ is compression constant, $T$ is temperature, $\varepsilon$ is an effective plastic strain and the primed parameters with the subscripts $p$ and $t$ are the derivatives of that parameter with respect to pressure and temperature at the reference state (T = 300 K, p= 0, ε = 0). The subscript zero also refers to values of $G$ and $Y$ at the reference state.

***Table 3.5*** *Parameters used in Steinberg-Guinan strength model [47]*

| **Parameters** | **Al 6061-T6** | **Unit** |
|---|---|---|
| Initial Yield Stress ($Y_0$) | 290 | MPa |
| Maximum Yield Stress ($Y_{max}$) | 680 | MPa |
| Hardening Constant ($\beta$) | 120 | |
| Hardening Exponent ($n$) | 0.1 | |
| Derivative dG/dp ($G_p'$) | 1.8 | |
| Derivative dG/dT ($G_t'$) | −17 | MPa/K |
| Derivative dY/dP ($Y_p'$) | 1.8e-2 | |
| Melting Temperature ($T_{melt}$) | 946 | K |

The Johnson-Cook strength model is used for tube material in coupled simulation of EM forming of muffler and the parameters are listed in table 3.6. Fracture prediction within the numerical models can be handled by the failure models. Here, the Johnson-cook failure model is used in coupled simulation of EM forming and perforation of Al tube, where, the equivalent strain is the function of strain rate, stress, temperature and damage constants. The Johnson-Cook failure model is given by equation (2.20). The Damage constants used in this model are given in table 3.7.

***Table 3.6*** *Johnson-Cook strength model parameters [47] Al 6061*

| **Parameter** | A (MPa) | B (MPa) | C | n | m | Tm (K) | $\dot{\varepsilon}$ (Sec$^{-1}$) |
|---|---|---|---|---|---|---|---|
| **Value** | 324 | 114 | 0.002 | 0.42 | 1.34 | 925 | 1 |

***Table 3.7*** *Damage constants used in the Johnson-Cook failure model [47]*

| **Parameters** | $D_1$ | $D_2$ | $D_3$ | $D_4$ | $D_5$ | $T_m$ (˚C) | $\dot{\varepsilon}$ (Sec$^{-1}$) |
|---|---|---|---|---|---|---|---|
| **Value** | -0.77 | 1.45 | 0.47 | 0 | 1.6 | 650 | 1 |

### 3.5 Equipment for Post-Processing

Different kind of machines and setups are used for the post processing. These different types of equipment used are as shown in figure 3.24 to figure 3.29, which were calibrated before taking the readings to avoid any error. The oscilloscope used for current measurement is shown in figure 3.25 (a).

(a) (b)

***Figure 3.25*** *(a) Oscilloscope for current measurement and (b) RLC measuring equipment*

(a) (b)

***Figure 3.26*** *Metallographic specimen molding unit (a) Manual and (b) Automatic*

Equipment shown in figure 3.25 (b) is used for the measurement of resistor (R), an inductor (L), and a capacitor (C). To study the grain structure after the experiment samples are prepared.

(a) (b)

***Figure 3.27*** *(a) Manual and (b) Automatic sample polishing machines*

For the metallographic study specimen preparation i.e. for specimen moulding and polishing, buehlers moulding and grinding machines shown in figure 3.26 and 3.27 are used. After preparation of the samples, for grain structural analysis microscope. The optical microscope and digital microscope are shown in figure 3.28 (a) and (b).

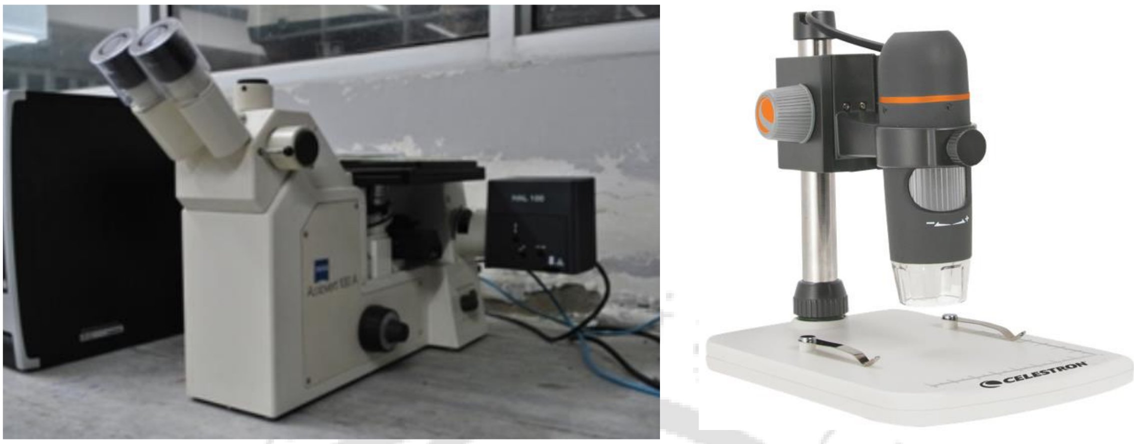

(a) (b)

***Figure 3.28*** *(a) Optical microscope and (b) Digital microscope*

(a) (b)

***Figure 3.29*** *(a) Universal Testing Machine and (b) Vickers hardness testing machine*

# Chapter 4

# Electromagnetic Forming and Perforation of Al Tubes: Experimental Study [I]

## 4.1 Introduction

Electromagnetic forming (EMF) is a high energy rate forming process which utilizes electromagnetic force to deform metal workpiece. In this research work, experiments have been conducted to establish the feasibility of electromagnetic forming and perforation (EMFP) of Al tubes. EMFP combines electromagnetic forming with electromagnetic perforation. For the feasibility study split die, pointed and concave punches have been designed. The detailed study of the effect of process parameters on EMFP of Al tubes has been carried out. The optimum discharge energy has been determined with experimental trials which lead to successful forming and perforation of the tube. The experimental setup, working priciple and methodology are explained in the section 3.2.2.

## 4.2 Results and Discussions

Experiments were carried out on as-received and heat-treated Al tubes at different discharge energies. As-received tubes were not deformed and perforated due to high strength. At higher discharge energies, indentation of punches was observed on the as-received Al tube. The tensile test is carried out as per ASTM E8 standard [48]. Young's modulus of as-received material is 48.9 GPa and tensile strength is 90 MPa. EDS analysis is carried out for finding out the material composition and it is listed in table 4.1.

***Table 4.1*** *EDS analysis result (composition)*

| Al | Cr | Cu | Fe | Mg | Mn | Si | Ti | Zn |
|---|---|---|---|---|---|---|---|---|
| 94.1 | 0.03 | 0.06 | 1 | 1.93 | 0.03 | 3.16 | 0.06 | 0.13 |

To improve its workability, as-received tubes were heat treated by annealing by keeping it for 3 hours at the temperature 412 $^0$C and cooled down slowly in the furnace itself. The complete process takes more than 18 hours. Hardness testing was carried out with the help of Vickers hardness testing machine. After the heat treatment, 19.57 % reduction in hardness of tube was observed. Two sets of experiments were carried out during this work. First set was with the help of 12 pointed punches and second was with 12 concaved punches. In the first set of experiments gap between the tube and die was kept 2 mm. At

---

[I] *Pawar, S., & Kore, S. D. (2019). Electromagnetic forming and perforation of Al tubes. Journal of Mechanical Science and Technology, 33(12), 5999-6007.*

low discharge energy, forming and piercing was observed in the tubes. Discharge energy for various discharge current is as shown in figure 4.1.

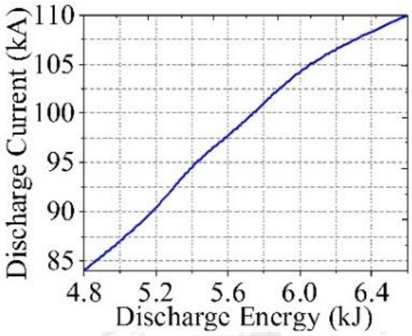

***Figure 4.1*** *Variation of discharge energy for the different discharge current*

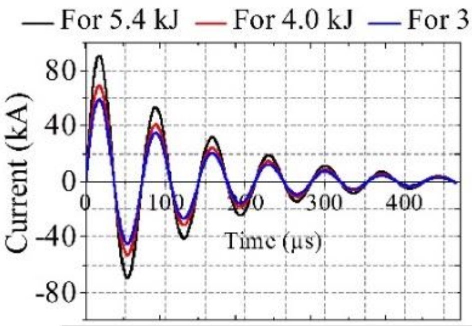

***Figure 4.2*** *Current waveforms for various discharge energy*

The maximum value of current for the first peak was 110 kA for 6.6 kJ of discharge energy. The current values were measured using a Rogowski coil. Figure 4.2 shows the current waveforms obtained from CRO for different discharge energies.

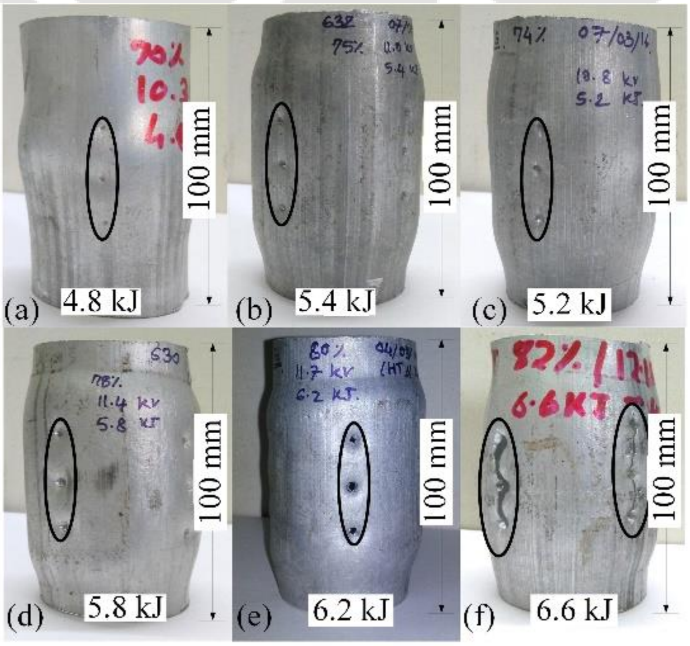

***Figure 4.3*** *Tubes after the experiment at different discharge energy for 12-pointed punch arrangement*

Tubes after the experiment at various discharge energy levels are shown in figure 4.3. As shown in figure 4.3 (e) at 6.2 kJ of discharge energy tube got pierced well, all 12 holes were pierced as shown in figure 4.4. Beyond 6.2 kJ discharge energy, crack was propagated through the perforated hole, and the tube gets failed along the hole because of high energy as shown in figure 4.3 (f).

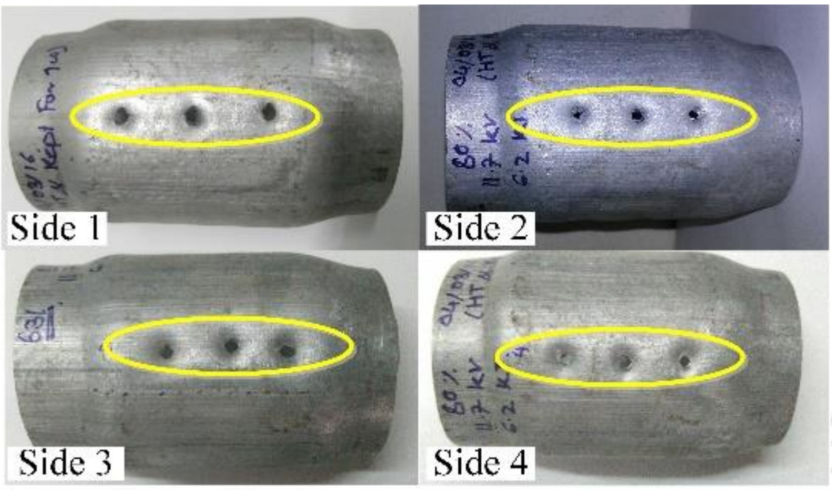

***Figure 4.4** All 12 pierced holes at 6.2 kJ discharge energy for 12 pointed punch arrangement*

From the experiment, it was observed that with the increase in discharge energy, the diameter of tube increases. Increase in diameter is measured at a different point along the length of the tube. The maximum deformed diameter of the tube was 56 mm. Increase in diameter with respective discharge energies is shown in figure 4.5.

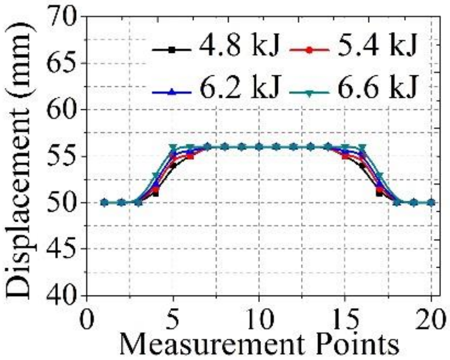

***Figure 4.5** Variation of forming diameter with an increase in discharge energy for 12 pointed punch arrangement*

In another case of EMFP, 12 concave punches were used, and experiments were carried out at varied discharge energy. The distance between tube and die was 3 mm. It was observed that as the discharge energy increases from 5.7 kJ to 6.2 kJ, hole diameter increases but at 6.2 kJ energy crack was generated at the hole edge as shown in figure 4.6 (b).

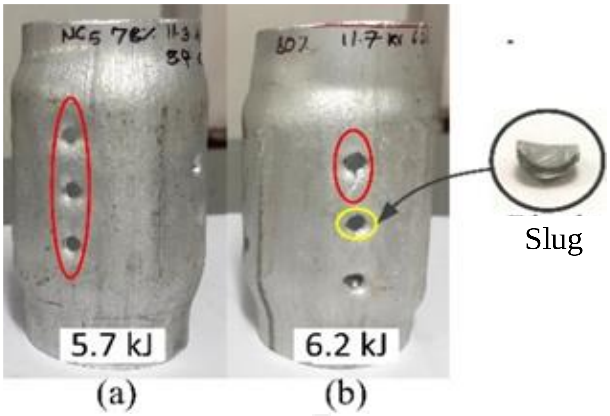

***Figure 4.6*** *Tubes after the experiment for 12 concave punch arrangement at (a) 5.7 kJ and (b) 6.2 kJ*

Perforated hole diameter and number of holes perforated increase with increase in discharge energy. The cross sections of perforated holes are shown in figure 4.7. With the help of pointed punch, Petaling is observed and by the concave punch, separation of the slug is observed.

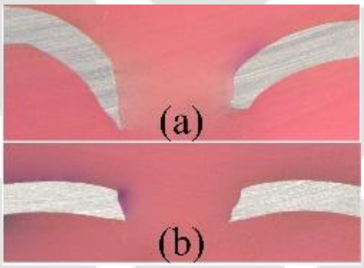

***Figure 4.7*** *Cross section of perforated holes, (a) Pointed punch, (b) Concave punch*

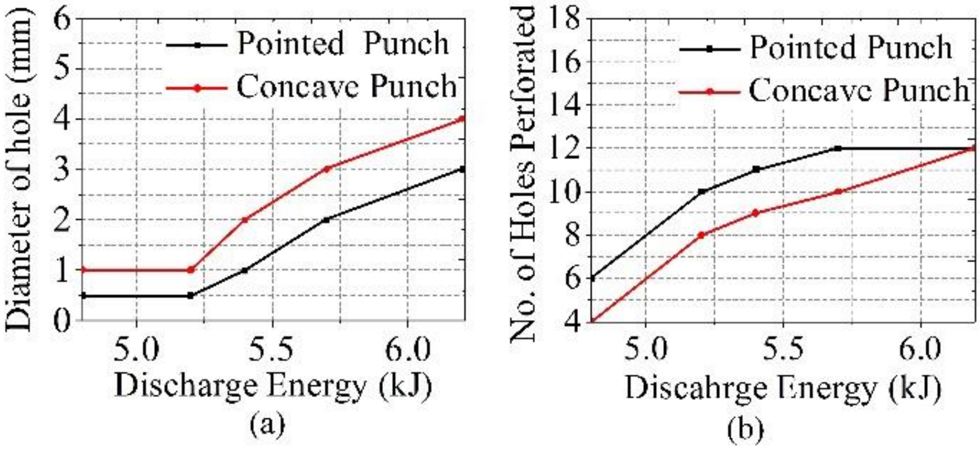

***Figure 4.8*** *(a) Variation of number of holes and (b) Diameter of perforated holes with discharge energy for 12 pointed and concave punch arrangements*

Variation of a number of holes and diameter of perforated holes with discharge energy for 12 pointed and concave punch arrangements is shown in figure 4.8 (a) and figure 4.8 (b). The number of holes perforated in case of pointed punches were more than the concave punch, because of the less sheared area which results in easy piercing, wherein concave punch arrangement, complete removal of sheared slug took place which consumes more energy as compared to the pointed punch. In comparison with a pointed punch, concave punch shows better results as the diameter of the perforated holes were more, and the complete removal of slug took place.

To study the effect of a number of punches on perforation 36 punches were used and the results were observed. Tubes perforated by 36-pointed punch are shown in figure 4.9.

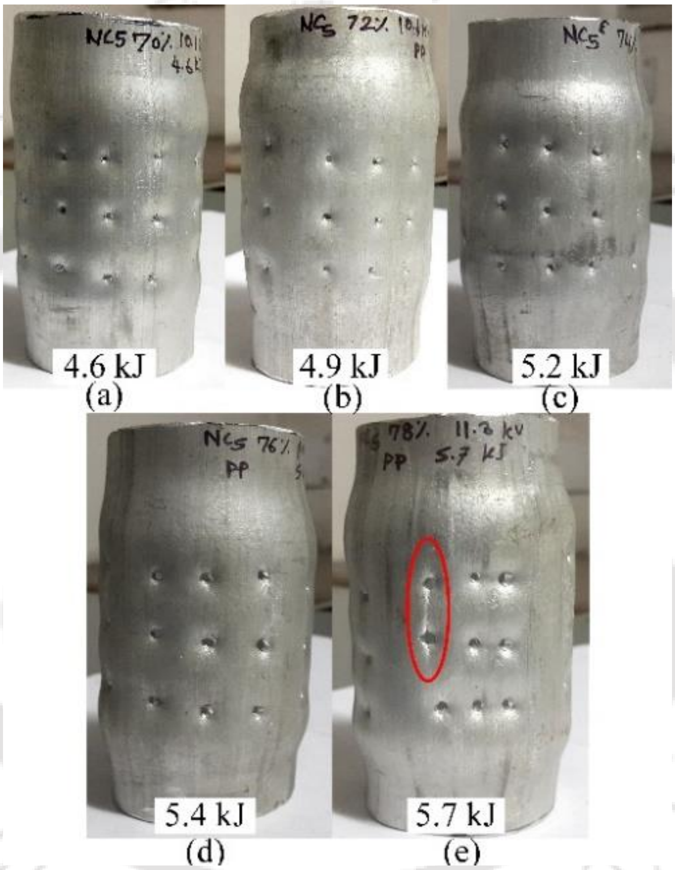

***Figure 4.9*** *Tubes after the experiment for 36-pointed punch arrangement*

At lower discharge energies piercing was not possible. All 36-hole got pierced at 5.4 kJ of discharge energy, but average hole diameter was 1 mm. Further, increase in energy increases the average diameter of the hole to 2 mm but at the same energy, propagation of a crack from one hole to the other was observed as highlighted in figure 4.9 (e). In another case 36 concave punches placed on the periphery of the die. Same 10 turn coil was used for the perforation. Tubes after the experiment are shown in figure 4.10. The number of holes perforated and hole diameter increased with increase in discharge energies. No cracks were observed at higher discharge energies. The average diameter of the hole was observed to be 4 mm at 6.5 kJ discharge energy.

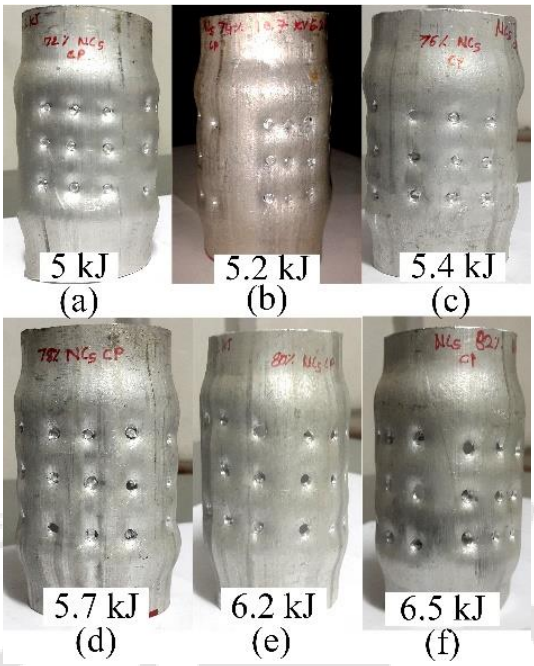

***Figure 4.10*** *Tubes after the experiment at different discharge energies for 36 concave punch arrangement*

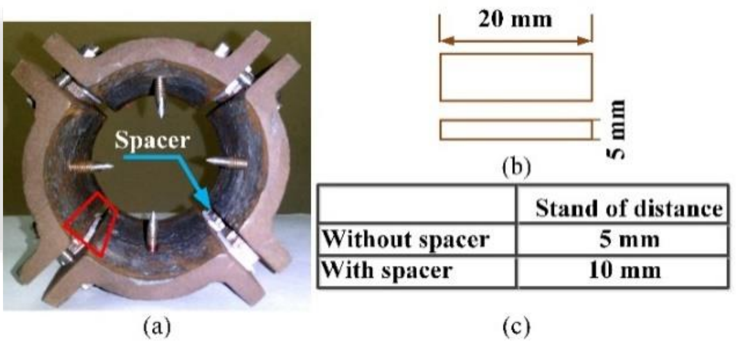

***Figure 4.11*** *(a) Spacer placed in the die, (b) Spacer geometry and (c) Stand of distance with and without a spacer*

The stand-off distance is the distance between the tube to be perforated and die. Hole diameter observed in the case of 2 mm stand-off distance was not up to the required diameter. To study the effect of a stand of distance on perforation, a 3 mm thick spacer was placed between two mating die part to increase the distance between tube and die as shown in figure 4.11. After placing the spacers, the gap between the tube and die becomes 5 mm. Instead of 12 pointed punches, 36 pointed punches were placed on the periphery of the die, and experiments were done at different discharge energies for finding out optimum discharge energy.

Tubes after the experiments are shown in figure 4.12. From the experiment, it was observed that with the increase in discharge energy diameter of tube increases. Increase in diameter was measured at a different point along the length of the tube. The maximum deformed diameter of the tube was 60 mm, which is the internal diameter of die after placing spacer. Increase in diameter of the tube with respective discharge energies is shown in figure 4.13. The number of holes perforated increases at a lower energy in case of with spacer arrangement, but after 5.2 kJ of discharge energy number of hole perforated in both the cases were same. From 5.2 kJ to 6.2 kJ discharge energy, in all the cases crack was propagated through the holes.

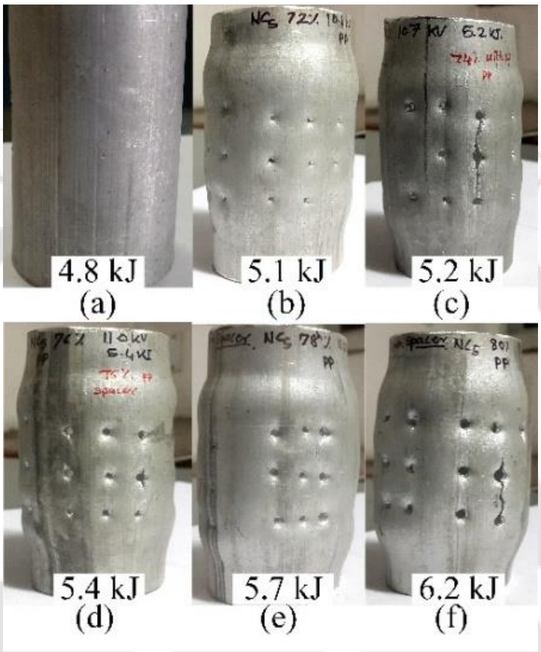

***Figure 4.12*** *Tubes after the experiment for 36-pointed punch with spacer arrangement*

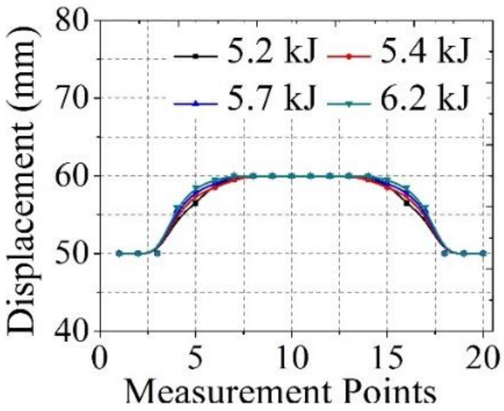

***Figure 4.13*** *Variation of forming diameter with an increase in discharge energy for 36-pointed punch with spacer arrangement*

In another set of experiment, 36 concave punches were placed on the periphery of the tube. The number of perforated holes and hole diameter for respective discharge energies increases with increase in discharge energy. Tube after the experiment is shown in figure 4.14.

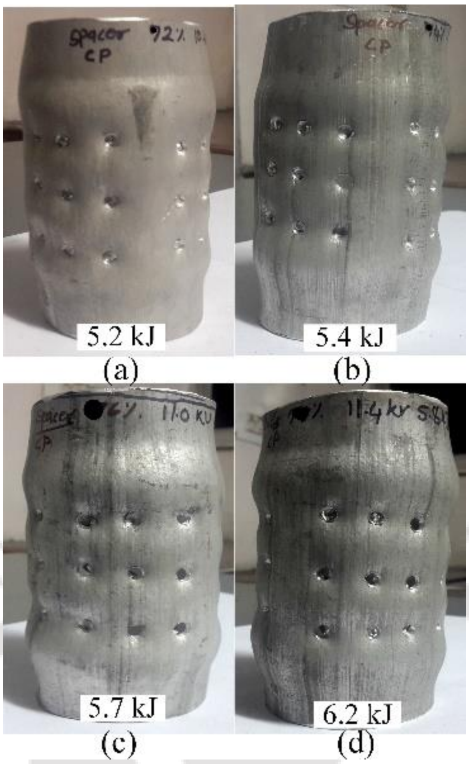

***Figure 4.14*** *Tubes after experiment for 36 concave punch with spacer arrangement*

Figure 4.15 shows the variation in a number of holes perforated and change in diameter of the hole with an increase in discharge energy for 36 pointed and concave punches with and without spacer arrangement.

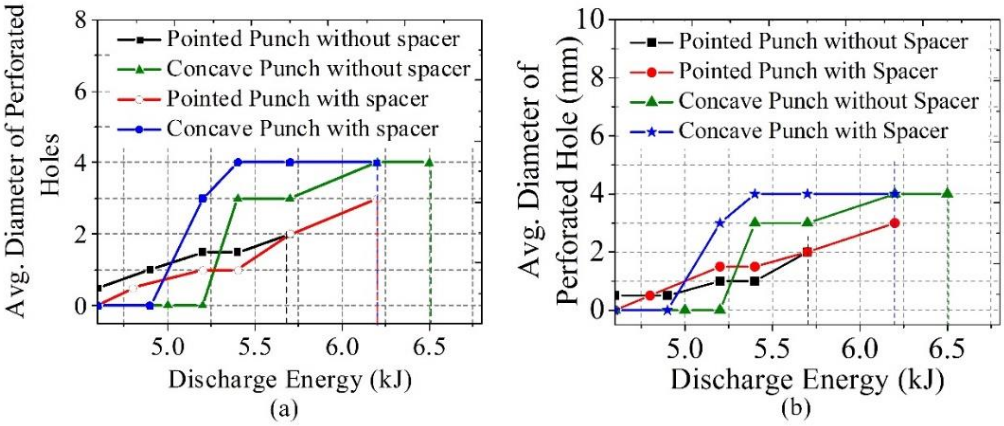

***Figure 4.15*** *(a) Variation of number of holes and (b) Diameter of perforated holes with discharge energy for 36 pointed and concave punch arrangements*

In case of pointed punch with and without spacer arrangement, the number of holes perforated was increased with increase in discharge energy. Increase in diameter of perforated holes was observed in case of with spacer arrangement. In case of concave punch with a spacer, a number of holes got perforated at lower energy and diameter of the perforated hole were more than the without spacer arrangement. All 36 holes got perforated at 6.2 kJ discharge energy while for same discharge energy 16 number of holes got perforated without spacer arrangement. By considering the diameter of perforated hole obtained and complete removal of slug during perforation, concave punch with spacer arrangement is the perfect combination.

### 4.2.1 Micro Hardness Tests and SEM Examination

Microhardness measurements were performed to study the effect of hardening or softening phenomena around the hole. Hardness values were measured along the four lines around the hole, and on each line, five measurements were taken using Vickers microhardness testing machine with 100 g load. Test data was recorded for different discharge energies. Figure 4.16 (b) to figure 4.16 (d) shows the measurements of hardness values along the four lines around the hole for different discharge energies.

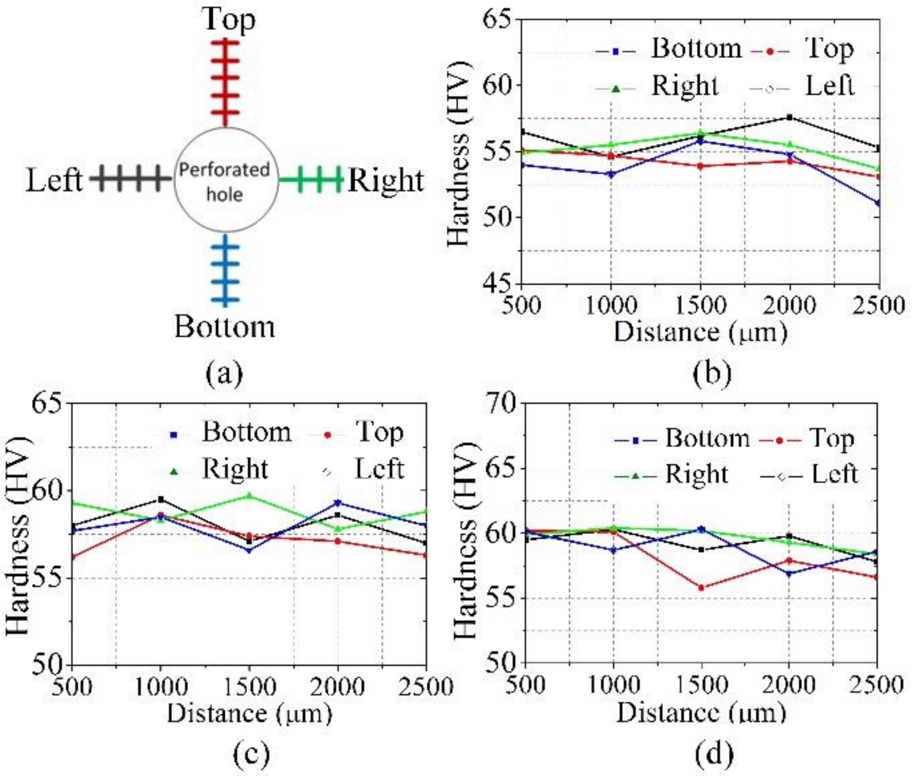

***Figure 4.16*** *(a) Hardness value measurement lines and average hardness values at (b) 5.8 kJ discharge energy (c) 6.2 kJ discharge energy (d) 6.6 kJ discharge energy*

An average value of hardness in the four directions for each of the sample after perforation was calculated and plotted against the distance from hole boundary and compared with hardness values after heat treatment of tube as shown in figure 4.17. An average hardness value after heat treatment and before the experiment is 43.5 HV. Hardness values obtained increases with the discharge energy; this is because the current and magnetic field intensity increased with increase in discharge energy which leads to greater magnetic pressure on the tube. Compressive residual stress can be introduced along the surface to get peening effect by electromagnetic field [49, 50], this induced increases the hardness.

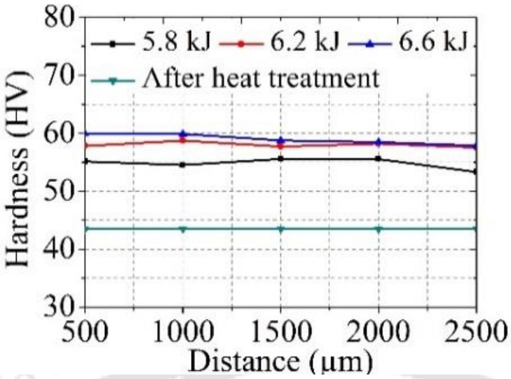

***Figure 4.17*** *Hardness values obtained for EM perforated hole at 5.8 kJ, 6.2 kJ, and 6.6 kJ discharge energy*

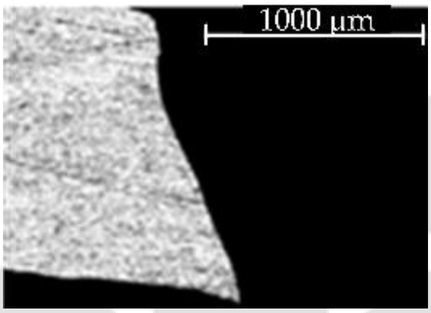

***Figure 4.18*** *Optical microscope image of cutting edge of the slug*

Figure 4.18 shows the microscope image of cutting edge of a hole which was obtained after perforation by a concave punch at 5.4 kJ discharge energy. Cutting edge shows that no burrs were formed. It concludes that the EMFP is a high strain rate forming process which eliminates the burrs and burrs free perforation is possible. In the case of electromagnetic forming and perforation, the impact of punch on the tube is at very high velocity. During the perforation by a concave punch, removal of the sheared slug is observed.

A scanning electron microscopy (SEM) study was performed on holes, perforated by concave punches. The figure 4.19 (a)-(e) shows the SEM images of the crack zone. The crack observed at the perforated hole, and magnified image of crack is shown in figure 4.19 (a) and (b) respectively. The failure occurred at high discharge energy. Figure 4.19 (c), (d), and (e) shows the SEM images of the cracked zone at higher magnification. A large number of spherical dimples separated by thin walls were observed which indicates the failure of material by ductile dimple fracture. Dimples are the void segments which come together to produce the fracture path [52]. Dimples formed on the shear lip of the cup and cone fracture will be elongated and attain parabolic shape as shown in figure 4.19 (e), which is an indication of shear failure.

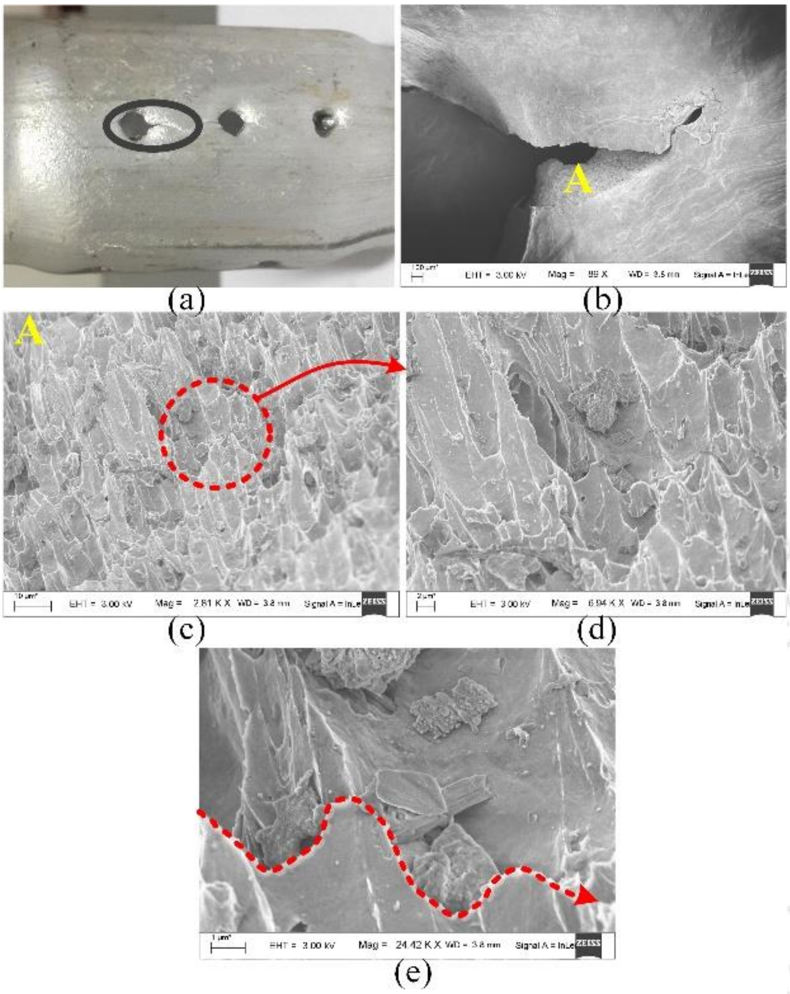

***Figure 4.19*** *(a)-(e) SEM investigation of the crack zone*

### 4.3 Conclusion

The experimental work presented in this study shows the feasibility of the EMFP process. Because of the annealing, workability of the Al tubes increases which leads to better perforation. A number of holes pierced, the diameter of hole and tube increases with an increase in discharge energy in all the cases.

- In case of 12-hole perforation without spacer arrangement, concave punches showed better results as compared to pointed punches as the perforated hole diameter obtained in case of concave punch was close to a required diameter as well as the complete removal of slug is taking place.
- In 36 pointed punches with spacer case, from 5.2 kJ to 6.2 kJ discharge energy, cracks were propagated through the holes because of excessive energy while in concave punch case more energy is utilized in the removal of the slug. In concaved

punch with spacer arrangement, a number of holes got perforated, and the diameter of the hole was more than with-out spacer arrangement. As a result, concave punch with spacer arrangement is a good combination for perforating holes in the tube.

- Microhardness test study has pointed out the strain hardening in the tube. The reason for this increase in hardness is due to residual strain induced by high-speed forming process and this is an advantage over the conventional forming process.
- Ductile dimple fracture was observed in SEM sur-vey. SEM study indicates the shear failure of the tube.

## Chapter 5

# Comparison of Electromagnetic and with Quasi-Static Die-Less Perforation[II]

### 5.1 Introduction

In the electromagnetic forming and perforation process, the electromagnetic force is used for the forming and perforation of tubes. It is a high strain rate shearing process, and it overcomes various disadvantages of conventional or quasi-static processes, like large roll-over depth, the formation of burrs etc. In the previous chapter the feasibility of EM forming and perforation process is established. Many researchers have studied electromagnetic manufacturing processes and their advantages over other conventional processes. Experiments on the punch-less electromagnetic shearing process were conducted by the Golowin et al. [52]. Authors validated the finite element simulated results with experiments. The detail investigation shows that the electromagnetic perforation of tubes has not been studied, and there is a need to understand the standing of electromagnetic forming and perforation with respect to Quasistatic dieless perforation. In chapter 4 we have experimentally studied electromagnetic forming and perforation of Al tubes with both pointed and concave punches. We have observed that the holes produced by concave punches with spacer arrangement have the most desired outcome. In this chapter, the detailed comparison of electromagnetic die-less perforation with quasi-static die-less perforation has been carried out. For the comparison purpose, Scanning Electron Microscopy (SEM) investigation of a cross section of holes and cracks generated due to impact has been carried out. Detailed study of sheared edge characteristics is done with the help of an optical microscope. Microhardness test has been carried out to study the effect of hardening or softening phenomenon near the hole.

### 5.2 Materials and Methods

#### 5.2.1 Materials

Experiments have been carried out on heat treated as-received Aluminum tube having an outer diameter of 50 mm, the thickness of 1.5 mm and a length of 100 mm for EM as well as the Quasi-static perforation. The geometry of punches and punch after manufacturing are shown in figure 3.4. The Vickers microhardness test is conducted for finding out the hardness value of as received Al alloy, and it is found to be 105 HV. Al 6061 T6 tubes are

---

[II] *Pawar, S., Kore, S. D., & Nandy, A. (2020). Comparison of sheared edge zones developed in electromagnetic and quasistatic dieless perforation. Journal of Materials Engineering and Performance, 29(2), 1146-1155.*

heat treated by annealing to improve its workability. The heat treatment process is already discussed in section 4.1.

### 5.2.2 Experiments on EM and Quasi-Static Die-less Perforation of Al Tubes

The experiments of electromagnetic perforation of tubes are carried out in chapter 4 section 4.2. The results which are obtained in previous chapter are used in this chapter for the comparison study. The conventional perforation at the quasi-static loading rate (10mm/min) is carried out with a separate experimental setup built using a Universal Tensile Machine (UTM). The setup used and the schematic representation is discussed in chapter 3, section 3.2.4. The same pointed punch and concave punch used in electromagnetic perforation are used for this study. The tube dimensions and material are kept same.

## 5.3 Results and Discussion

### 5.3.1 Comparison of EM Perforation with Quasi-Static Die-less Perforation

*a. Punch exit Hole Study*

In the case of EM perforation, experiments are carried out on as heat-treated Al tube with the help of pointed and concave punches. After many experimental trials with above-mentioned tube geometry and material, it is observed that at 6.2 kJ discharge energy, better perforation is possible. The same coil, having 10 turns, 16 mm$^2$ wire, 100 mm length and coil external diameter of 46 mm, is used for both types of punches.

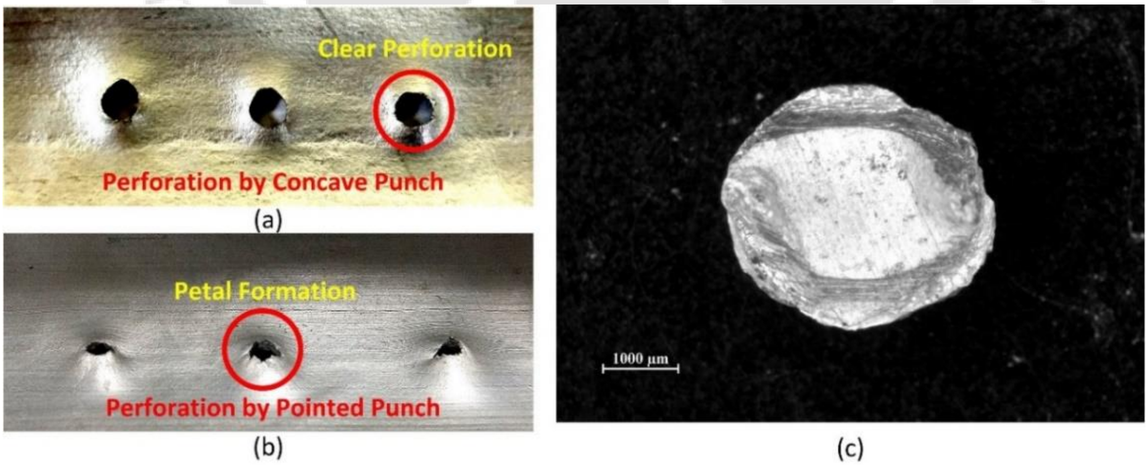

***Figure 5.1*** *(a, b) Samples after EM die-less perforation process for, (a) Concave punch, (b) Pointed punch, and (c) Slug obtained after EM concave punch perforation*

Figure 5.1 shows the samples after the EM die-less perforation. In Quasi-static die-less perforation, experiments are carried out on same as-received heat-treated Al tube. The failure load data is obtained from the UTM readings. It has been found that failure load increases with increasing number of punches. It can be observed that failure load also depends upon the geometry of punches.

Piercing is easier with pointed punches as compared to other geometries due to the sheared area. The samples after the quasi-static die less perforation is shown in figure 5.2. During the pointed punch perforation in both EM as well as quasi-static type, the alloy in front of the punch is pushed in an inward direction. The punch also drags adjacent material with it. Hence, there will be a radial inward flow of the materials along the edge of the material hole which results in the petalling phenomenon as shown in figure 5.3.

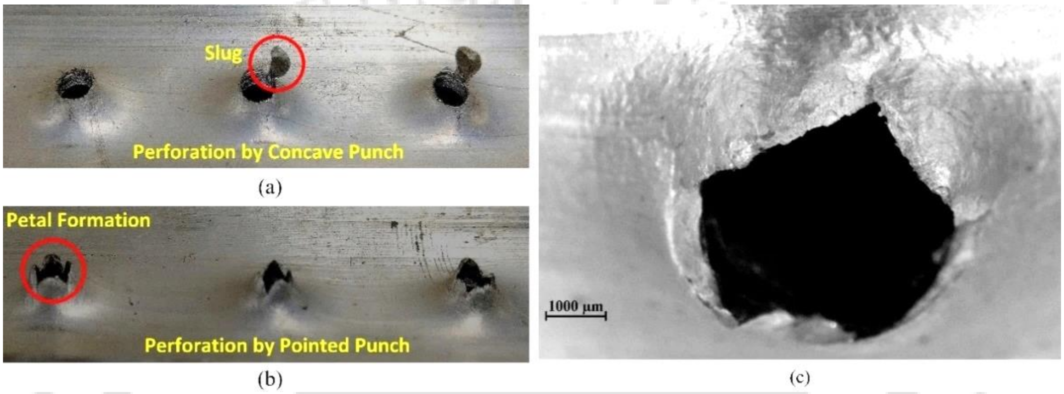

***Figure 5.2*** *Samples after the Quasi-static perforation for, (a) Concave punch, (b) Pointed punch, and (c) Petals at higher magnification in case of pointed punch*

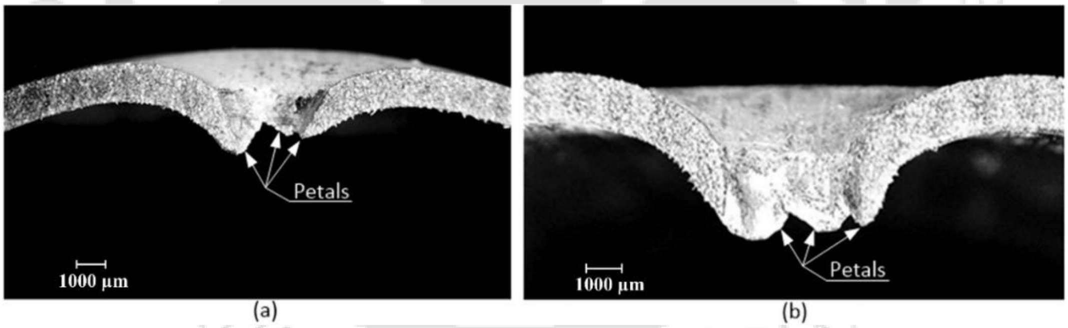

***Figure 5.3*** *Cross section of perforated holes by the pointed punch, (a) EM perforation process and (b) Quasi-static die-less perforation process*

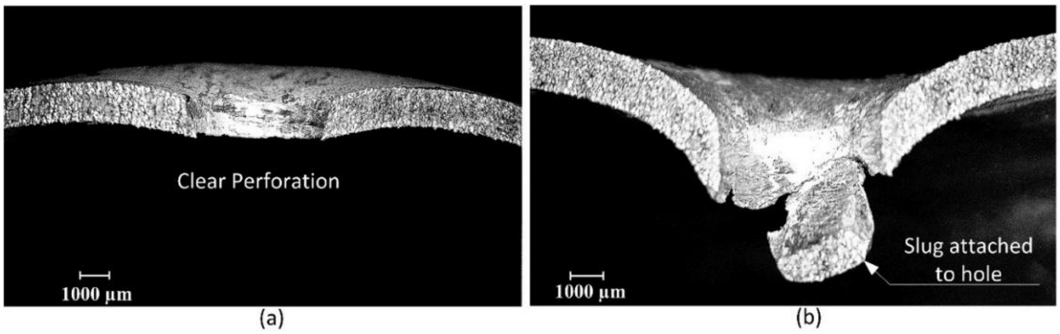

***Figure 5.4*** *Cross section of perforated holes by the concave punch, (a) EM perforation process and (b) Quasi-static die-less perforation process*

In the case of EM perforation for the concave punch, ejection of the slug is observed, and clear perforation is possible. Figure 5.4 (a) shows the cross section of the hole after EM perforation. In comparison with EM perforation, in Quasi-static concave punch perforation, direct ejection of the slug is not observed as shown in figure 5.4 (b) because of the die-less process. Figure 5.5 shows the punch exit hole side after quasi-static die less perforation for both pointed and concave punch.

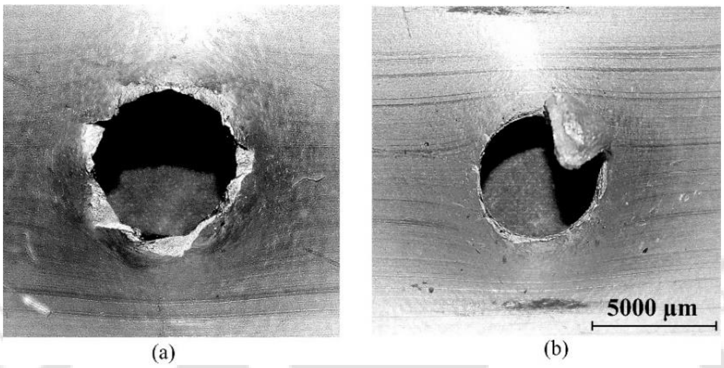

***Figure 5.5** Punch exit hole side for quasi-static perforation: (a) Pointed punch and, (b) Concave punch*

*b. Effect of loading on Roll over depth, Burr depth, and Work Hardening*

Figure 5.6 shows the different zones of the sheared edge, where *T* is the thickness of the tube. During the shearing process, initially the punch engages the tube, and it pushes the material downward. Hence, it draws the material and creates a small depression on the sheet as shown in figure 5.6, which is termed as 'Roll-over.' With the increase of the clearance value in die punching, roll-over area also increases [53].

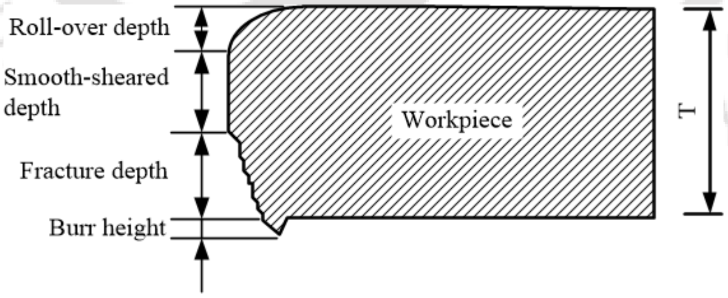

***Figure 5.6** Different zones of sheared edge*

After the initial stage, punch continues to penetrate, and it shears the upper part of the material creating a burnished area before the remaining material along thickness is fractured or separated completely. Burr is a sharp protrusion at the bottom edge of the perforated hole, formed at the end of the shearing process due to elongation of the slug material before completely getting separated from the parent material. Figure 5.7 shows different zones of the sheared edge, for EM and Quasi-static die-less processes.

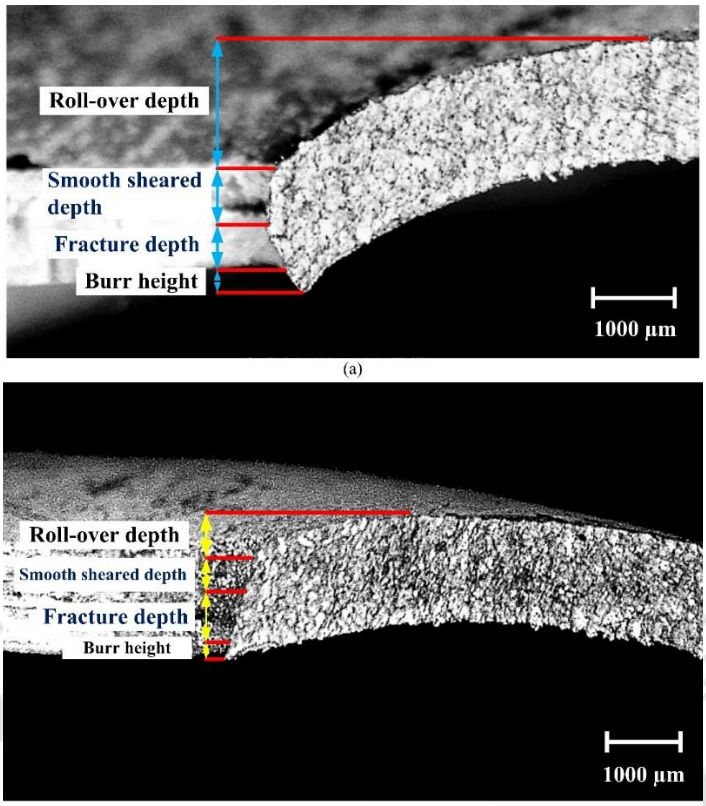

(a)

(b)

***Figure 5.7*** *Sheared edge zones for, (a) EM perforations and (b) Quasi-static die less*

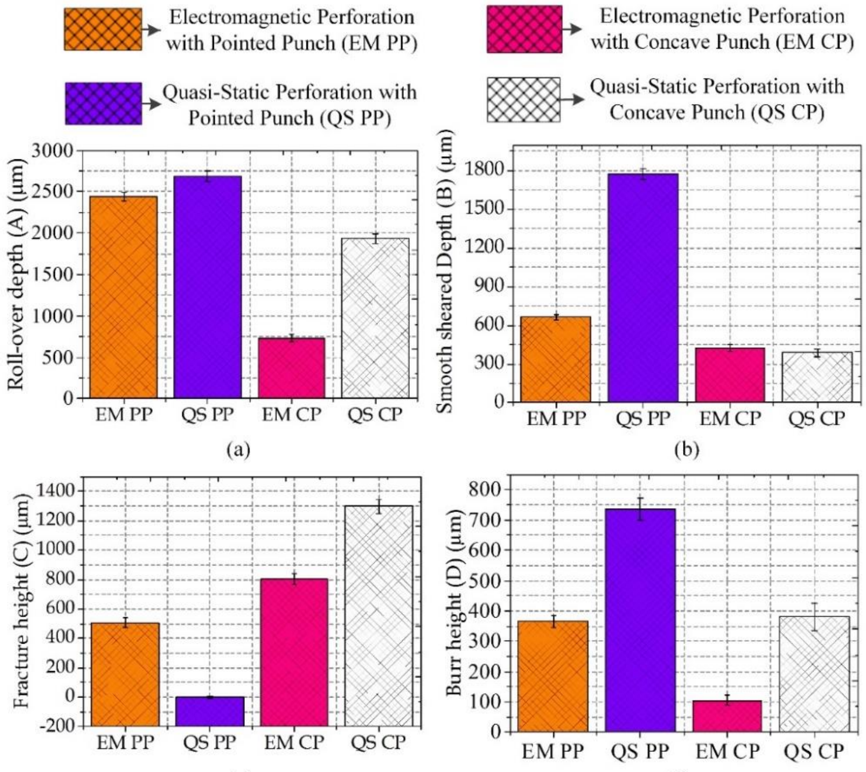

(a)

(b)

(c)

(d)

***Figure 5.8*** *Effect of the process and punch type on roll-over depth (A), Smooth sheared depth (B), Fracture height (C) and Burr height (D) Values for concave punch (Cp) and pointed punch (Pp)*

After the experiment the roll over depth, smooth sheared depth and burr height are measured with the help of a microscope. The effect of process type and punch type on all above-mentioned height and depths is shown in figure 5.8. As shown in figure 5.9, in both cases absence of die support results in a considerable roll over depth but it is much less in case of EM perforation due to high-speed impact. For the same reason, EM perforation has less burr height than the quasi-static perforation.

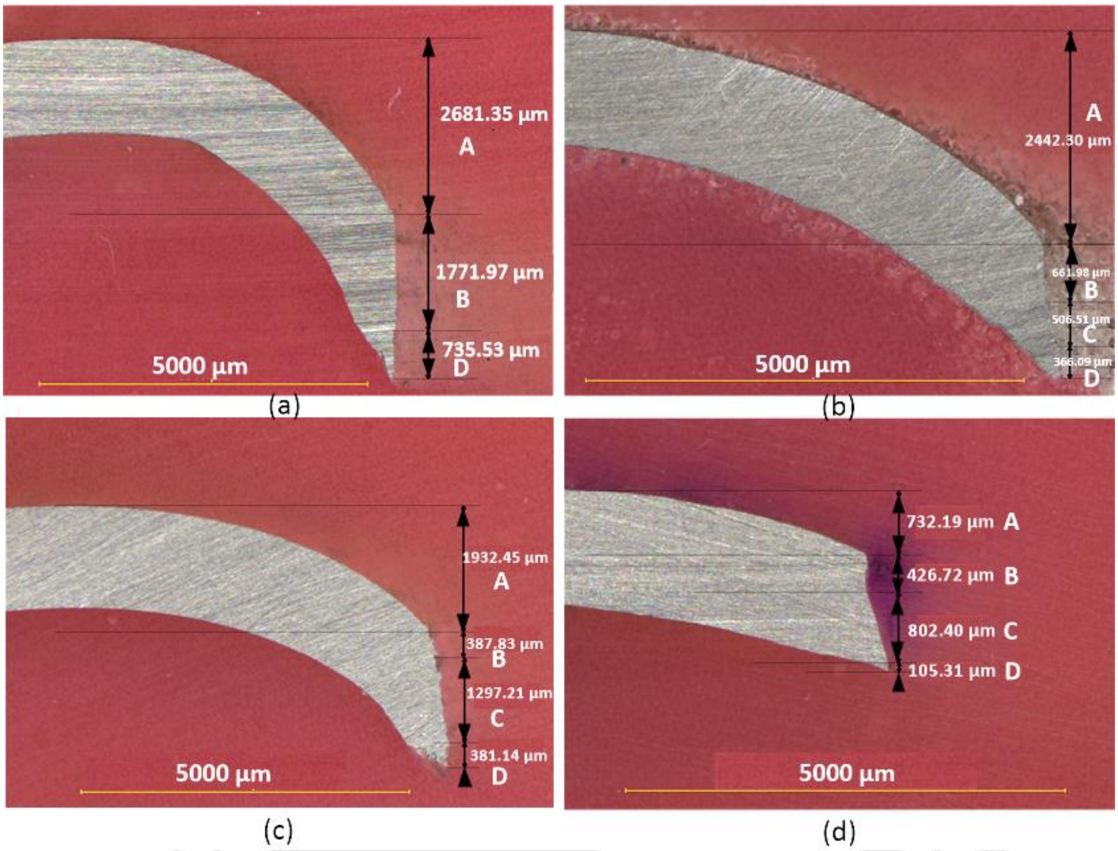

***Figure 5.9*** *Quantitative measurements of sheared edge: (a) Quasi-static pointed punch, (b) EM pointed punch, (c) Quasi-static concave punch, and (d) EM concave punch*

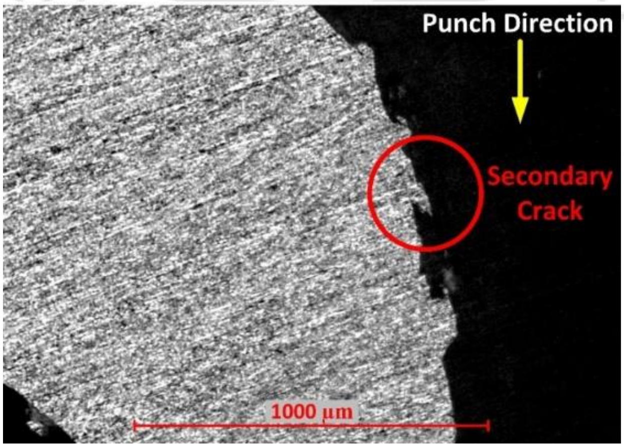

***Figure 5.10*** *Secondary crack formation during Quasi-static die-less perforation with a concave punch*

From the magnified images of sheared edge (figure 5.10 and 5.11), secondary cracks and hence rough surface finish can be clearly observed in quasi-static perforation whereas EM perforation leads to smooth sheared edges

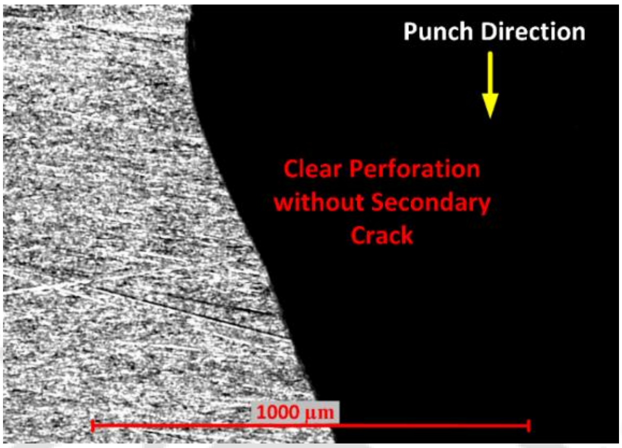

***Figure 5.11*** *Smooth sheared edge during EM die-less perforation with a concave punch*

In order to study the hardening effect near the sheared edge of the perforated hole, the Vickers Microhardness test is conducted with 100g load, at three locations along the thickness and 0.5 mm away from the edge of the perforated hole as shown in figure 5.12 (a). In the case of EM perforation average hardness value increases to 65.74 HV from that of starting annealed Al tube at 43.5 HV whereas for quasi-static perforation hardness remain unaltered as shown in figure 5.12 (b). Hence, we can conclude that more work hardening takes place during EM perforation.

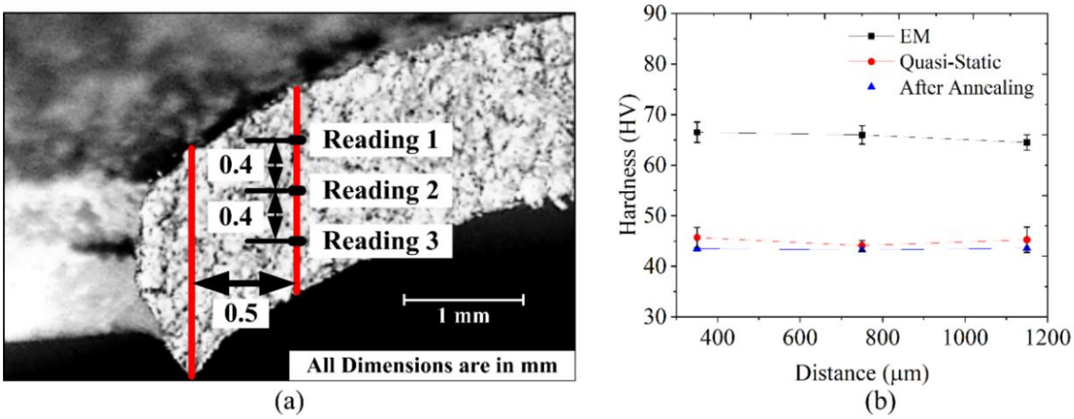

***Figure 5.12*** *Vickers Hardness test of perforated holes: (a) Measurement points, and (b) Hardness values*

### *c. Scanning Electron Microscopy (SEM) Study*

A scanning electron microscopy survey has been done to study the hole morphology, failure pattern during perforation, and modified features due to impact. Figure 5.13 shows SEM images at a different magnification of the crack zone at the exit side of the hole perforated in quasi-static perforation with a concave punch. Dimple growth is the predominant ductile failure mode for both EM and quasi-static perforation as shown in figure 5.13 and 5.14 respectively. A large number of spherical dimples are observed in figure 5.13 (b). Dimple occurs because of the formation of microvoids along the fracture path [14].

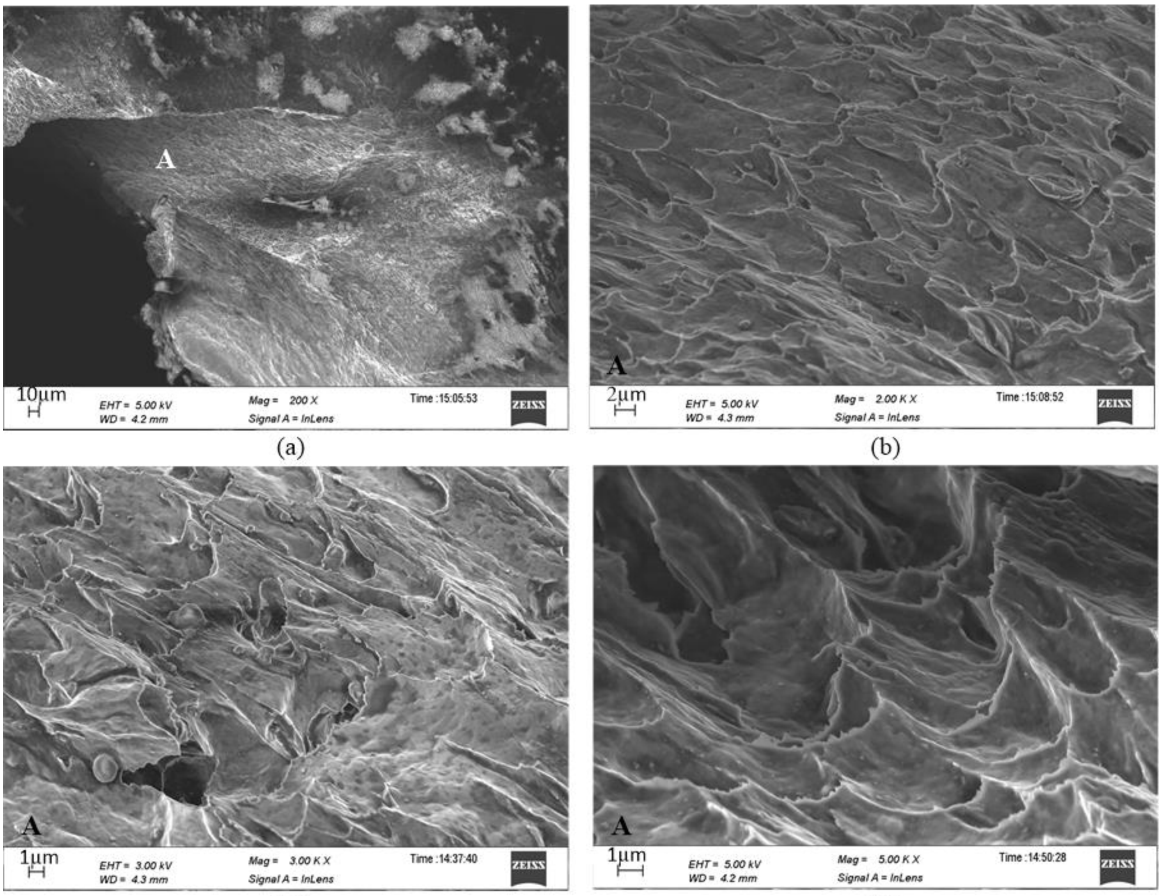

(a) (b)

(c) (d)

***Figure 5.13*** *SEM images of the exit side of the hole in quasi-static perforation with a concave punch: (a) Images taken at region A in the crack zone (b) At 2.00 KX magnification, (c) At 3.00 KX magnification and (d) Parabolic fracture profile at 5.00 KX magnification*

Elongated dimples with parabolic shapes are an indication of shear failure. In quasi-static perforation such elongated dimples are observed (Figure 5.14 (b)) due to low strain rate loading and combined tension and bending state [54], while in EM perforation as this high strain rate process takes place within a microsecond, dimple boundaries are short as shown in figure 5.14 (a). Thus, in both, EM as well as quasi-static perforation, mode of failure is ductile. In brittle fracture, spontaneous and rapid crack propagation occurs through perforated holes, which is not desirable. Hence, the ductile fracture is always preferred over the brittle fracture.

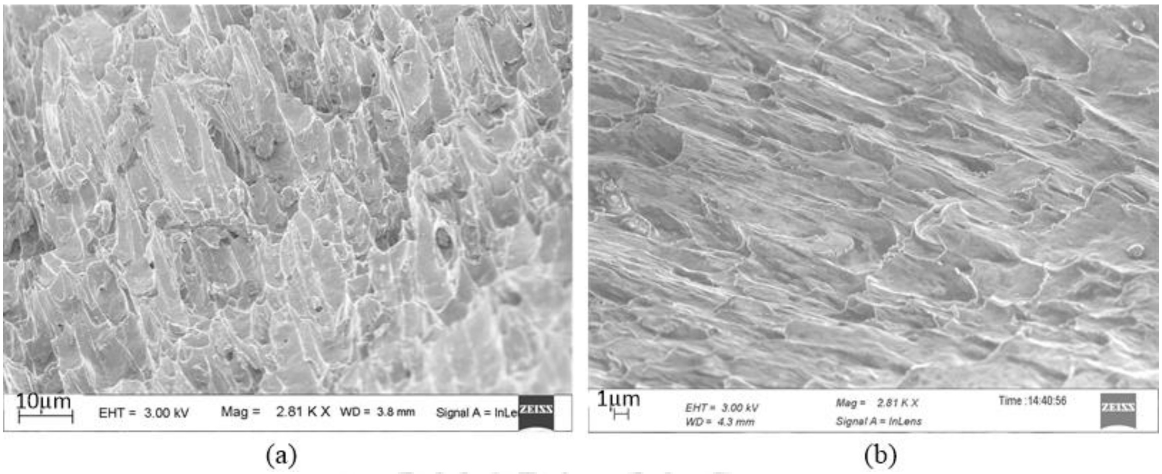

(a) (b)

***Figure 5.14*** *2.81 KX magnified images of dimple formation in (a) EM perforation, (b) Quasi-static die-less perforation*

## 5.4 Conclusions

The performed comparison between EM and quasi-static die-less perforation shows that the EM perforation process overcomes various disadvantages of the quasi-static perforation process. Based on the observations, the following conclusions are drawn,

1. In both the perforation process pointed punch penetrates the workpiece by pushing the material in front of the punch aside which causes the petalling mode of failure. In case of concave punch, EM perforation separates the slug completely by plugging where as in quasi-static perforation, the slug is not separated due to low loading rate.

2. The roll-over depth and burr height are more in case of quasi-static perforation as compared to those in EM perforation. Hence, we can have a smooth shear edge with lower surface roughness in EM perforation.

3. Secondary cracks produced due to secondary shearing in case of quasi-static die-less perforation can distort the surface finish of the hole edge. Such secondary cracks are absent in EM perforation due to high strain rate shearing which overcomes the disadvantage of quasi-static perforation.

4. In the quasi-static process, hardness remains almost unaltered after perforation, whereas in EM perforation there is a nearly 50% increase in hardness, which indicates a hardening of material in EM perforation. Microhardness study reveals the strain hardening of material due to EM pressure wave resulting in higher strength compared to the original material.

5. SEM study shows that in both EM and quasi-static perforation mode of failure is ductile. In quasi-static perforation, low loading rate results in elongated dimples whereas in EM perforation short dimple boundaries are observed due to high loading rate.

Overall, in this novel comparison of EM perforation with quasi-static die less perforation, the holes produced by the EM perforation process with a concave punch are secondary crack free unlike the quasi-static perforation. Also, the edge characteristics show that these holes have a far better surface finish than the conventionally perforated hole. Further, the optimization of parameters will establish EM perforation as traditional practice.

# Chapter 6

# EM Forming and Perforation of Tubes: Modeling, Simulation and Validation[III]

## 6.1 Introduction

Electromagnetic forming and perforation (EMFP) is a complex Multiphysics process involving structural deformation due to electromagnetic forces. The complexity further increases in EMFP due to two simultaneous deformation processes, namely, forming and shearing (perforation) [56]. The deformed perforated tube has many applications especially in automobile, oil and gas industries. The main advantage of EMFP is its productivity; also, it will overcome the limitations of conventional forming processes such as less formability. Addition to that, the high-speed shearing process can reduce the formation of burr. Although the physics of the process is well documented in the literature, still the development of new accurate simulation models is a challenge to the research community. In chapter 4 the feasibility of the EMFP process is established. In chapter 5, the detail comparison between electromagnetic perforation and quasi-static dieless perforation is presented and the advantages of high strain rate perforation over quasi-static perforation are identified. To understand the failure mechanism and movement involve at high strain rate perforation process, in this chapter, FEA analysis of electromagnetic forming and perforation process has been carried out with the help of a non-coupled and coupled simulation method separately. The comparison of these methods is carried out, and numerical results are validated with experimental results.

## 6.2 Methodology

### 6.2.1 Non-coupled Simulation

In non-coupled simulation approach, two simulation softwares, Ansys Maxwell and Ansys Explicit Dynamics are used, where the electromagnetic part is simulated by ANSYS Maxwell and structural part is solved in ANSYS Explicit Dynamics. The detail flow chart and simulation procedure is already explained in section 3.2.2. The mesh convergence study is done, and optimum mesh and time steps are used for the simulation. Tetrahedral 3D element is used for meshing tube. Al 6061 material is used for tube. The Steinberg-Guinan material is used to describe the behaviour of this material at high strain rates. The constitutive equation and parameters used are explained in chapter 3 with equation 3.7.

---

[III] *Pawar, S., Ray, D., Kore, S. D., & Nandy, A. (2020). Electromagnetic forming and perforation of tubes: Modeling, simulation and validation. Journal of Manufacturing Science and Engineering (ASME), DOI: 10.1115/1.4049090.*

### 6.2.2 Coupled Simulation

Coupled electromagnetic and mechanical simulation is carried out in LS-DYNA. The detailed flow chart of coupled behaviour and simulation procedure is explained in section. Because of the limitation of coupled simulation software, only quad type of elements is used for meshing all parts [10]. Time step and mesh convergence study is carried out and optimum mesh size and time steps are used for all the simulations. Al 6061-T6 material is used for the tube, Cu is used for the coil and SS-304 is used for the punch. Fracture prediction within the numerical models can be handled by the failure models. Here, the Johnson-cook failure model is used where, the equivalent strain is the function of strain rate, stress, temperature and damage constants. The constitutive equation of the failure model is given in equation 2.20.

## 6.3 Results and Discussions

### 6.3.1 Electromagnetic Forming and Perforation (EMFP) Experiments

Experiments are carried out on Al tubes with the pointed and concave punch. The discharge energies are varied from 5.0 kJ to 6.2 kJ. At lower discharge energy, i.e. at 5.0 kJ, punch indented the tube, further increase of energy initiates the perforation process and at 6.2 kJ discharge energy tube gets perorated with the required diameter of the hole. In case of pointed punch perforation, petaling phenomenon is observed where the clear perforation is not possible, while in case of concave punch, clear perforation is observed with separation of slug from the hole. The diameter obtained after perforation by a concave punch is more compared to the pointed punch. The cross-sections of perforated holes after the experiment are shown in figure 6.1.

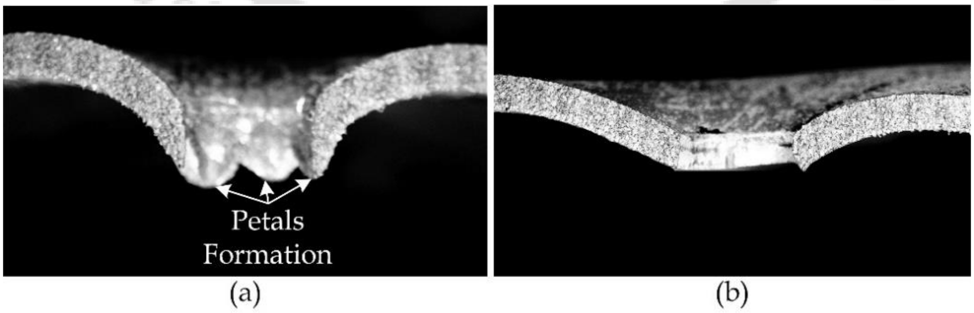

***Figure 6.1*** *Cross-sections of perforated holes by (a) Pointed and (b) Concave punch*

## 6.4 Validation and Comparison

### 6.4.1 Magnetic Pressure and Radial Displacement

Figure 6.2 shows the variation of the magnetic field and pressure with time for coupled and non-coupled simulations. It is observed that the magnetic field obtained in non-coupled simulation is more than the coupled simulations. Because of the generation of more magnetic field, the magnetic pressure obtained in the non-coupled simulation is more as compared to the coupled simulation.

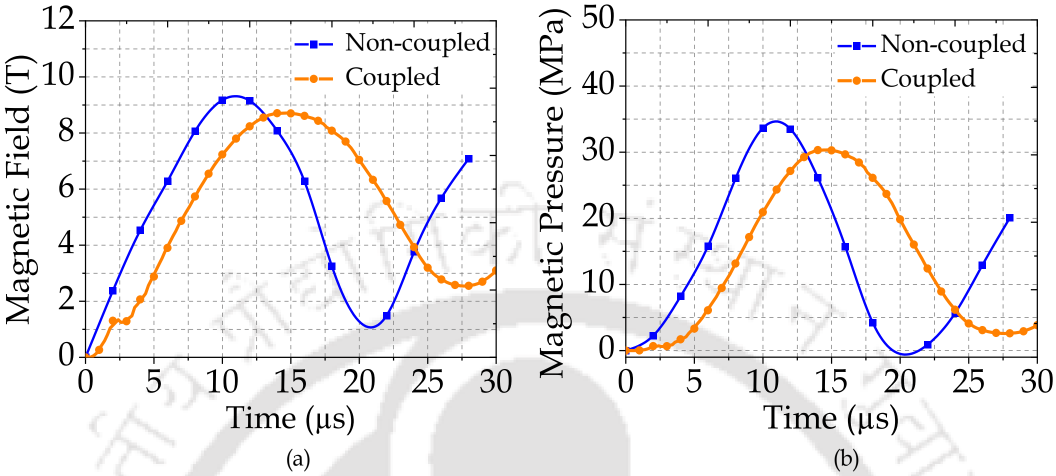

***Figure 6.2*** *Variation of (a) Magnetic field, and (b) Magnetic pressure with time*

The pressure generated in the coupled solver, due to magnetic fields is evaluated by equation 6.1 [3]. The loss in the magnetic field is considered in the coupled simulation. This loss is due to the structural deformation, which causes diffusion of magnetic flux line on the surface of the tube.

$$P(r,t) = \int_{r_0}^{r_i} F\,(r,t) = \frac{1}{2}\mu(H_{gap}^2(t) - H_{diffuse}^2(t)) \tag{6.1}$$

However, non-coupled solver ignores the loss due to diffused magnetic lines of flux, and it calculates the magnetic field on the inner surface of the tube. Thus, the transient magnetic pressure obtained in the non-coupled solver is more compared to the coupled solver. The transient magnetic pressure generated in the non-coupled model can be evaluated by the analytical equation 6.2.

$$P(r,t) = \frac{1}{2}\mu H_{gap}^2 \tag{6.2}$$

As a consequence of more magnetic pressure generation, the non-coupled solver overestimates the results, but the deviation with experimental deformation is minimal, on the other hand, coupled solver accurately estimates the deformation. Figure 6.3 shows the variation of displacement along the length obtained in the experiment, coupled and in the non-coupled simulations for both pointed and concave punch perforation.

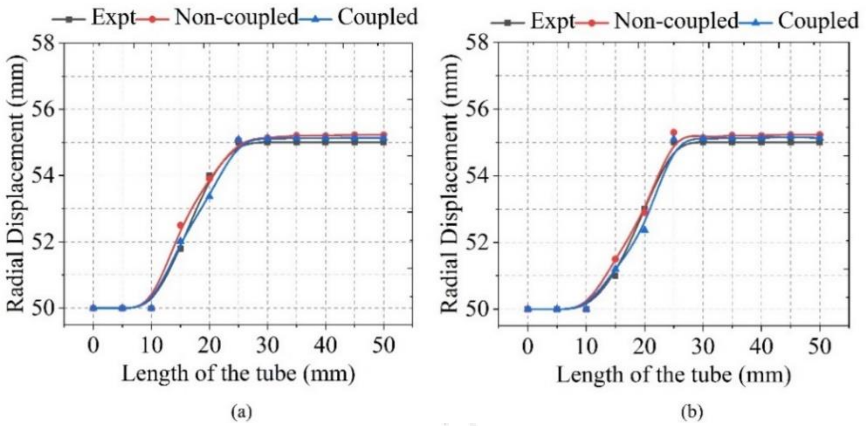

(a) (b)

***Figure 6.3*** *Variation of displacement along the length (measured from symmetry Z face i.e. punch location to the end of the tube) (a) Pointed punch and (b) Concave punch*

### 6.4.2 Material Movement and Process Parameter Distribution

Deformation and perforation snapshots are captured at different time points in both coupled and non-coupled simulation for pointed and concave punch perforation. The cross-sections of the holes after perforated by pointed punch in coupled and non-coupled simulations are presented in figure 6.4, 6.5 and 6.6. These plots clearly show that both simulation models qualitatively capture the behaviour of the tube during perforation at different discharge energies.

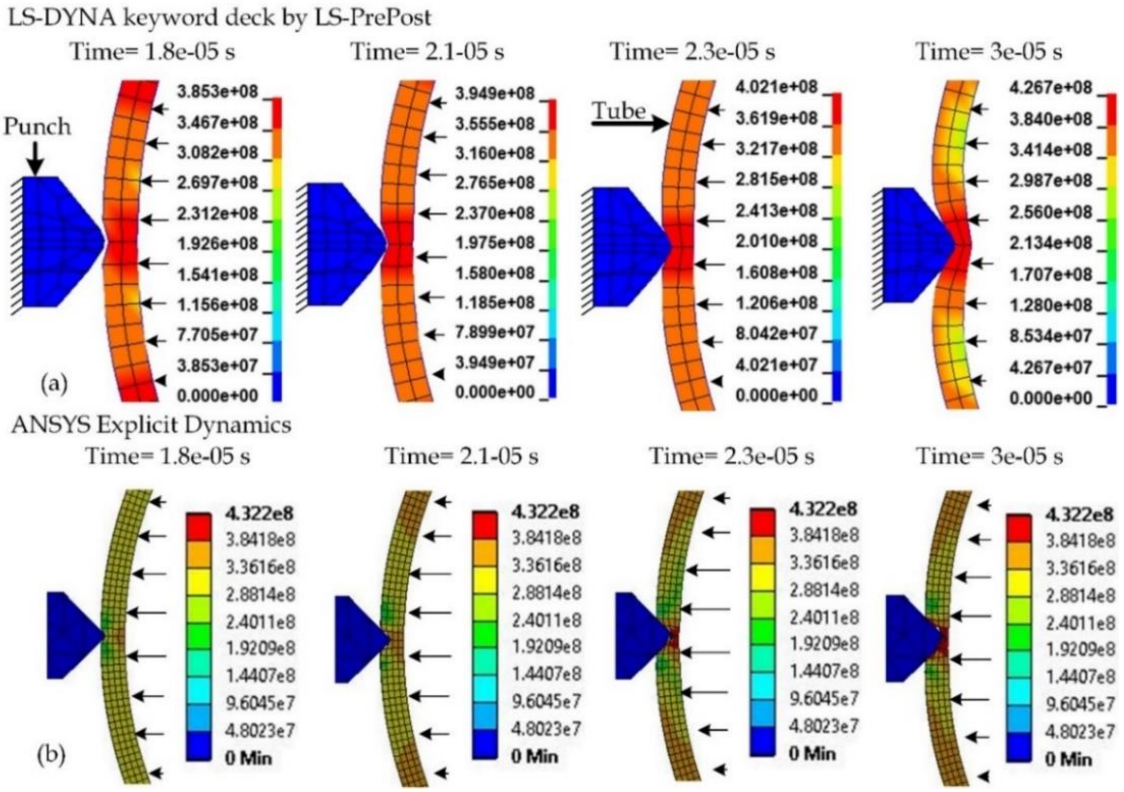

***Figure 6.4*** *Perforation stages of tubes at different time instances at 5.0 kJ discharge energy for pointed punch in (a) Coupled and (b) Non-coupled simulations with von-Mises stress distribution (in Pa)*

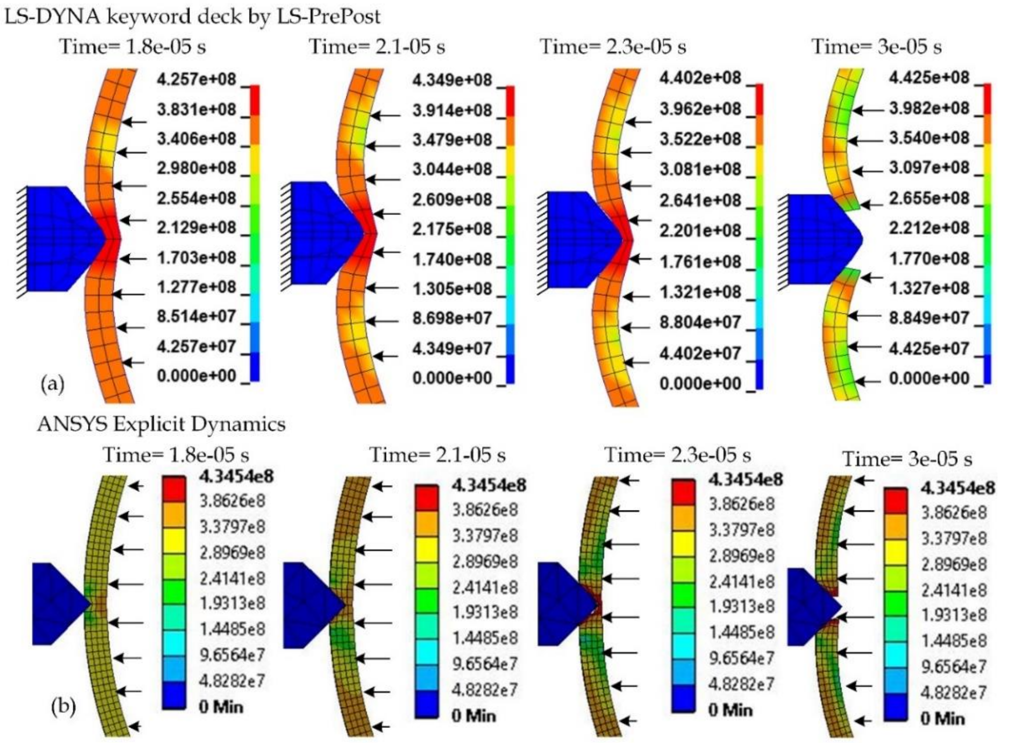

***Figure 6.5*** *Perforation stages of tubes at different time instances at 5.7 kJ discharge energy for pointed punch in (a) Coupled and (b) Non-coupled simulations with von-Mises stress distribution (in Pa)*

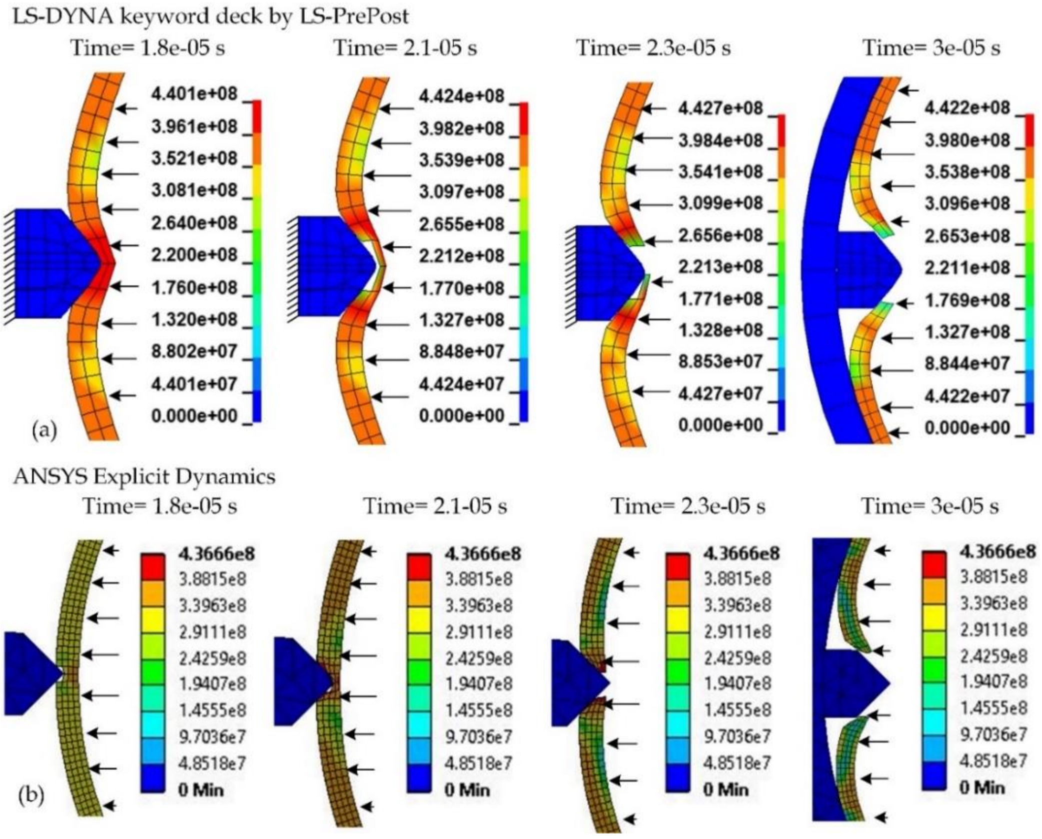

***Figure 6.6*** *Perforation stages of tubes at different time instances at 6.2 kJ discharge energy for pointed punch in (a) Coupled and (b) Non-coupled simulations with von-Mises stress distribution (in Pa)*

Figure 6.6 demonstrate that the coupled model weakly captures the initiation of penetration, whereas in the non-coupled simulation, clear initiation of penetration is observed. In all the cases maximum von-Mises stresses are observed at the interaction of punch and tube, starting from 0 to 4.42e+08 Pa in coupled simulation and up to 4.336e+08 Pa in case of non-coupled simulation. The variation of maximum von-Mises stresses obtained with different discharge energies is shown in figure 6.7. The minor difference is observed between coupled and non-coupled results.

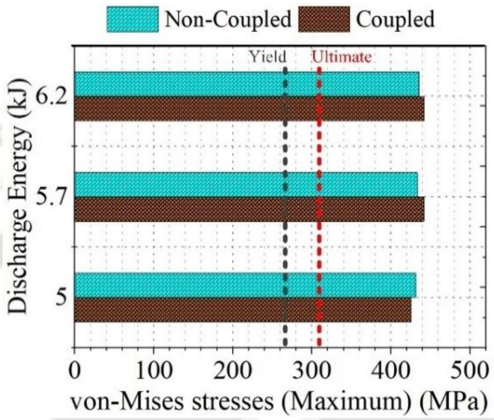

***Figure 6.7** Maximum von-Mises stress at different discharge energies for pointed punch perforation*

During the commencement of perforation by pointed punch, the alloy in front of the punch is pushed in an inward direction. The punch also drags adjacent material with it. Hence, there will be a radial inward flow of the material along the punch edge which results in maximum stress generation at the interaction region. After the initiation of penetration by 2.1e-05 seconds, the maximum stress regions migrate from interaction point to other end through the edges. By 3e-05 seconds in case of 6.2 kJ discharge energy, maximum stress layer gradually disappears since the material is removed and tube get perforated.

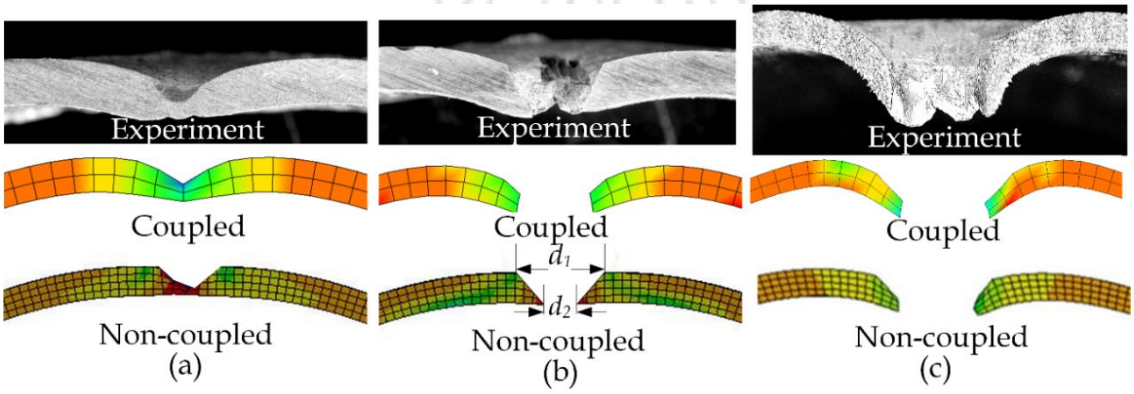

***Figure 6.8** Comparison of perforated holes at (a) 5.0 kJ, (b) 5.7 kJ and (c) 6.2 kJ*

Figure 6.8 shows the comparison of the cross-section of the perforated hole at different discharge energy in the experiment, coupled and non-coupled simulations. As shown in figure 6.8 (a), at 5.0 kJ discharge energy, holes do not get perforated due to low magnetic pressure generation in both experiments as well as in simulations. As shown in figure 6.8 (b), at 5.7 kJ, just exit of punch is observed which shows this energy is necessary for the initiation of penetration. As shown in figure 6.8 (c), in the experiments as well as in simulations, all holes are completely perforated at the discharge energy of 6.2 kJ. Hence, 6.2 kJ discharge energy is treated as minimum discharge energy. The diameter of holes measured after perforation in each case is listed in table 6.1.

***Table 6.1*** *Diameter of the perforated hole in case of pointed punch*

| Energy (kJ) | Experiment | | Coupled Simulation | | Non-Coupled Simulation | |
|---|---|---|---|---|---|---|
| | d1(mm) | d2(mm) | d1(mm) | d2(mm) | d1(mm) | d2(mm) |
| 5.0 | 1.5 | - | 1.6 | - | 1.63 | - |
| 5.7 | 4 | 2.8 | 4.2 | 2.92 | 4.5 | 3 |
| 6.2 | 5 | 5 | 5.2 | 5.1 | 5.6 | 5.2 |

In all the cases presented in figure 6.8, the variation between the diameter obtained between experiment and simulation is very less. However, the diameter obtained in non-coupled simulations is more than the coupled simulation because of more magnetic pressure effect. In the same way, for perforation with concave punch the material movement is visualized by coupled and non-coupled simulation methods at various instances of time. The cross-sections of the holes after perforated by the concave punch in coupled and non-coupled simulations are presented in figure 6.9, 6.10 and 6.11.

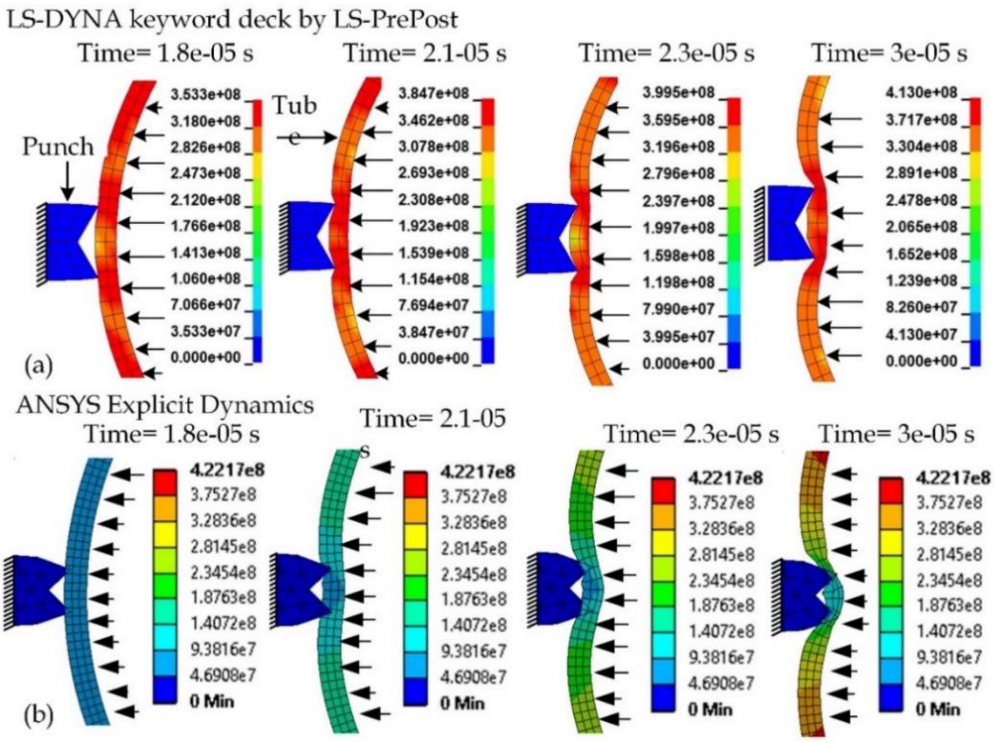

*__Figure 6.9__ Perforation stages of tubes at different time instances at 5.0 kJ discharge energy for concave punch in (a) Coupled and (b) Non-coupled simulations with von-Mises stress distribution (in Pa)*

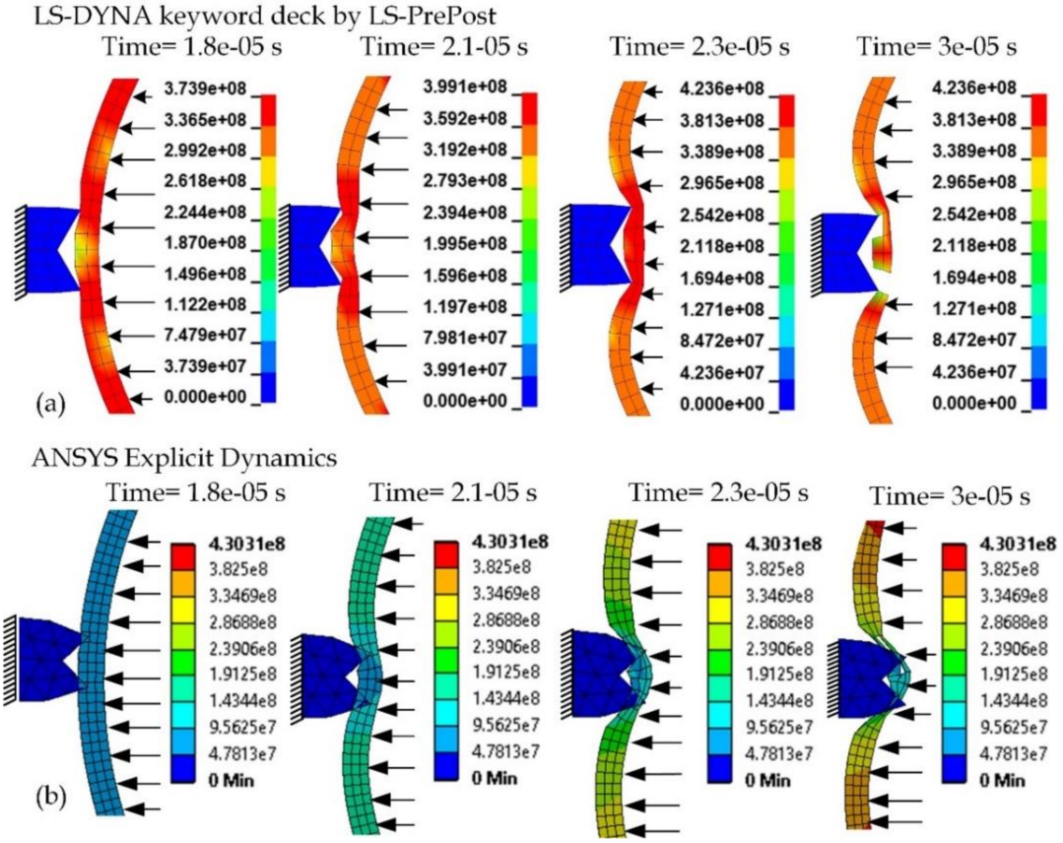

*__Figure 6.10__ Perforation stages of tubes at different time instances at 5.7 kJ discharge energy for concave punch in (a) Coupled and (b) Non-coupled simulations with von-Mises stress distribution (in Pa)*

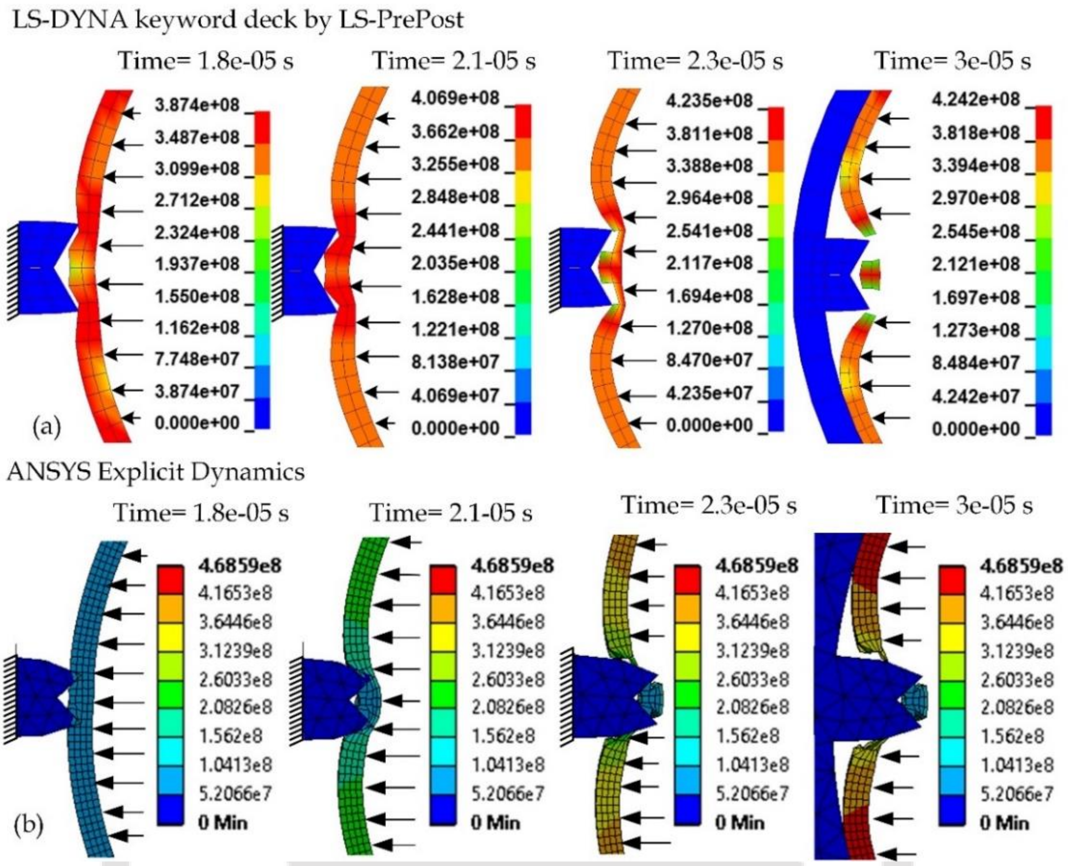

*Figure 6.11 Perforation stages of tubes at different time instances at 6.2 kJ discharge energy for concave punch in (a) Coupled and (b) Non-coupled simulations with von-Mises stress distribution (in Pa)*

In all the cases maximum observed von-Mises stresses in the perforation region for the entire simulation time period obtained at different discharge energies are shown in figure 6.12. The generated von-Mises stresses are greater than yield stress (275 MPa) and ultimate strength (310 MPa) of the material [58, 59].

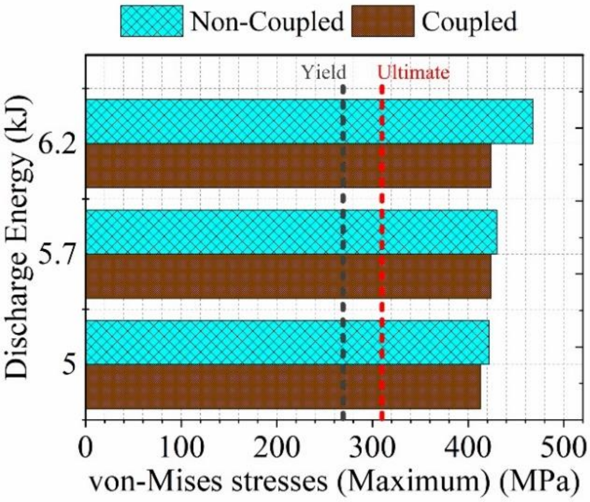

*Figure 6.12 Maximum von-Mises stress at different discharge energies for concave punch perforation*

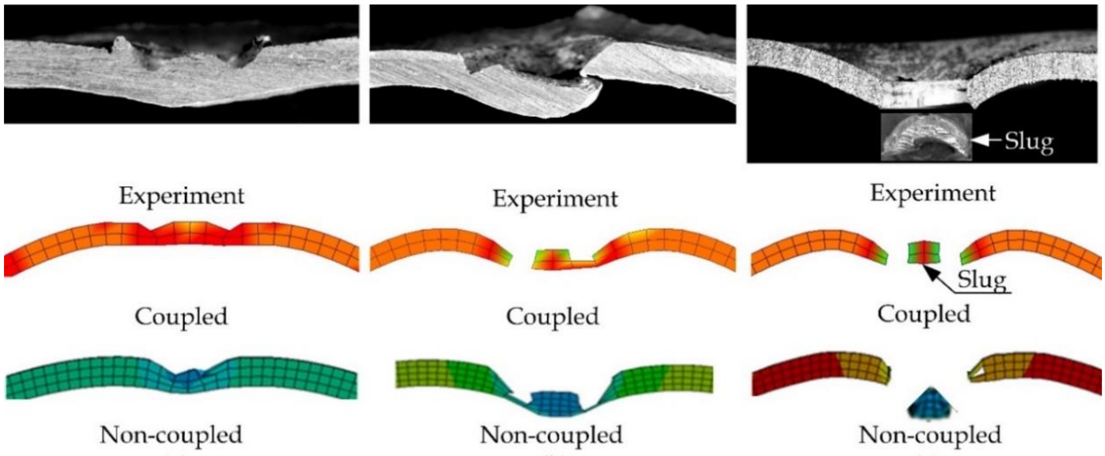

(a) (b) (c)

***Figure 6.13** Comparison of perforated holes by concave punch at (a) 5.0 kJ, (b) 5.7 kJ and (c) 6.2 kJ*

Figure 6.13 shows the comparison of a cross-section of holes perforated by concave punch in experimental, coupled and in the non-coupled simulation models for different discharge energies. At lower discharge energies, for 5.0 and 5.7 kJ, perforation is not possible during the experiment and the same is observed in both simulations. As shown in figure 6.13 (c), at 6.2 kJ discharge energy in all three cases, the slug is separated from the hole. The minimum deviation is observed between experimentally measured diameter and simulation results as shown in figure 6.14.

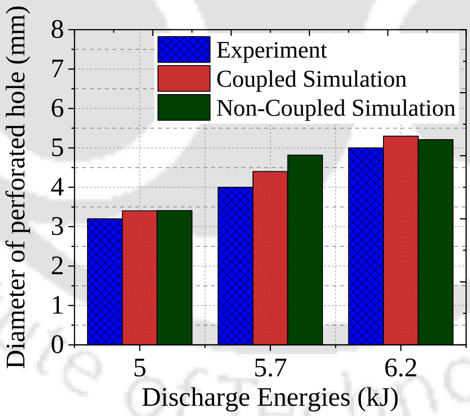

***Figure 6.14** Diameter of the perforated holes in case of concave punch*

As electromagnetic perforation takes place within microseconds, so it is challenging to find out some parameter experimentally. The magnetic field, radial displacement, the cross-section of the hole and effective plastic strain are obtained numerically and compared for coupled and non-coupled simulations. For this numerical analysis, 6.2 kJ discharge energy is used. For the comparison of variation of parameters, an element located near to the perforated hole is selected as shown in figure 6.15 and variation of different parameters is plotted as shown in figure 6.16.

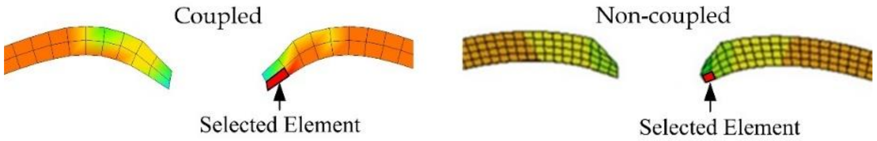

***Figure 6.15*** *Element selection to obtained variation of different parameters*

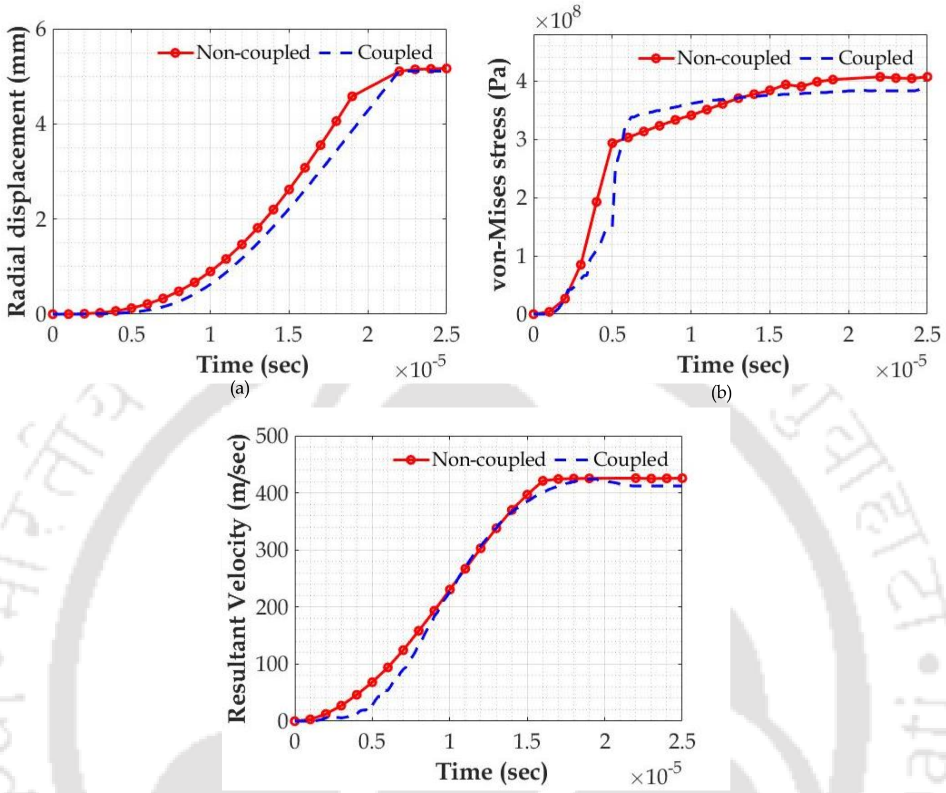

(a)

(b)

(c)

***Figure 6.16*** *Variation of (a) Radial displacement, (b) von-Mises stress, and (c) Resultant velocity*

Final displacement observed in both the simulation methods is very close to the experimental result. figure 6.16 (a) shows the change of radial displacement with time. The maximum deformation in both the simulations is found to be more than the experimental value. The actual deformation obtained in experiment is 5 mm in the radial direction while in the case of coupled simulation is 5.11 mm and in the case of non-coupled simulation is 5.17 mm. The variation is mainly because of the losses happening in actual experiments are not considered during the simulation which generates more pressure and hence, it results in more deformation. figure 6.16 (b) shows the variation of von-Mises stresses obtained in both the simulation methods for pointed punch. In both the simulations, maximum von-Mises stress is observed at the punch-tube interaction area. The maximum of 4.422e+08 Pa and 4.36e+08 Pa von-Mises stresses are generated in LS-DYNA and Ansys respectively and they are found well above the ultimate strength of the material which causes the material to shear. Figure 6.16 (c) shows the comparison of velocity obtained in

LS-DYNA and Ansys simulations. The minimum velocity required for the tube to perforate as per the required dimension is 407 m/s in case of coupled simulation and 417 m/s in case of non-coupled simulation.

The electromagnetic forming and perforation happen within micro-seconds. It is very difficult to measure the strain at different time steps experimentally. So, in the present study experimentally strain rate was not measured. Here the strain rate values are measured numerically. For that strain values varying with the time are captured in the coupled simulation as shown in figure 6.17.

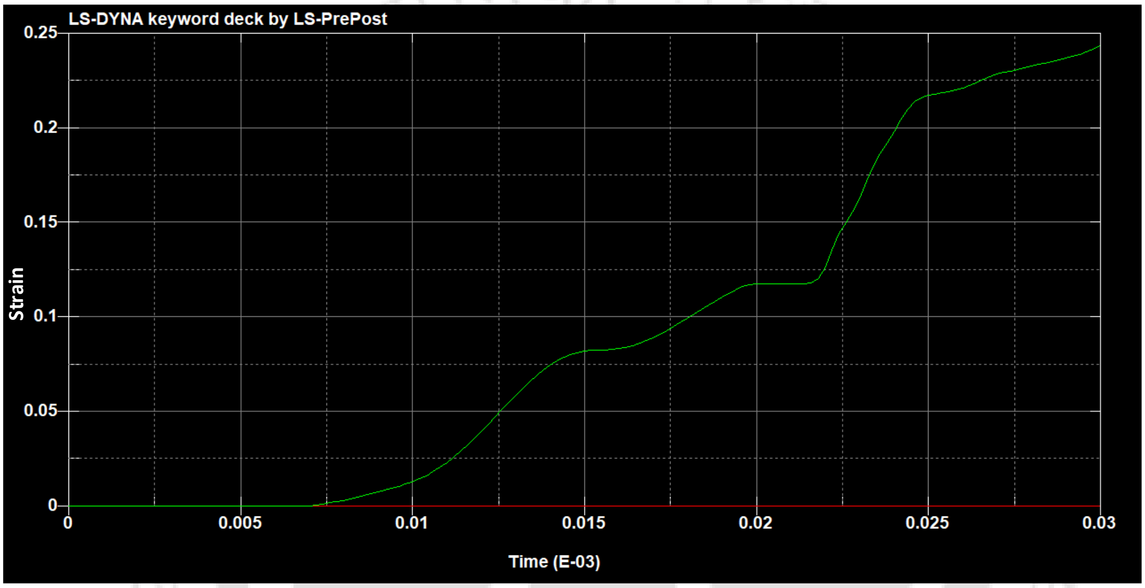

***Figure 6.17*** *Variation of strain with time*

For any small interval of time, we can measure the strain-rate as simply the amount of strain accumulated, ϵ, in a complete time interval. Here, the maximum strain observed is 0.2437 at 30 μS of the total time which us very small.

$$\text{Strain rate} = (0.2437 / (30 \text{ X } 10^{-6})) = 8.123 \text{ x } 10^{3} \text{ sec}^{-1}$$

So the strain rate observed in the simulation is in the range of $10^3$ sec$^{-1}$.

Figure 6.18 shows the Lorentz force distribution at different discharge energies. It is seen that in case of concave punch, a 161 N force was required for clear perforation at 6.2 kJ discharge energy. In case of pointed punch, because of less shear area, for initiation of perforation a minimum of 80 N force is required at 5.7 kJ discharge energy which increases up to 110 N at 6.2 kJ discharge energy for perforating tube without failure. The variation of maximum Lorentz force obtained at different discharge energies in case of pointed and concave punch is shown in figure 6.19.

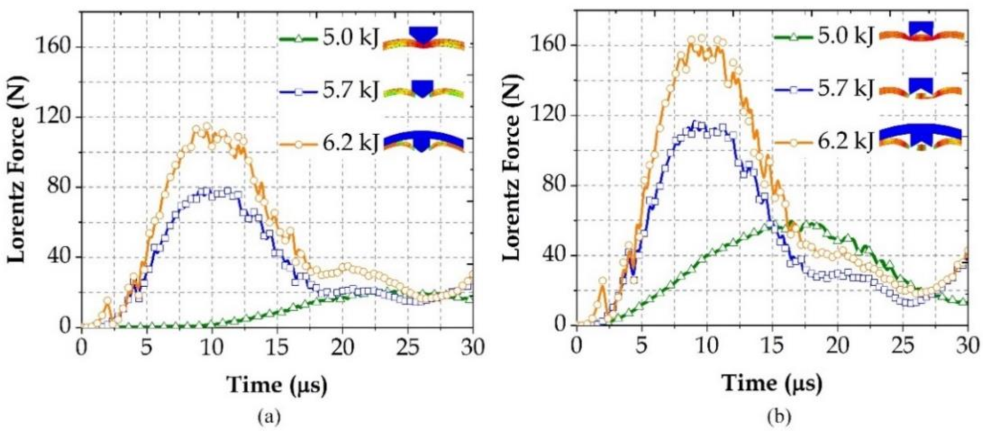

(a) (b)

***Figure 6.18*** *Variation of Lorentz force with time at different discharge energies for (a) Pointed and (b) Concave punch perforation*

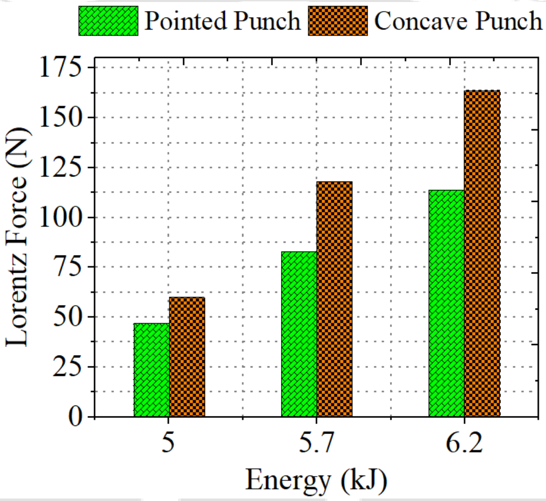

***Figure 6.19*** *Maximum Lorentz force obtained at different discharge energy in coupled*

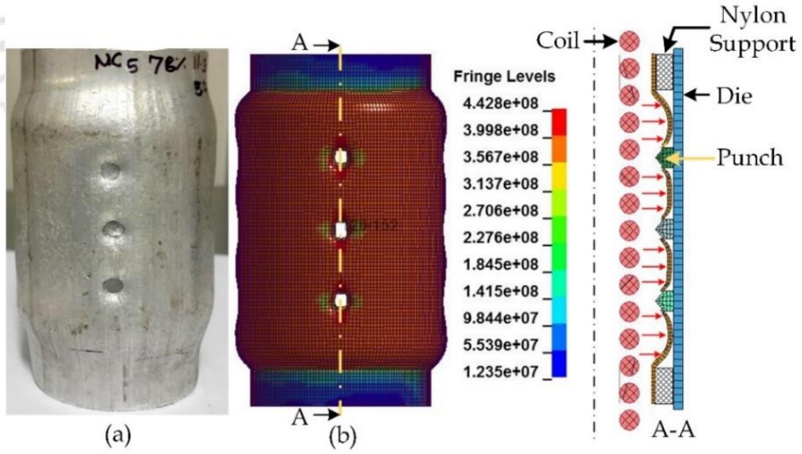

(a) (b)

***Figure 6.20*** *Tubes after perforation (a) Experiment and (b) Coupled simulations at 6.2 kJ discharge energy with pointed punch*

Figure 6.20 shows a comparison of the tube after the experiment and simulation at 6.2 kJ discharge energy with pointed punch. In these simulations and experiments, 12 pointed punches are used. All holes are perforated and the appearance in the simulation is similar to the experimental results. In earlier section validation of the four-punch forming and perforation model is done and it shows a good agreement with experimental results.

### 6.5 Conclusion

The FEA model developed in this work presents the novel finite element analysis of EM perforation processes, as no literature is available on coupled FEA simulation of tube forming and perforation.

- After the EMFP experiments, petal formation is observed in pointed punch perforation and slug separation is observed in case of concave punch perforation. The presented FEA models are succeeded in developing these failure patterns which can be useful for further EM shearing operation research. Around 95% and almost 94% of agreements are observed between numerical and experimental results for pointed and concave punch arrangements.
- The maximum von-Mises stresses of 4.42e+08 and 4.242e+08 Pa are observed for pointed and concave punch respectively in coupled simulation. Whereas in non-coupled simulation maximum of 4.336e+08 and 4.68e+08 Pa von-Mises stresses are observed for pointed and concave punch respectively. The observed stresses are well above the yield and ultimate tensile strength of the material which can easily causes the shearing of the material.
- In this work, material movement is visualized by coupled and non-coupled simulation methods at the locations of interest with the variation of time. The coupled model numerical results are found 96% in agreement with experimental results. While on the other hand on the non-coupled simulation result shows 94% agreement with experimental results. With the use of advanced meshing and boundary conditions, the initiation of failure in the tube is better captured in non-coupled simulations.

The non-coupled approach overestimates the numerical results. The non-coupled approach can be used for the good approximation of perforation process and also some limitations of coupled approach can be overcome by the use of different mesh type and meshing methods, otherwise, for more accurate estimation of results, the coupled approach should be used.

# Chapter 7

# FEA to Study the Shearing Mechanism in Punch-less EM Perforation of Aluminium Tubes[VI]

## 7.1 Introduction

Earlier the feasibility study of electromagnetic forming of tube is carried out where punches were used. In chapter 5 the it has been seen that this high strain rate process is more advantageous than the quasi-static perforation. The finite element study presented in the chapter 6 reveals that the stress produced in the EMFP are well above the ultimate strength of the material. In the above study punches are used for the perforation. In the literature it is reported that the punch-less shearing process can eliminate the burrs and slivers from the sheared part [16-18]. The influence of crack initiation and propagation and other trimming conditions like die radius were studied by Hu et al. [19]. The experimental study of trimmed surface and numerical analysis of blank fracture is carried out. The results pointed out that the burrs can be transferred from part side to scrap side if the shearing starts from the die end instead of punch end, as it is the case with the electromagnetic shearing process. In the present chapter, a novel approach for modeling the electromagnetic perforation has been used to study the shearing mechanism involved, optimum energy and the pressure required for punch-less electromagnetic perforation. The complete finite element analysis of EM perforation is conducted in two steps. Firstly, for the calculation of transient magnetic pressure generated due to an interaction between magnetic fields present in coil and tube, for this, a coupled simulation model is developed in LS-DYNA software. The generated magnetic pressure causes the expansion of the tube, resulting in crack initiation near the die cutting edge and subsequent perforation of the tube. In the second step, to study the detailed shearing mechanism involved during the EM perforation process obtained transient pressure is used for 2D FE analysis in Abaqus/Explicit.

## 7.2 Principle of Electromagnetic Punch-less Perforation

The principle of EM perforation lays out the fundamentals behind the electromagnetic effect. The schematics of EM perforation is shown in figure 7.1 (a). The high voltage is supply to the capacitor bank. After charging, the stored energy is discharged through the coil. The resulting current running through the coil produces a magnetic field around it.

---

*[V] Pawar, S. H., Kore, S. D., & Nandy, A. (2020). FE Analysis of Effect of Variation in Coil length and Coil-tube Relative Positions on Establishment of Magnetic Fields and Distribution of Velocities in Electromagnetic Forming of Muffler Tube. Procedia Manufacturing, 47, 659-664.*

The coil is surrounded by conductive metal tube and thus, it induces the eddy currents in the tube. This induced current generates another magnetic field. These developed magnetic fields are opposite in nature; thus, the interaction produces Lorentz force. This force is responsible for the movement of tube material, which initiates a crack formation and subsequent shearing of the workpiece near the cutting edge as shown in figure 7.1 (b-c). The physics involve in this process is already discussed in chapter 1 section 1.3.

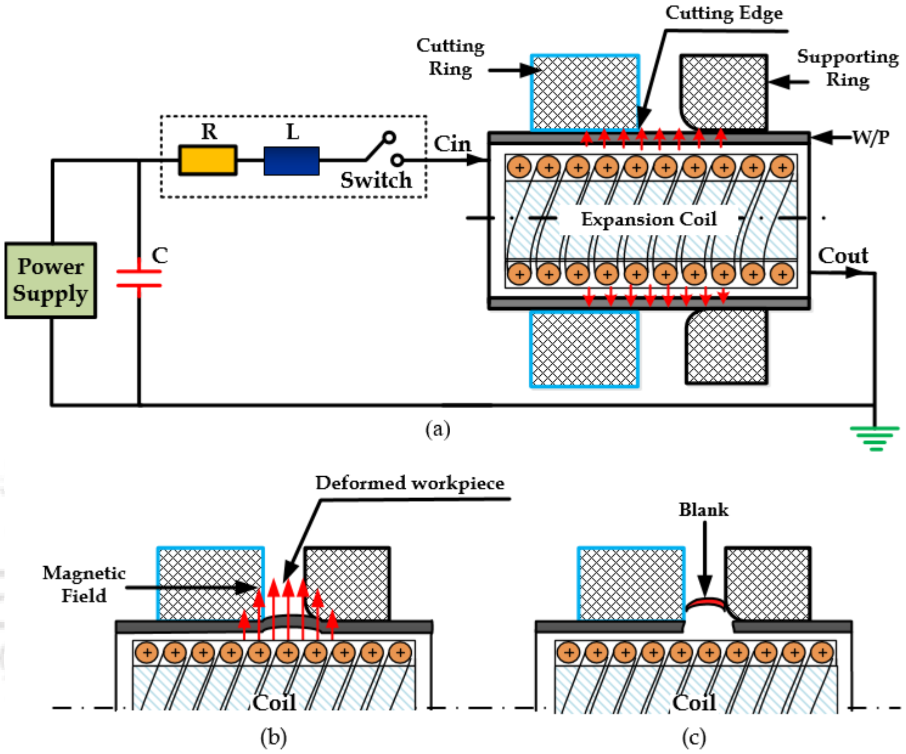

***Figure 7.1*** *(a) Process setup of EM shearing, (b) Deformation in the workpiece and (c) Shearing of the workpiece*

### 7.3 FE Analysis of Electromagnetic Punchless Perforation of Aluminium Tubes

Application of perforated tubes can be found in exhaust systems, agricultural strainers, washing machine parts, aero components, automobile components, oil filter, structural support and filter elements. Conventional perforation is difficult due to the requirement of punch and die, whereas EM perforation can be carried out with a single-sided punch. The complete FE analysis of electromagnetic perforation of aluminium tubes was done in two steps,

I. The electromagnetic simulation was conducted using the EM module of LS-DYNA to obtain transient EM pressure, which causes the tube deformation.

II. The EM pressure obtained from the step I is used in Abaqus/Explicit to understand the shearing mechanism. The flow chart of the complete simulation process is given in figure 7.2.

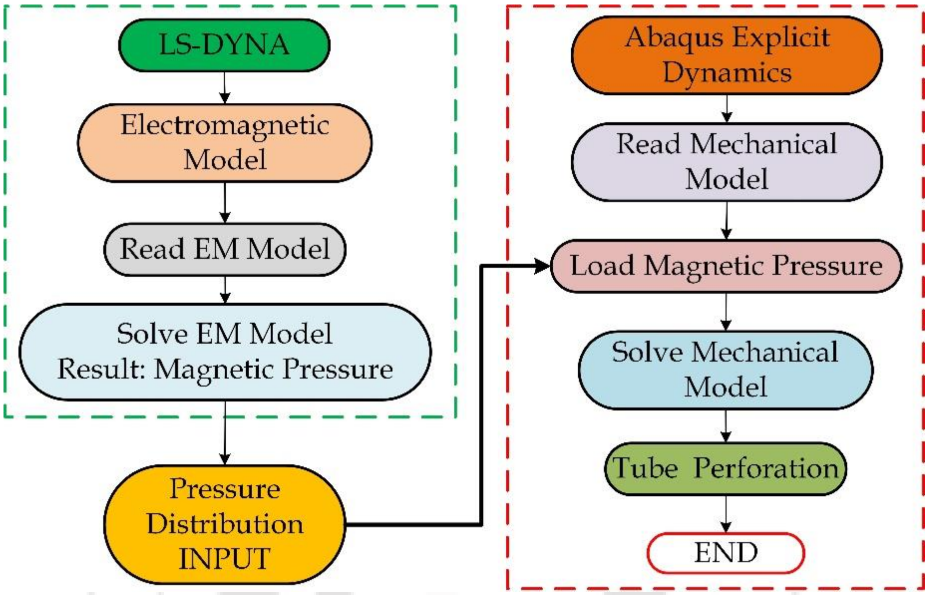

***Figure 7.2** Flowchart of simulation process*

### 7.3.1 3D Electromagnetic Simulation using LS-DYNA

The FEA study of complete electromagnetic perforation process was conducted using LS-DYNA. The FEA involves the study of EM pressure generated due to the oppositely charged magnetic field developed in coil and tube when highly damped sinusoidal current passes through the coil. The study also provides results of flow of tube material through the die opening due to the EM pressure generated and the stress accumulated at different regions along the length of the tube. The tubes with thicknesses 1, 1.5 and 2 mm were used, and the minimum energy required for EM perforation was studied. Also, different fillet radius and die angle were used during the analysis to understand the effect of fillet radius and die angle on high strain rate shearing and the shape of the sheared tube.

Figure 7.3 shows the complete 3D finite element model created for conducting a numerical study of EM perforation, incorporating tube, coil and die. The tube of 50 mm inner diameter with 1 mm thickness and 80 mm length is used as workpiece. The total elements used for meshing tube were 2020. The material of the workpiece is Al6061. The model of the tube was prepared in Pro/ENGINEER, and then the tube was meshed in HyperMesh software using hexahedral solid elements. The dimensions of the coil are 50 mm length, 9 mm pitch, 39 mm inner diameter and 2.5 mm cross-section radius. The gap kept between tube and coil is 0.5 mm. The total elements used for meshing of coil were 2300. The material of the coil is Cu 10100. The die is 80 mm in length, with 52 mm inner diameter and 2.5 mm wall thickness. The total elements used for die meshing were 4930. The die was used as a rigid body. The Johnson-Cook material model was used for tube material.

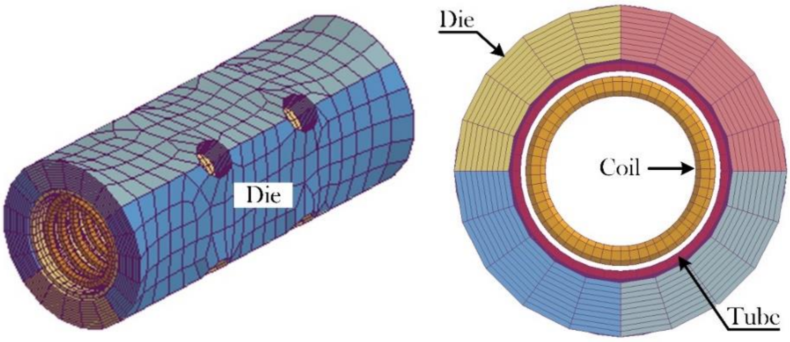

*Figure 7.3 3D model of setup used in LS-DYNA*

The resonant circuit is used to produce the damped sinusoidal current. FE analysis was carried out at different energy levels. Table 7.1 summarizes simulation conditions used for this study. The permeability and electric conductivity of materials were kept constant. The energy supplied is varied by varying the input voltage.

***Table 7.1*** *FEA Input Parameters*

| **Parameters** | **Value** |
|---|---|
| Resistance | 10.5 mΩ |
| Inductance | 440 mH |
| Capacitance | 426 µF |
| Total time taken by the simulation | 300 µs |
| Electromagnetic time step | 2 µs |

### 7.4 Results and Discussion for EM Perforation

Finite element simulation of EM perforation is carried out in LS DYNA. Simulations at different launch energies of 3.4 kJ, 5.325 kJ, 7.668 kJ, 10.437 kJ are conducted to check the deformation of the tube and to obtain electromagnetic pressure graphs.

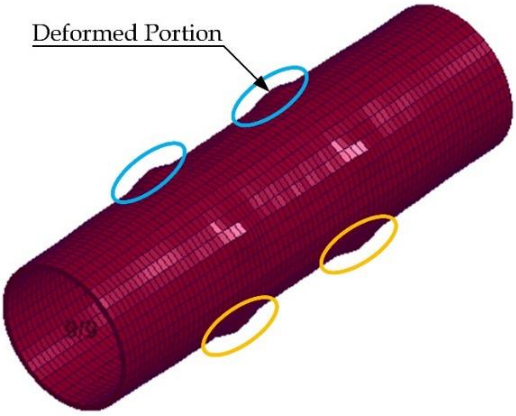

***Figure 7.4*** *Deformed workpiece at 300 µs in LS-DYNA at 7.668 kJ discharge energy*

Figure 7.4 shows the tube after the simulation. It can be concluded that the expansion of tube takes place from the hole and thus, the possibility of shearing will be near to die hole edge where the deformation of tube material is restricted.

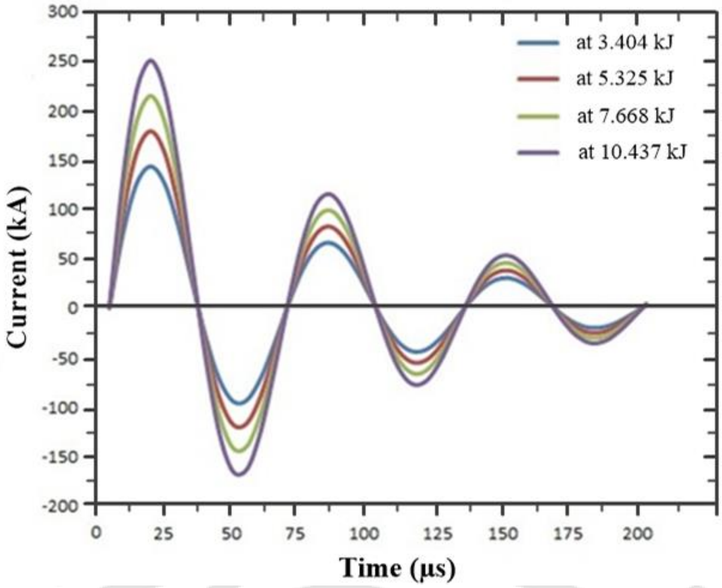

***Figure 7.5*** *Variation of current with time at different energy levels*

The variation of current with time was obtained from the simulation run at various energy levels, as shown in figure 7.5. Current waves at different energy levels are indicated by different colors. With increase in discharge energy, the increase in peak current is observed. In the graph, we can see the typical damped sinusoidal current waveform is obtained as it is characteristic of R-L-C circuit.

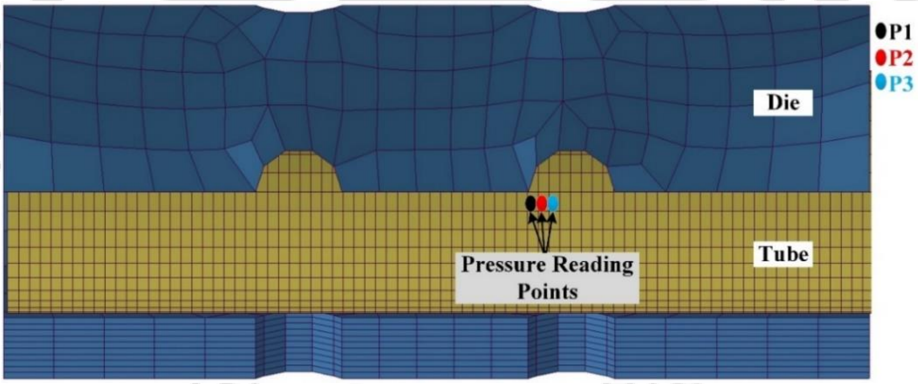

***Figure 7.6*** *EM perforation setup with points denoted for EM pressure readings*

The electromagnetic pressure results were obtained at different levels of input energy. The pressure was measured at the three different points shown in figure 7.6, and their average was taken and used as input in Abaqus/Explicit, where 2D FE model of the tube was used to study the shearing mechanism. At selected three points, probable chances of failure can be observed from stress accumulation. The selection of points is purely based on the stress concentration results. It was observed that at the tube-die interaction point, stress concentration was more which results in more pressure generation and it started decreasing towards the free tube surface. Figure 7.7 shows the variation of pressure with the time at three different points also the average pressure value generated at 5.325 kJ input discharge energy. The point P1 has maximum pressure value, as this location is restricted to deform freely because of the die edge. The point P3 is having minimum pressure comparative to others as it deforms through the die hole and the value of magnetic field strength decreases and thereby, EM pressure decreases. The curve of the pressure is damped and varying with time; this is due to the damped sinusoidal nature of the current graph.

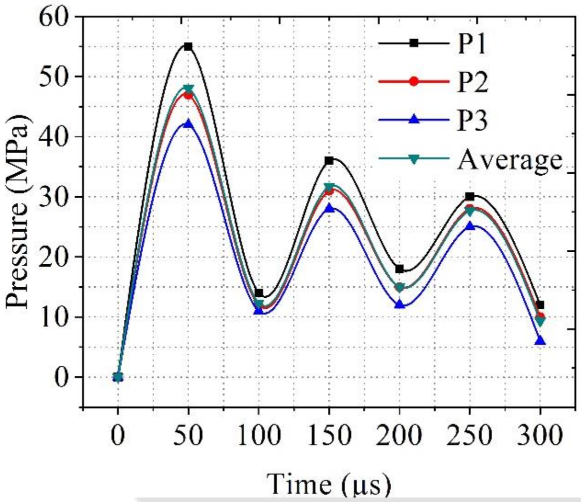

***Figure 7.7*** *Variation of pressure with time at three different points on the tube*

### 7.4.1 Transient nonlinear numerical simulation of shearing mechanism involved during EM perforation

For the study of the shearing mechanism involved in EM perforation process of the tube, a 2D solid model was developed in Abaqus/Explicit. The LS-DYNA electromagnetic module was the primary choice for the electromagnetic simulation processes as it includes an ALE solver with multi-material. Whereas Abaqus/Explicit was the best choice for studying the shearing mechanism presented in this research work because of its capabilities to handle complex contact interaction between the sheet and die by providing a node to surface contact and to handle the remeshing of tube material near to cutting zone. A finite element analysis with a similar approach was conducted in LS-DYNA, but the attempts were unsuccessful due to instabilities in the contact methods. Also, the electromagnetism module of LS-DYNA has a limitation of a number of elements to be used for the analysis, which prevents use of fine meshing near the cutting edge.

In this simulation, the tube was modeled using solid element. For maintaining the accuracy of results, fine mesh was used near the cutting edge. The tube was modeled with 30 elements through its thickness in the area near the cutting edge, and comparatively coarser elements were used in the rest area of the tube to save the analysis run time as shown in figure 7.8. Johnson-Cook (JC) failure model is used for handling the failure of the element at high strain rate. The reported simulation was carried out in plane strain conditions such that ε_33=0 and assuming the restriction to flow of material normal to the plane of 2D section.

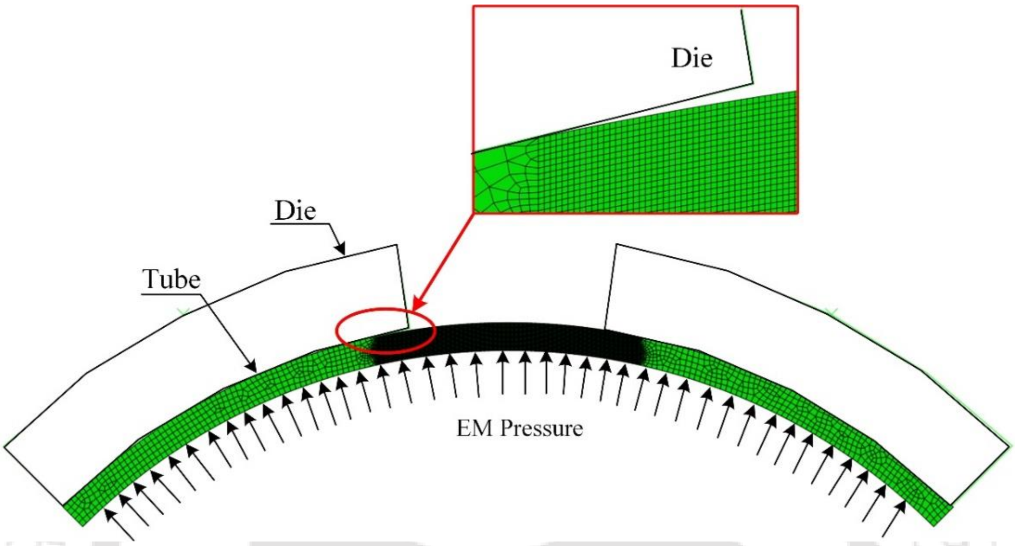

***Figure 7.8*** *Quadrant meshed 2D model of tube showing the EM pressure applied*

Electromagnetic perforation is high strain rate process. In this process the tube undergoes large plastic deformation and to achieve a reduction in distortion adaptive meshing method, Arbitrary Lagrangian-Eulerian (ALE) is used. The quadrilateral (QUAD) plane strain element (CPE4R) was used to model the tube. Once the JC damage parameter values at any element reach to unity, the element gets deleted. Initially, between free surfaces of die and tube, surface to surface contact is defined. However, once the element on the top surface of the tube gets deleted there can be tool to tube mesh part penetration and to avoid it, additional contact is provided between nodes of tube mesh part and die surface. After the deletion of damaged element, the additional contact ensures that the die will remain in contact during the simulation with the exposed elements. Figure 7.9 shows the contact interaction defined between the 2D tube model nodes (highlighted in pink) and die surface (highlighted in red). Also, an initial surface to surface contact is defined amongst the die left surface (highlighted in red) and tube upper surface (highlighted in yellow). For examining the shearing mechanism of the Al6061 sheet at high strain rate process, electromagnetic pressure, which was calculated from the simulation conducted in LS-DYNA was averaged and applied to the bottom of the 2D tube model in Abaqus/Explicit. The average value of pressure which was used as the input EM pressure varying with time is given in table 7.2.

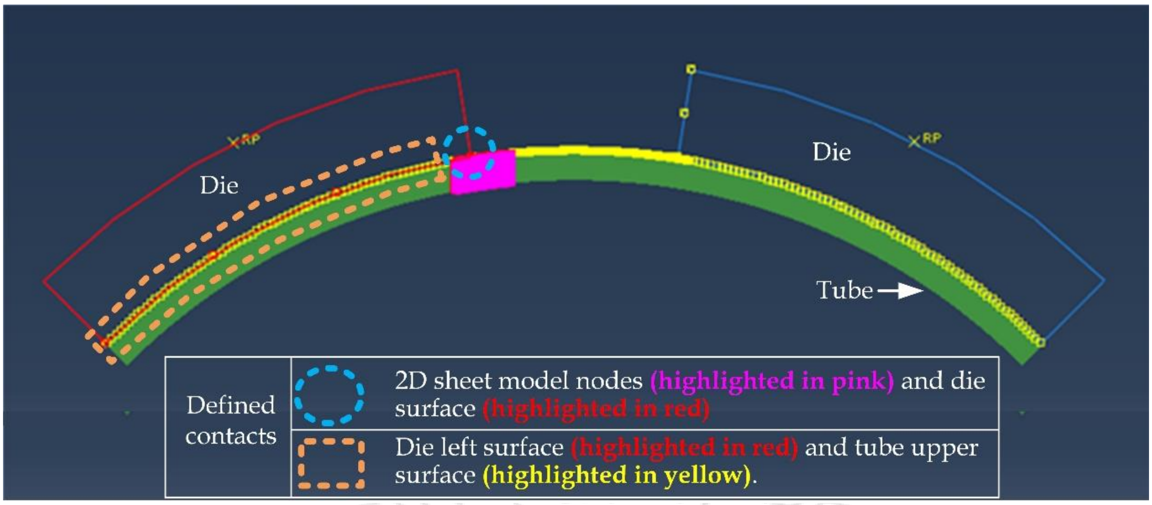

***Figure 7.9*** *Showing tool surface contact with internal slug nodes*

***Table 7.2*** *Input EM pressure varying with time*

| **Time (μs)** | 50 | 100 | 150 | 200 | 250 | 300 |
|---|---|---|---|---|---|---|
| **Pressure (MPa)** | 45 | 12 | 31 | 15 | 28 | 8 |

### 7.4.2 Simulation of Slug separation

Figure 7.10 shows the slug separation. As the slug is moving upward, the failure starts to compile in an area near to the trim edge. The initiation of fracture is observed at 65 μs on the top surface of the slug, which further propagated towards the bottom of the slug. The slug is completed separated from the tube at 71 μs. Figure 7.10 shows the contours obtained when at integration points Johnson-Cook damage initiation criterion is used.

The variation of pressure with time was obtained from the final perforated geometry. Figure 7.11 shows the graph plotted at an element from the geometry. The pressure at the element rises quickly up to 50μs causing the element to delete due to shearing. And once the element is deleted, it falls quickly to zero. The graph thus concludes the impact shearing nature of EM perforation process.

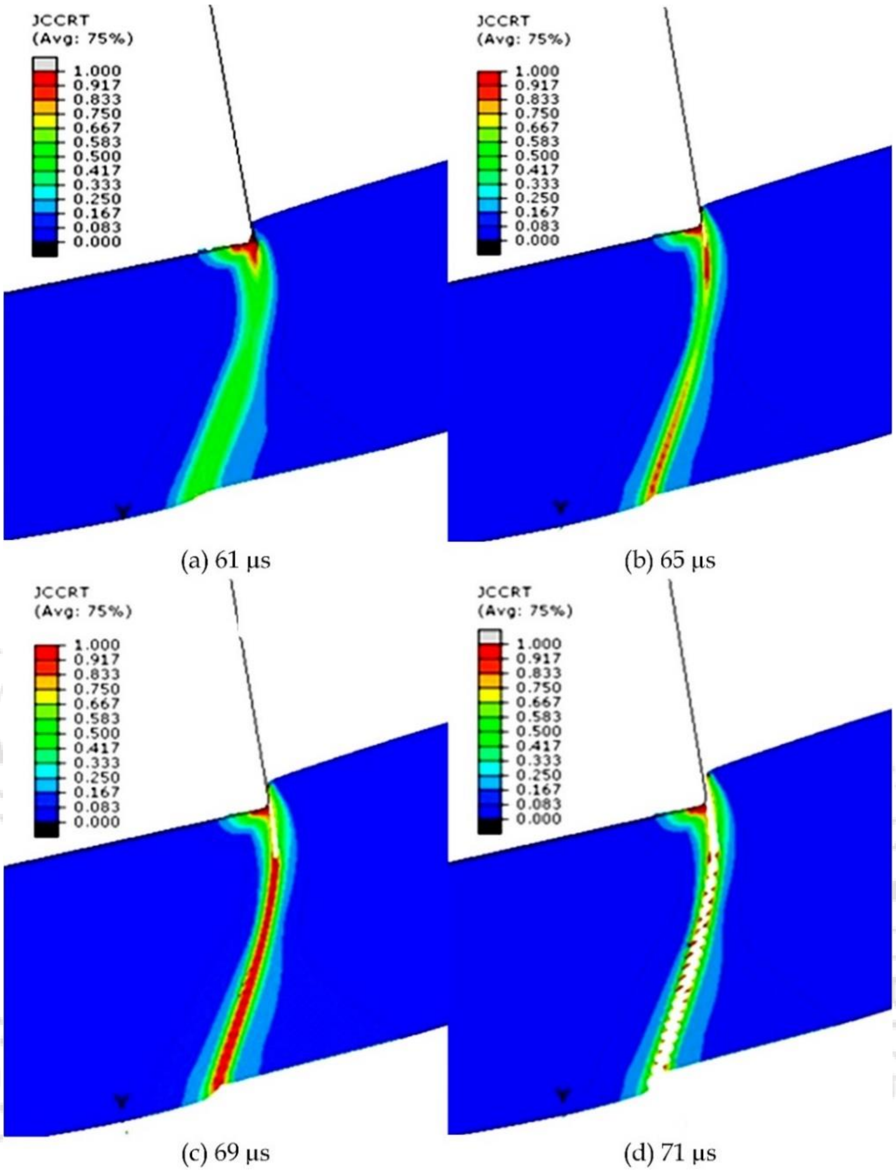

***Figure 7.10*** *Fringe pattern of JCCRT at (a) 61 µs, (b) 65 µs, (c) 69 µs and (d) 71 µs*

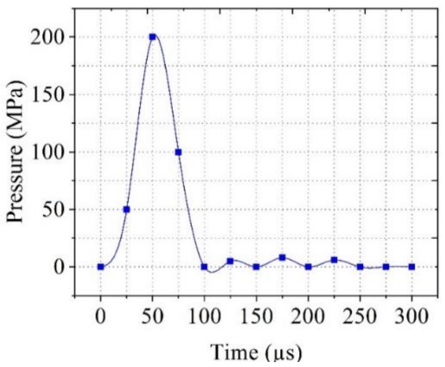

***Figure 7.11*** *Variation of pressure with time obtained from perforated tube*

The simulations were conducted, keeping different die angles to check the effect of die angle on the shape of the final geometry as well as on the plastic equivalent strain. For the EM perforation giving a small fillet radius to the die, the sheared face edge improves.

Figure 7.12 shows the result of the simulations. We can see the geometry obtained by 50 die angle was better than the other angles. The sheared off face appearance was smooth when 50 die angle was used.

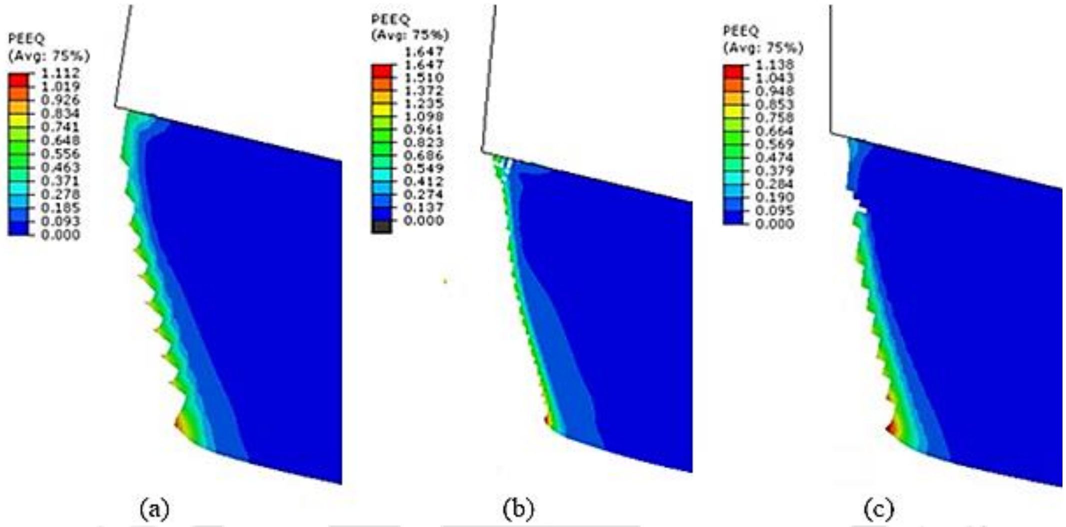

***Figure 7.12*** *Plastic strain fringe when (a) 80 die angle, (b) 50 die angle, (c) no die angle*

The sheared off face obtained with 50 die angle was best and thus, different fillet radius was used with 50, and the simulations were conducted as shown in figure 7.13. The 30 µm fillet radius results in good quality sheared off face as compared to 100 µm radius as shown in figure 7.13.

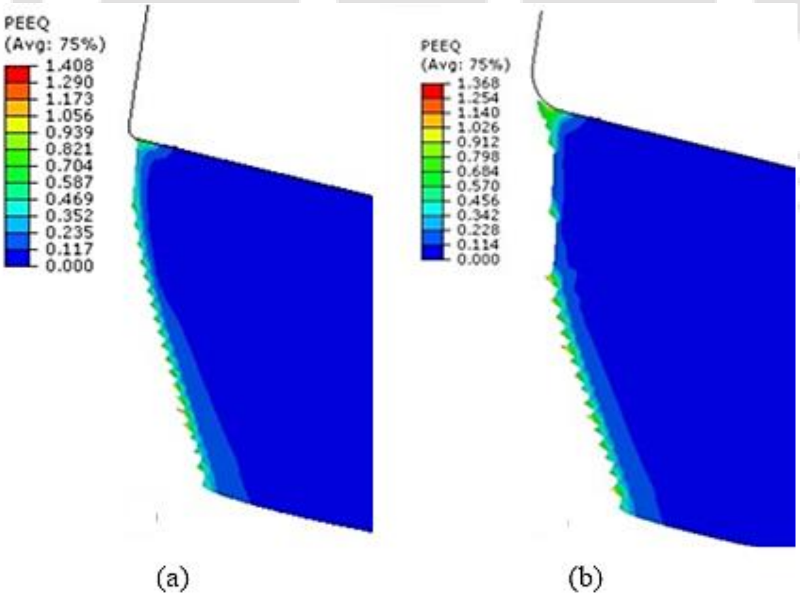

***Figure 7.13*** *Simulation results at different fillet radius (a) 30 µm, (b) 100µm*

### 7.4.3 Results of Simulation of 2 mm Al6061 Tube

A similar simulation process was conducted for 2 mm Al6061 tube. First, the 3D model was run on LS-DYNA with the same process parameters and same material model at different energies levels, as discussed above, to obtain electromagnetic pressure required for penetration. Then the different pressure values obtained were used in a 2D model of the tube in Abaqus/Explicit to study the pressure required and thus the energy required for perforating 2 mm thick tube.

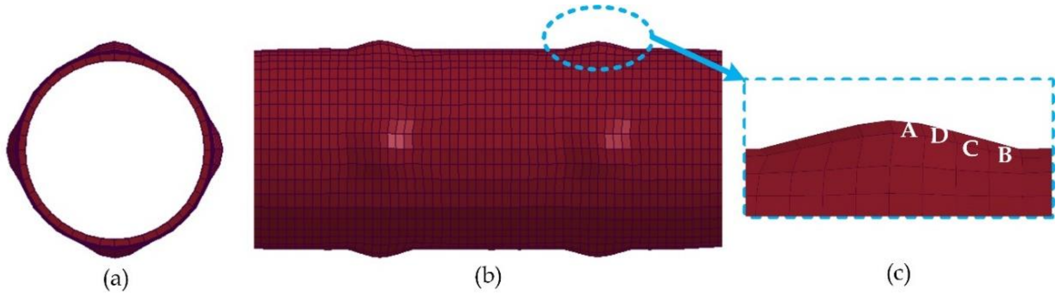

***Figure 7.14*** *(a) Front view, (b) Side view and (c)Magnified image showing elements where pressure is measured*

Figure 7.14 (a) and (b) shows the front and side view of the expanded tube in LS-DYNA at 13.625 kJ discharge energy. The pressure measured at four different elements is shown in figure 7.14 (c). The enlarged view of the tube near the perforation zone shows the tube expanded through the hole of the die and the selected elements for obtaining pressure. The pressure is measured at three different energies 5.325 kJ, 7.668 kJ, and 13.625 kJ, respectively. The pressure obtained from 5.325 kJ and 7.668 kJ were insufficient for perforating holes. Figure 7.15 shows the variation of pressure with time when the simulation was run using 13.625 kJ of energy.

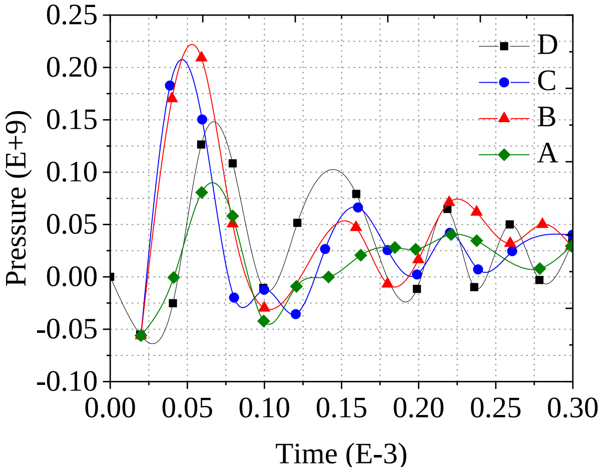

***Figure 7.15*** *Variation of pressure with time obtained from the simulation of 2 mm tube at four different points (A, B, C, D shown in Figure 7.14)*

The average value of the graph was then plotted as shown in figure 7.16 and values were used as input in Abaqus/Explicit. These pressure values were used as input pressure varying with time in perforating the 2D model of a tube having 2 mm thickness. Figure 7.17 shows the 2D model of tube perforation in Abaqus/Explicit.

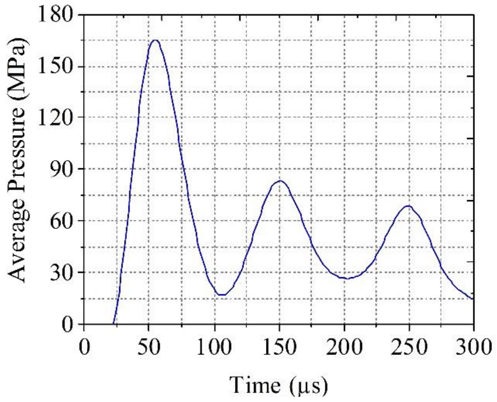

***Figure 7.16*** *Variation of averaged pressure with time*

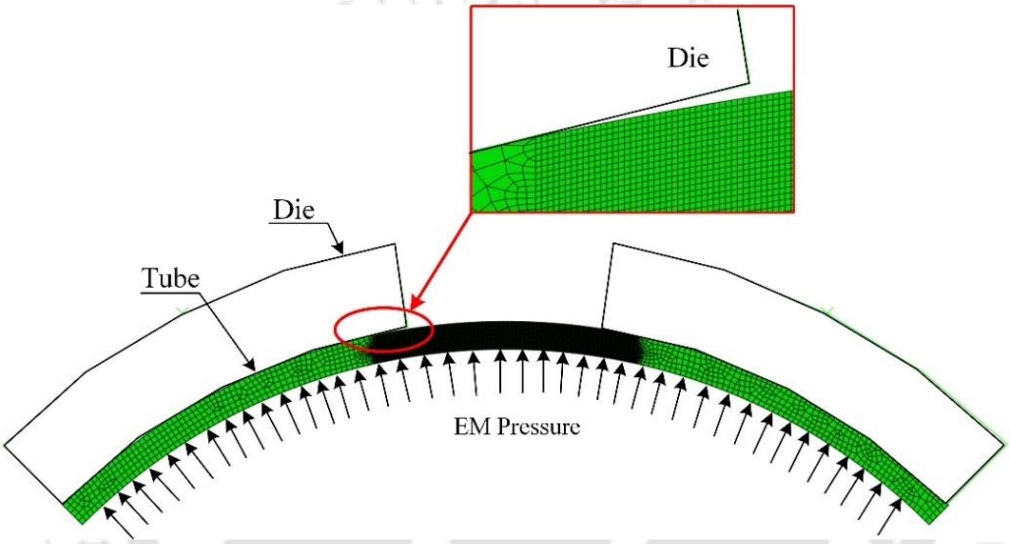

***Figure 7.17*** *Numerical model of the EM perforation process in Abaqus/Explicit*

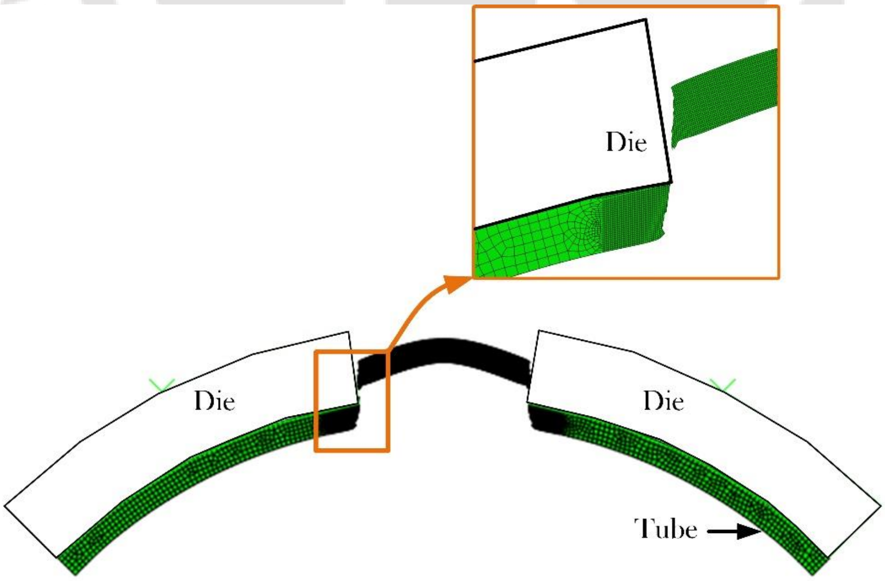

***Figure 7.18*** *Final deformed shape the 2 mm perforated tube*

The final deformed shape can be seen in figure 7.18. The scrap-side of tube is moved upward away from part. The shearing mechanism was found similar for every thickness of the tube. At 80 µs the scrap side was detached from the part side. Similarly, the simulation was also carried out for the 1.5 mm thick tube.

### 7.5 Conclusion

A hybrid approach for finite element analysis of EM perforation of tubes was successfully conducted and demonstrated in this research work. The crack initiation and propagation are clearly captured by the developed numerical model, in the results it can be seen that the shearing starts from the die side and propagates towards the side where EM pressure is applied; hence the burr is transferred from part to the scrap. Thus, this ensures that the sheared off face will have improved face geometry as compared to conventional perforation process. The results pointed out that the energy required for shearing is influenced by the thickness of the tube. The minimum energy required for perforation of 1 mm thick Al6061 tube was 5.325 kJ and for perforation of 2 mm thick Al6061 tube was 13.625 kJ. The effect of die angle and fillet radius was also successfully demonstrated. These factors show the influence on the appearance of the sheared off face. A small fillet radius of around 30 µm shows better-perforated geometry.

# Chapter 8

# FE and Experimental Analysis on EM Punchless Forming of Muffler[v]

---

## 8.1 Introduction

Now a day near net shape manufacturing technologies produce components those are close to the finished size and shape, requiring a minimal amount of finishing process. In the earlier chapters the feasibility of electromagnetic forming and perforation (EMFP) process is established. As stated, in EMFP, the simultaneous forming and perforation is possible which eliminate the number of process involve in manufacturing of deformed tube. Similarly, this chapter can be seen as application of the EM forming processes where the feasibility study of electromagnetic forming of muffler tube is carried out which may result in near net shape of muffler tube. The muffler is part of a noise reduction system placed in the IC engine. Normally they are made out of steel. The density of steel is almost three times of the density of aluminium. In an automobile, the weight of the part plays a vital role in improving efficiency. Use of aluminium reduces the weight of muffler significantly which will lead to an increase in efficiency of the automobile. The muffler produced by conventional manufacturing mostly fails in the region of the weld zone as shown in figure 8.1. In this study, experiments are carried out on EM forming of Al muffler which results in a single piece of component of desired shape, hence eliminating the weld zone to extend the working life of muffler.

***Figure 8.1*** *(a) Muffler, (b, c) Failure at the weld zone*

In this chapter, experiments are carried out on the EM forming of a muffler. The EM forming of a muffler takes place within a fraction of microsecond, so it is very hard to find out strain behavior as well as the velocities of flowing material experimentally, hence,

---

[v] *Pawar, S. H., Kore, S. D., & Nandy, A. (2020). FE Analysis of Effect of Variation in Coil length and Coil-tube Relative Positions on Establishment of Magnetic Fields and Distribution of Velocities in Electromagnetic Forming of Muffler Tube. Procedia Manufacturing, 47, 659-664.*

numerical simulations are inevitable. To study these parameters numerically, a new coupled finite element model is developed in LS-DYNA™ EM module.

### 8.2 Experimental Methodology

The detail working principle of electromagnetic forming of muffler tube and experimental details are explained in chapter 3, section 3.2.3. Here, experiments are carried out on Al 6061 tube having 1 mm thickness, 100 mm length and 50 mm outer diameter.

### 8.2.1 Strain Measurement for Formability Analysis

Forming limit diagram is used to represent the forming behavior of the material. For the measurement of strain, grid of circles is imprinted on the lateral tube surface by chemical etching.

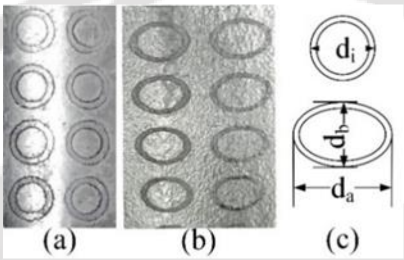

***Figure 8.2*** *Grid imprints (a) Before the experiment, (b) After the experiment and (c) Measurement*

After the forming experiment, major and minor diameters of the elliptical grids measured with the help of an optical microscope. Figure 8.2 shows the magnified image of grids captured at the same section on the tube before and after the experiment.

### 8.3 Finite Element Model

Electromagnetic forming is a combination of thermal, mechanical and electromagnetic phenomenon. Electromagnetic module available in LS-DYNA™ is used for simulating the electromagnetic forming process. EM module is governed by Maxwell's eqns as explain in chapter 3, section 3.3.1. In LS-DYNA™, both electrical, as well as mechanical solution takes place, so it is called a coupled simulation. The dynamics of the electromagnetic field is taken care by the electromagnetic module and the mechanical solver deals with the mechanics of material flow. The flow chart of coupled behavior in LS-DYNA™ is explain by figure 3.13.

### 8.3.1 Modeling of EM Forming of Muffler Setup

Al 6061-T6 tube with the outer diameter of 50 mm and 1 mm wall thickness is used in the simulation. The dimensions of coil and die are same as that of the experiments. Three different coils as shown in figure 8.3 named coil 1, coil 2, and coil 3 with varying lengths of 80 mm, 100mm and 120 mm respectively are used in the simulation for finding out the optimum length of the coil. Cu alloy is used as material for coil. A 16 mm2 Cu cable is used for the making of coils. The details of the elements and nodes are mentioned in table 8.1.

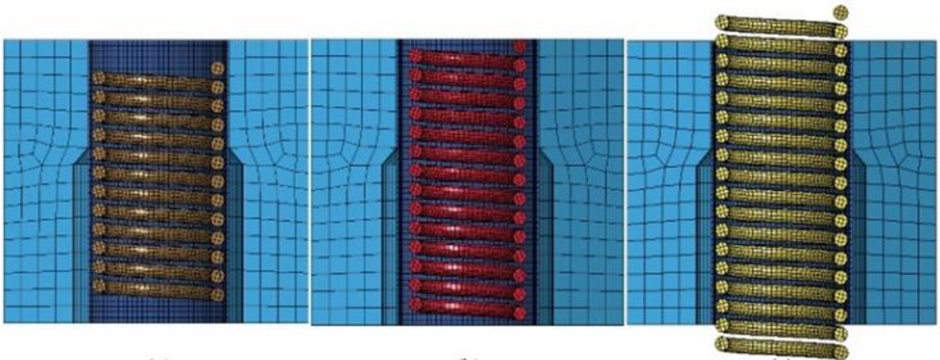
(a) (b) (c)

***Figure 8.3*** *Different coils (a) 80 mm, (b) 100 mm and (c) 120 mm*

***Table 8.1*** *Elements and nodes*

| **Part** | **No. of elements** | **No. of nodes** |
|---|---|---|
| Die | 4526 | 5985 |
| Tube | 4000 | 8160 |
| Coil 1 (80 mm length) | 7119 | 12672 |
| Coil 2 (100 mm length) | 7344 | 13072 |
| Coil 3 (120 mm length) | 10683 | 19008 |

Johnson-Cook material model is used in the FE model to describe the constitutive behavior of metals at high strain rates over a wide range of strain and temperature. To analyze this behavior, 015-JOHNSON COOK material model available in LS-DYNA™, is used. The constitutive equation for the model is given by equation 2.17. The parameters taken for the model are given in chapter 3, section 3.4. The current waveform obtained from the oscilloscope is used as current input in the circuit parameters.

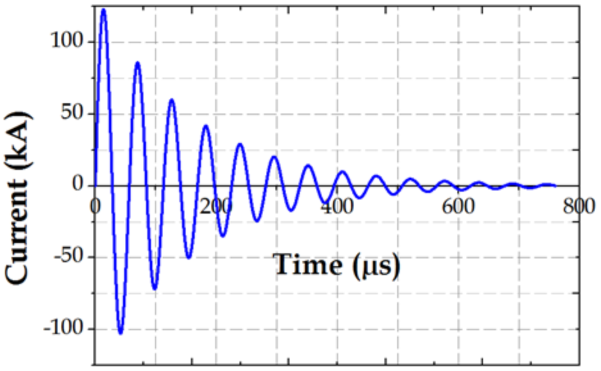

***Figure 8.4*** *Current waveform obtained at 6.5 kJ discharge energy*

Figure 8.4 shows the current curve used for the simulation obtained at 6.5 kJ discharge energy during the experiment. The ceramic material is used for defining the properties of the die. For both the coil and die, 020 RIGID material model used in the LS-DYNA™. The properties of all materials used are given in chapter 3, section 3.4. Simulation conditions used for this finite element model are given in table 8.2.

***Table 8.2*** *Simulation conditions applied in LS-DYNA™*

| **Conditions** | **Value** | **Unit** |
|---|---|---|
| Total time period (t) | 3e-5 | s |
| Initial temperature (T) | 300 | K |
| Time step scale factor ($t_s$) | 0.1 | s |

## 8.4 Results and Discussion

Experiments are carried out on 1 mm thick Al tubes at different energies to find out the optimum energy for maximum gap filling. Effect of coil length and coil position on deformation pattern and effect of discharge energy on gap filling and strain rate are studied.

### 8.4.1 Effect of variation in the length of the coil

Different simulations are carried out at different discharge energies to the study the effect of variation of length in the coil on the magnetic field and velocity obtained. Figure 8.5 shows the magnetic field variation at different discharge energies.

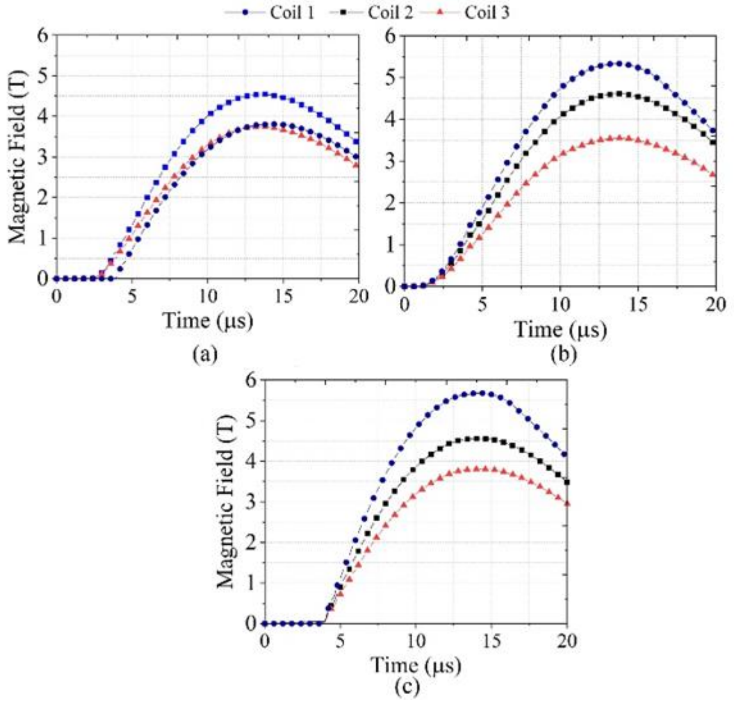

(a) (b) (c)

***Figure 8.5*** *Magnetic field distribution obtained at the center of the tube using different (a) at 5.0 kJ, (b) at 5.6 kJ and (c) at 6.2 kJ*

It is observed that with the increase of the length of the coil, the magnetic field is decreasing. It is because the magnetic field is inversely proportional to the length of the coil. Although the maximum pressure is obtained for coil 3 at the end of the tube, as shown in figure 8.6 (c), the maximum deformation or gap-filling is possible with the coil 2 as it can be seen that the uniform expansion of the tube is possible for the same coil. The deformation obtained in all three cases is shown in figure 8.7.

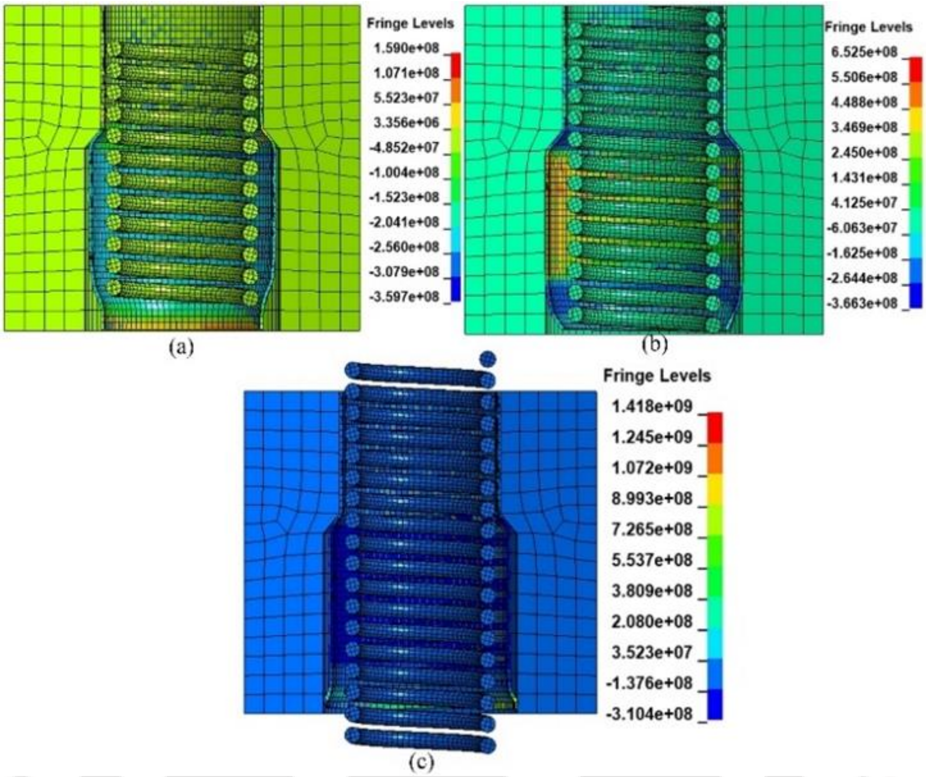

***Figure 8.6*** *Magnetic pressure distribution at 6.2 kJ discharge energy for (a) Coil 1, (b) Coil 2 and (c) Coil 3*

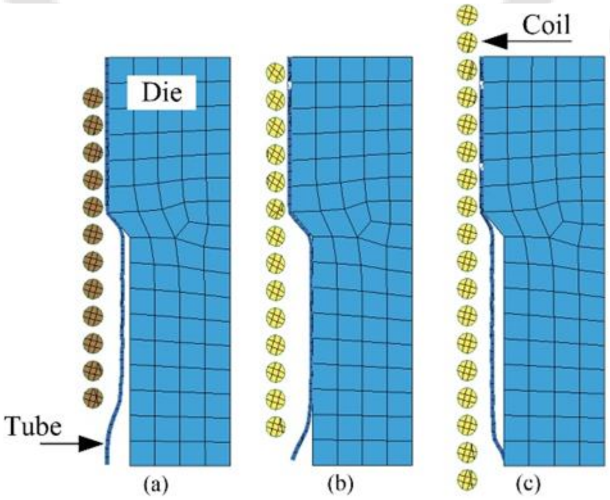

***Figure 8.7*** *Deformation obtained at 6.2 kJ discharge energy for (a) Coil 1, (b) Coil 2 and (c) Coil 3*

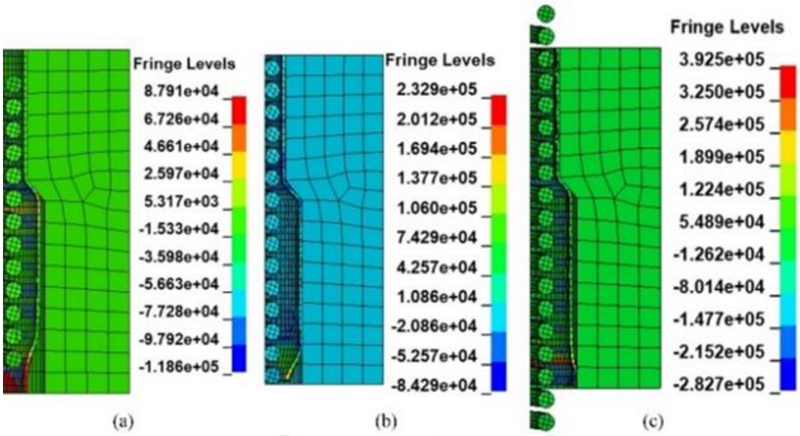

***Figure 8.8*** *Velocity distribution obtained at 6.2 kJ discharge energy for (a) Coil 1, (b) Coil 2 and (c) Coil 3*

The velocity distribution obtained by using three different coils is shown in figure 8.8. It is observed that a minimum of 87 m/s velocity is required to deform the Al tube. In the case of coil 3, the maximum velocity of 392 m/s is observed at the end of the tube as the maximum magnetic field is observed at the same location. The uniform distribution of the magnetic field is observed in the case of coil 2 which is responsible for the maximum gap filling. For further study, the coil of 100 mm length is used. The developed simulation model is validated with experimental data for the case where 80 mm length coil is used. The experiment is carried out at 5.2 kJ discharge energy. For validation, the deformation obtained in simulation is compared with the available experimental results. The 94% agreement is observed between the numerical and experimental results. Figure 8.9 shows the comparison of deformation obtained in the experiment with the simulation.

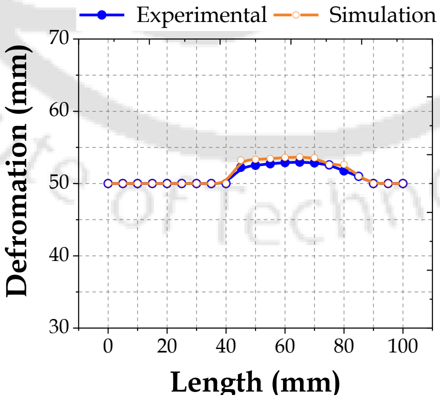

***Figure 8.9*** *Validation of simulation model for deformation obtained*

### 8.4.2 Effect of Coil Position (along tube length) on Deformation Pattern

The axial position of the coil defines the deformation patterns. In this section, four types of coil position, as shown in figure 8.10 are used, and the deformation patterns are observed. Experiments are carried out at 5.6 kJ discharge energy. Finite element simulations are carried out on the same discharge energy using the current waveform obtained from the oscilloscope.

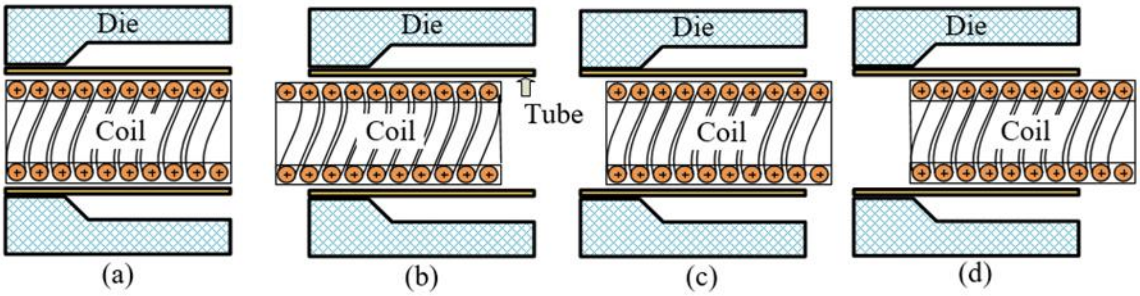

***Figure 8.10*** *Coil positions (a) Coil covers tube length, (b) 1 turn outside from left end, (c) 1 turn outside from right end (d) 2 turn outside from right end of the tube*

Earlier, in the literature, it is observed that the maximum magnetic field is present at the middle of the coil, which results in maximum deformation at the centre of the tube [8]. Figure 8.11 shows the vector plot of the Lorentz force distribution along the length of the tube. The maximum values of the Lorentz force on the tube at different coil positions are 194 N, 104 N, 510 N and 100 N respectively.

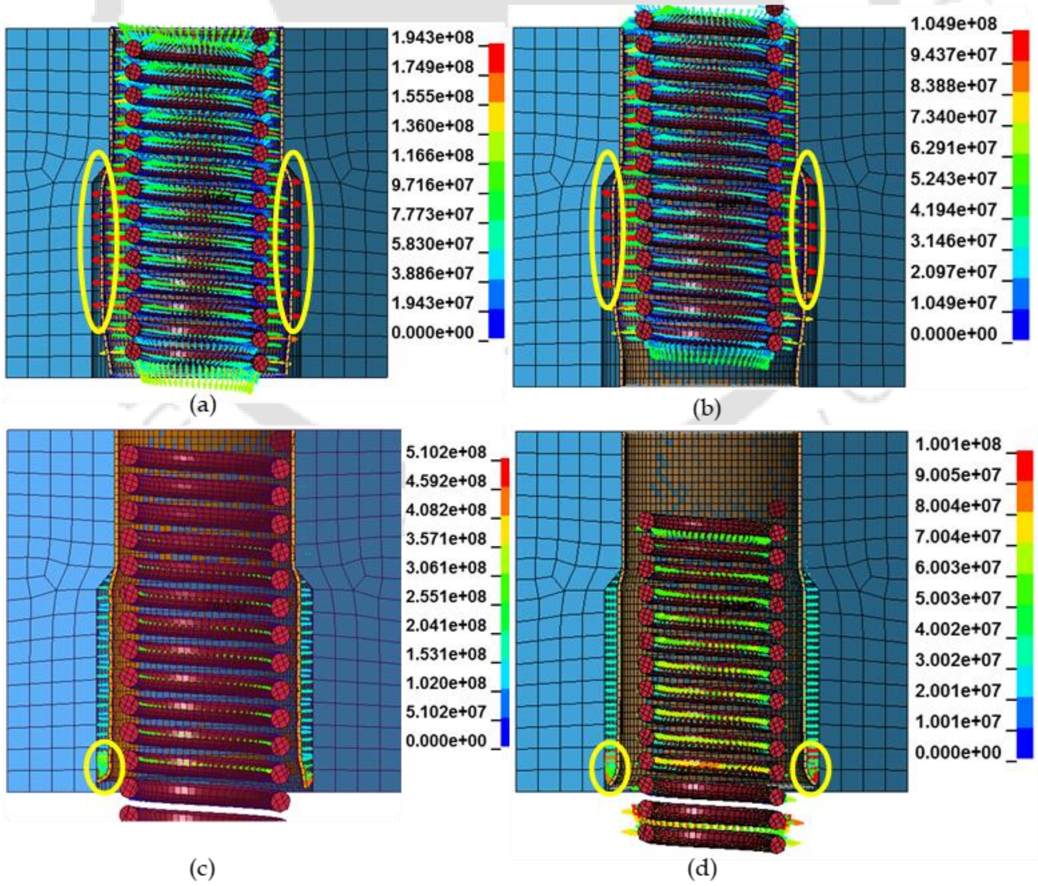

***Figure 8.11*** *Lorentz force distribution along the length obtained in simulation (a) Coil covers tube length, (b) 12 mm outside from left end, (c) 12 mm out from right end (d) 24 mm out from right end of the tube*

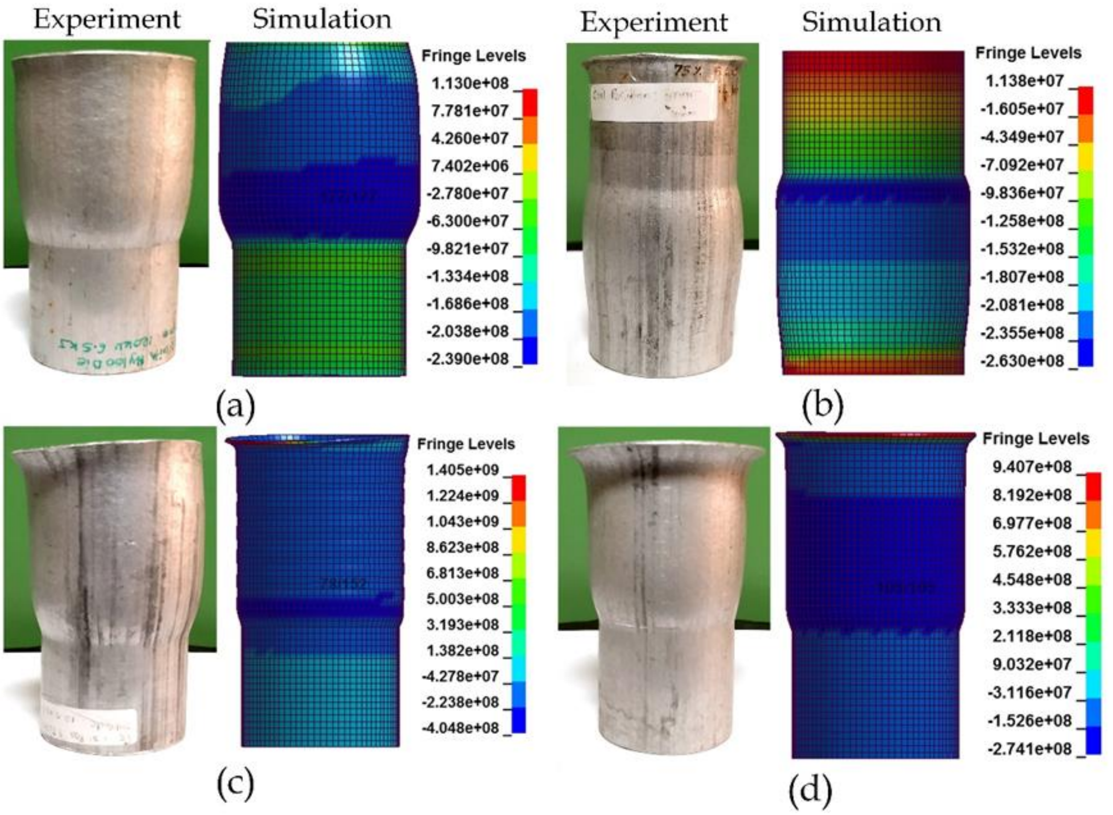

***Figure 8.12*** *Tubes after the experiments and after simulation where coil (a) Covers tube length, (b) 1 turn outside from left end, (c) 1 turn outside from right end (d) 2 turn outside from right end of the tube (Fringe level shows stress in Pa)*

Figure 8.12 shows the comparison of deformation patterns obtained in finite element simulations with the experimentally deformed tube. In the first case, the coil covers the length of the tube which results in uniform tube bulging. Compared to all other situation, in the case when coil covers the total length of the tube, maximum Lorentz force on the tube at the required area is observed, which results in maximum deformation in the desired location. In case 2, the coil is placed one turn outside from the left end of the tube, which results in non-uniform deformation. In case 3 and case 4, one and two turns of the coil are kept outside the right end of the tube respectively. In these two cases, the magnetic pressure at the tube end is more than that present at the center, results in flanged shape. Figure 8.13 shows the comparison of variation of deformation pattern with respect to coil position in experiment and simulation runs. As shown in figure the simulation successfully captured the material movement and effect of coil postion on deformation. Around 95% agreement between experiment and simulation run is observed in all the cases. Among all the positions, when the coil covers the length of the tube, the magnetic field generated and obtained deformation is maximum, therefore for all further study, this coil position is used.

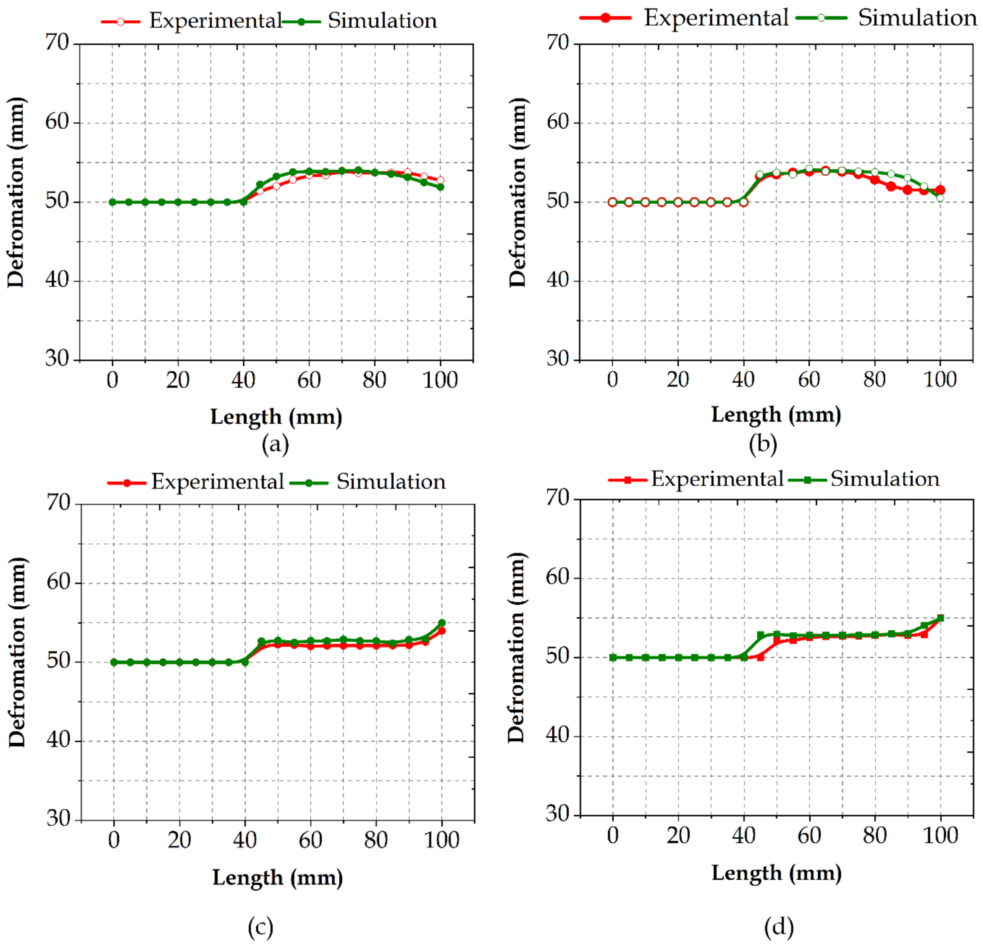

*Figure 8.13 Validation of simulation results with experimental for coil (a) Covers tube length, (b) 1 turn outside from left end, (c) 1 turn outside from right end (d) 2 turn outside from right end*

### 8.4.3 Effect of Discharge Energy on Gap Filling

The experiments are carried out to find out the optimum discharge energy for maximum gap filling. The discharge energies were varied from 3.0 kJ to 6.5 kJ.

***Figure 8.14** Tubes after the experiments at different discharge energies*

The significant deformation is observed after 5.0 kJ discharge energy as shown in figure 8.14. As shown in figure 8.14 (d), at 6.50 kJ discharge energy the failure of the tube is observed.

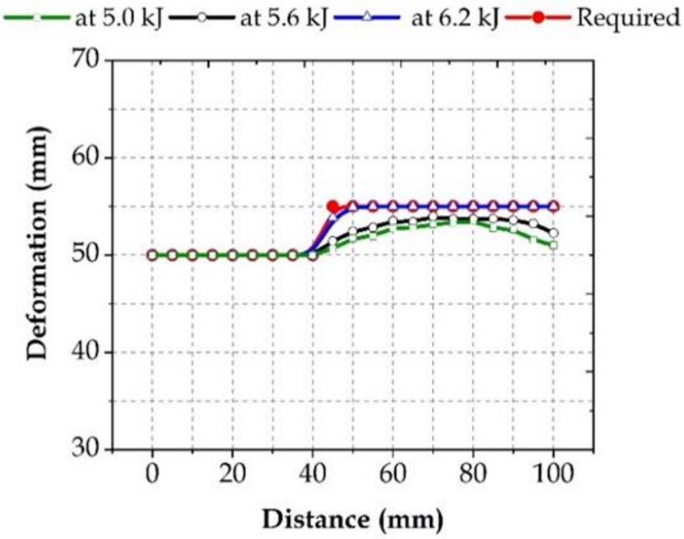

*Figure 8.15* *Variation of deformation with discharge energy*

For measurement of deformation after the experiment, the tube is cut into the half part and measurements are taken on the Coordinate Measuring Machine (CMM). As shown in figure 8.15, it is observed that with the increase of discharge energy the deformation is also increased. Finite element simulations were carried out on the same discharge energy using the current waveform obtained from the oscilloscope. Figure 8.16 shows the variation of von-Mises stresses in the tube along length at different discharge energies.

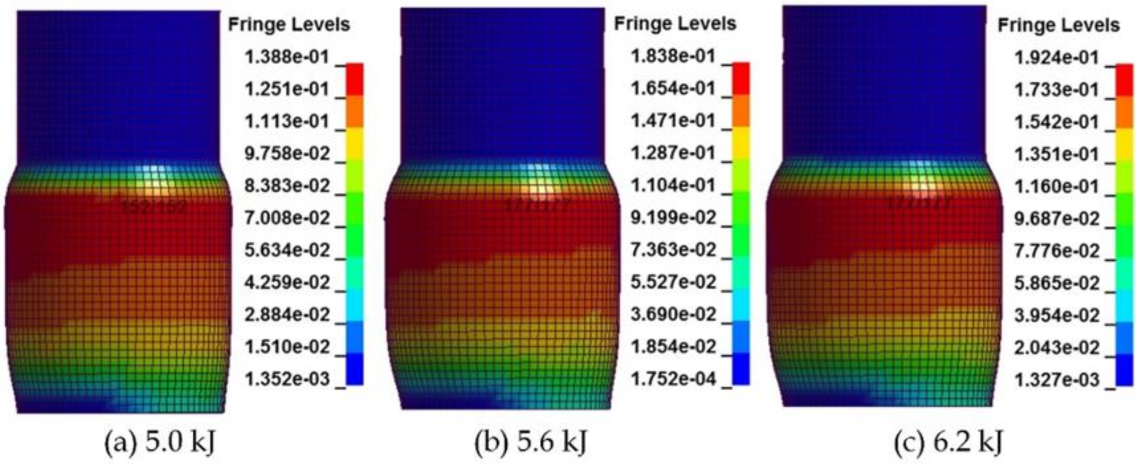

(a) 5.0 kJ (b) 5.6 kJ (c) 6.2 kJ

*Figure 8.16* *Effective plastic strain distribution at various discharge energies*

The von-Mises stresses are increasing with an increase in discharge energy. Maximum of 305 MPa von-mises stress is observed at 6.2 kJ discharge energy which is below to the ultimate strength of material (310 MPa) and greater than the yield strength (275 MPa). The appearance of maximum stresses at the center of the tube indicates maximum magnetic field generation at the center. It also suggests that after 6.2 kJ discharge energy, the tube may fail at the center. After the experiment and successful simulation run, for finding out the percentage of gap filling, measurement of deformation is carried out at three zones. The zones for measurement are shown in figure 8.17.

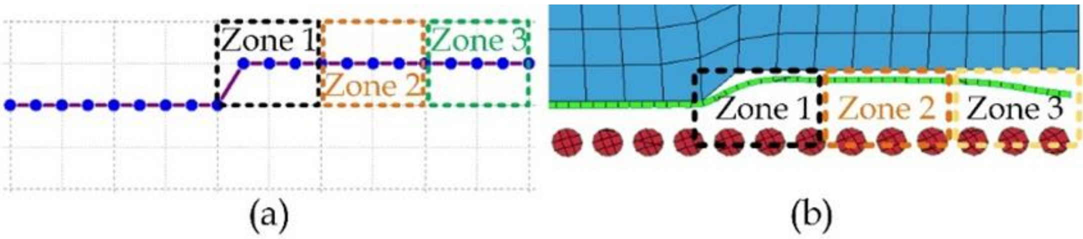

(a) (b)

***Figure 8.17*** *Zones of measurement (a) On tube using CMM and (b) During simulation measurement*

Figure 8.18 shows the percentage of gap filling with discharge energy in the experimental run. Figure 8.19 (a), (b) and (c) shows the validation of simulation results with experimental measurement for the percentage of gap-filling at various discharge energies at three different zones. In all the cases gap-filling percentage is higher in the case of zone 2 because of higher magnetic field generation. At 6.2 kJ discharge energy, the percentage of gap filling is 90.483% at zone 1, 98.15% at zone 2 and 99.985% at zone 3. The obtained gap-fill filling percentage is more compared to other lower energies. It observed that in all the cases, the variation between simulation results and experimental results is minimal. The finite element analysis results are found more than 95% agreement with the experimental result.

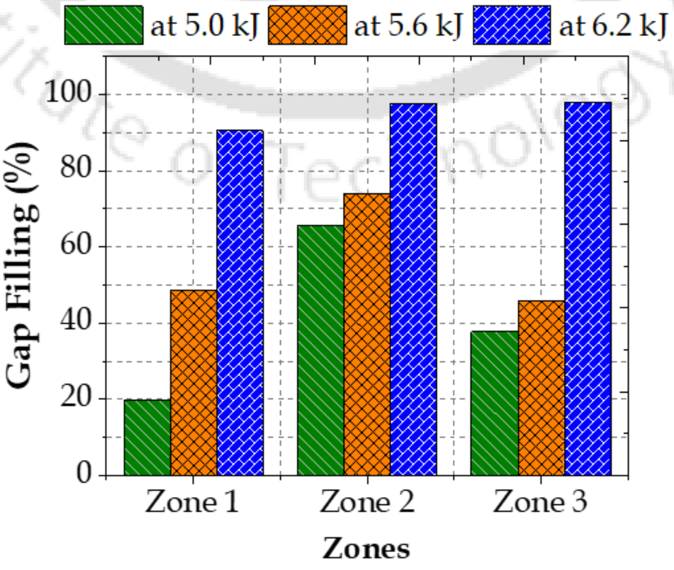

***Figure 8.18*** *% gap filling with discharge energies in experimental runs*

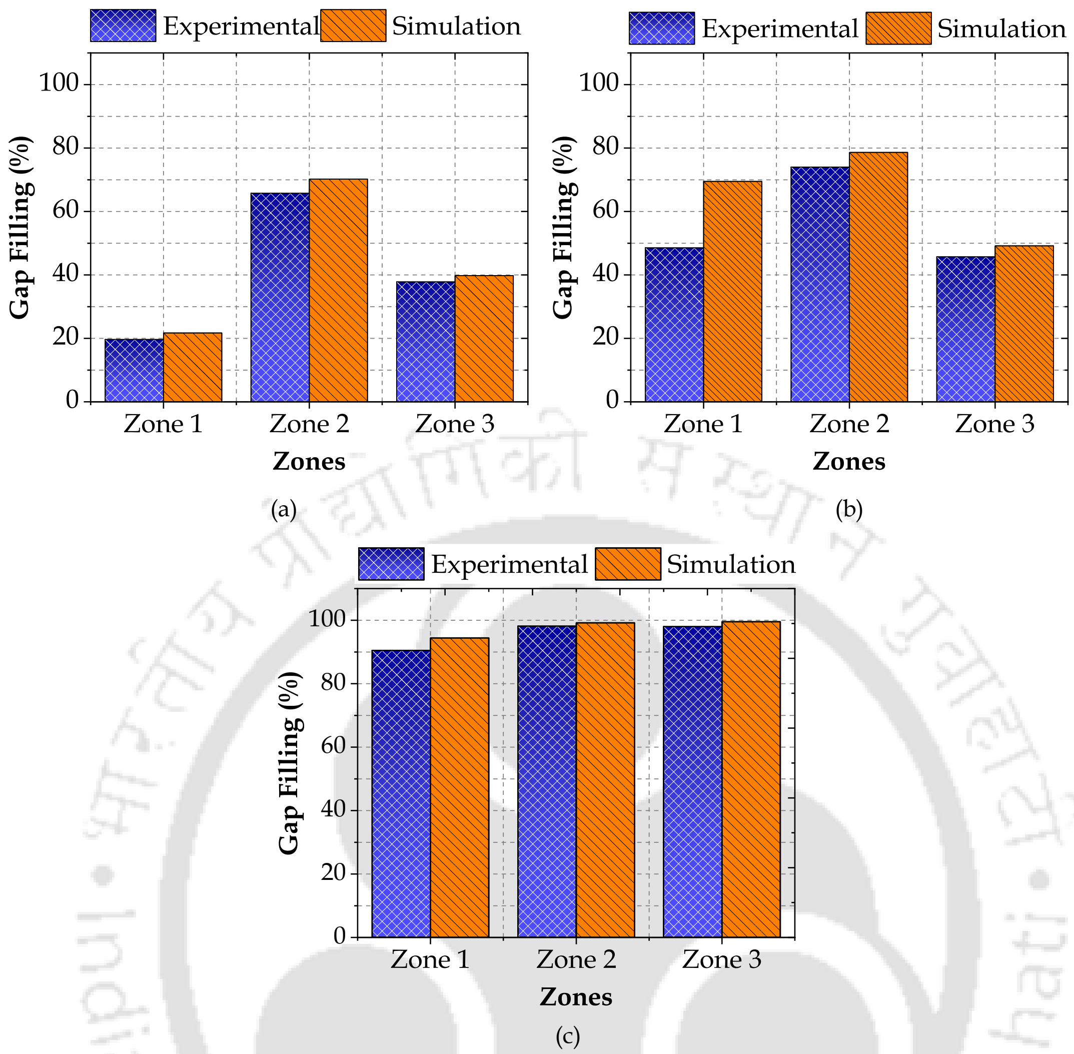

***Figure 8.19*** *% gap filling with discharge energies, validation of simulation results with experimental (b) at 5.0 kJ, (c) at 5.6 kJ and (d) at 6.2 kJ discharge energies*

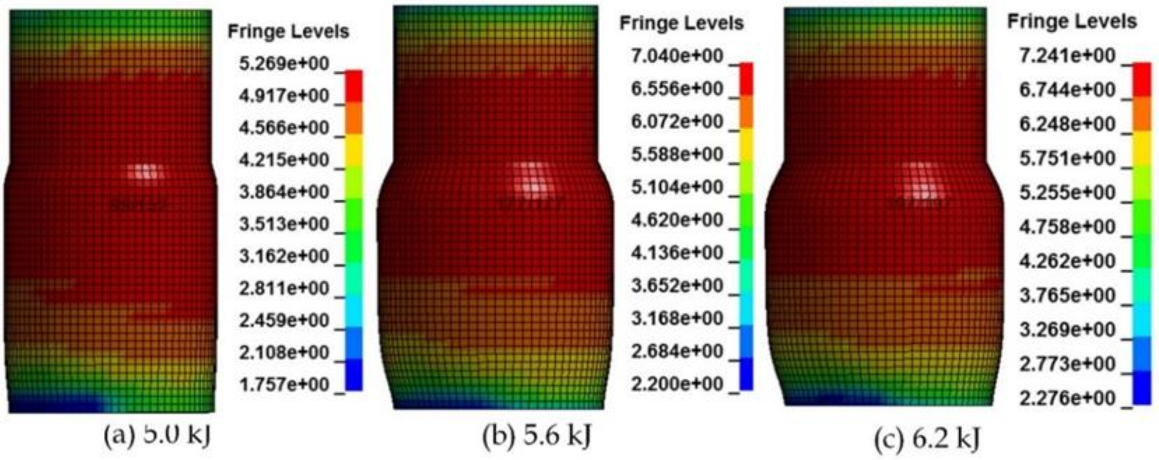

(a) 5.0 kJ (b) 5.6 kJ (c) 6.2 kJ

***Figure 8.20*** *The magnetic field distribution in the tube at various discharge energies (Fringe level unit is Tesla)*

The magnetic pressure is proportional to the current, and it increases with the peak current. Magnetic field distribution at all discharge energies are shown in figure 8.20. It is observed that at 6.2 kJ discharge energy magnetic field produced is maximum which results in largest deformation.

Figure 8.21 shows the resultant velocity obtained at various discharge energies. The measurements are taken at several points as shown in figure 8.21 (a). The velocity increases with the increase of discharge energy. The maximum velocity obtained is 217 m/s at 6.2 kJ discharge energy. The magnetic field generated and velocity both are maximum at 6.2 kJ discharge energy which results in largest deformation, resulting in maximum gap filling.

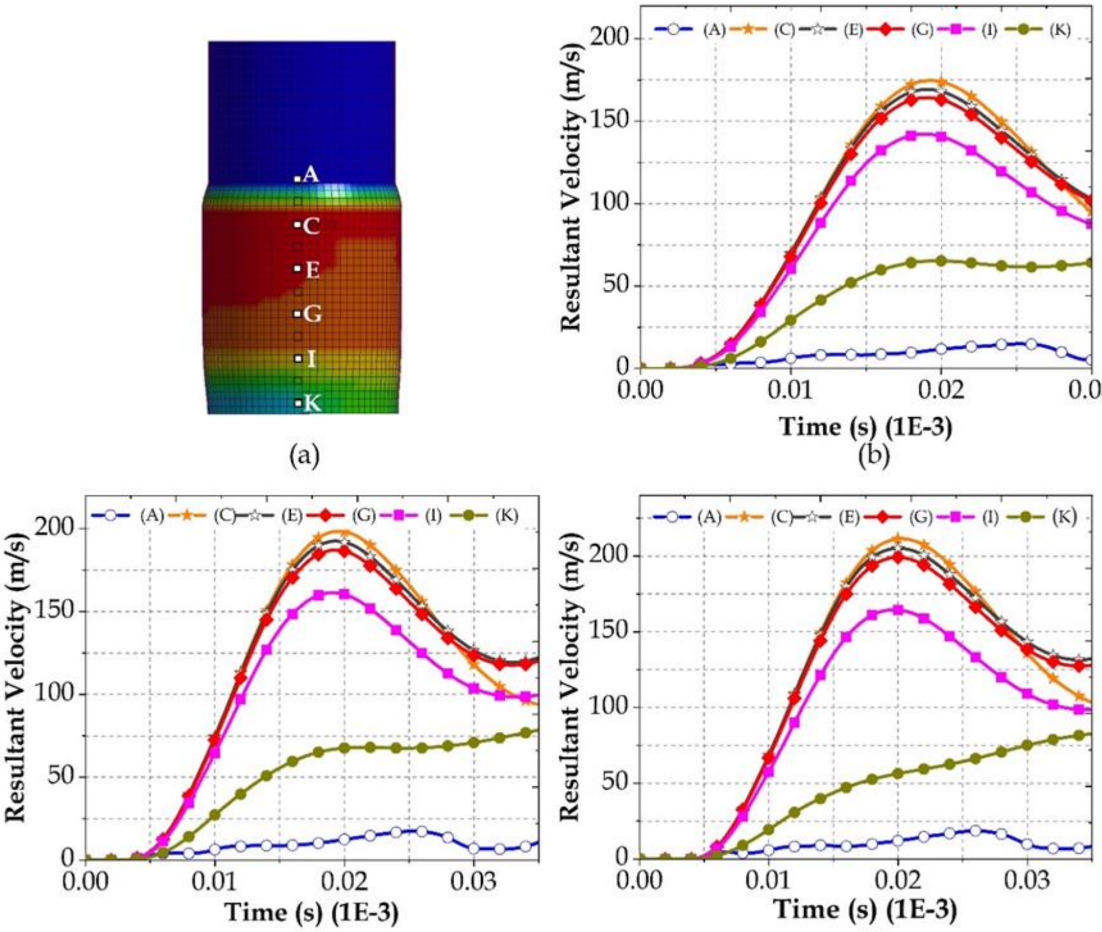

(a) (b) (c) (d)

***Figure 8.21*** *Resultant velocity obtained at various discharge energies (a) Measurement points (b) 5.0 kJ, (c) 5.6 kJ and (d) 6.2 kJ*

### 8.4.4 Formability Analysis

For the formability study, the strain values are measured in two different regions. One is at near to the tube failure (unsafe region), and other is away from the tube failure region (safe region). These strain values are measured on the failure and safe region of 6.5 kJ tube, 6.2 kJ, 5.6 kJ and 5.0 kJ samples. The forming limit separated the safe region from the failure region on a major-minor strain plot. Strains are measured as the percentage change in diameter along the major and minor axes and are plotted in Figure 8.22. These strain values are calculated with the help of equation (7.1) and equation (7.2).

$$\text{Major strain} = \frac{\text{Major axis length } (d_a) - \text{Initial circle diameter } (d_i)}{\text{Initial circle diameter } (d_i)} \tag{7.1}$$

$$\text{Minor strain} = \frac{\text{Minor axis length } (d_b) - \text{Initial circle diameter } (d_i)}{\text{Initial circle diameter } (d_i)} \tag{7.2}$$

Figure 8.22 shows the strain values differentiate the safe and unsafe region by forming limit line. The maximum strain is obtained at the center of the tube. The fracture starts at the center and cracks get propagate towards the end of the tube. The maximum safe major strain is in the range of 34% to 55%, and the maximum minor strain values are in the range of 15% to 41%. The strain values are confined to the biaxial region of forming limit curve. For other discharge energies (6.2 kJ, 5.6 kJ and 5.0 kJ) strain values are lying well below the forming limit line.

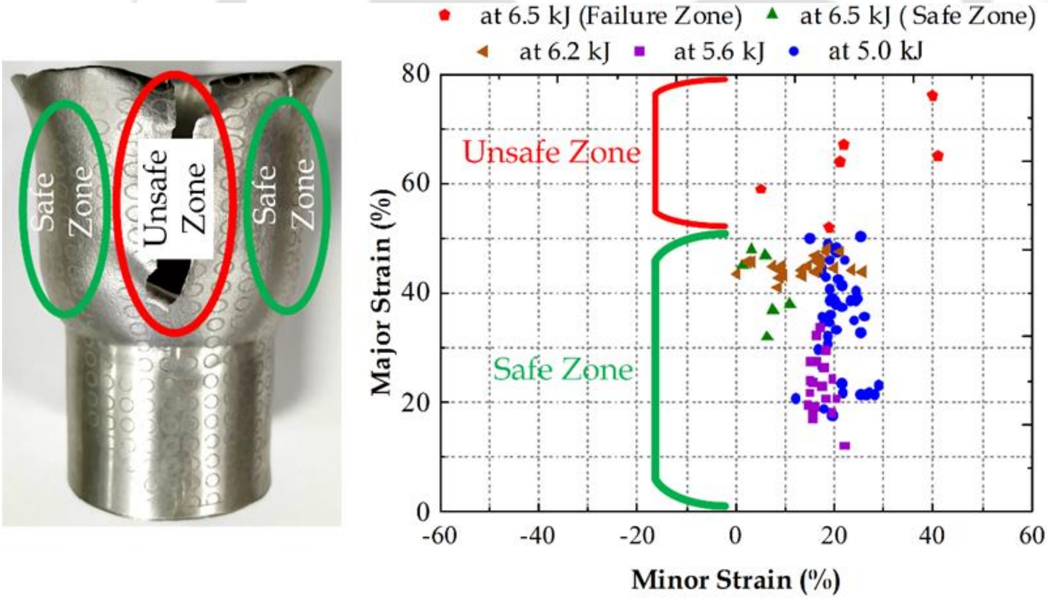

***Figure 8.22** Major and minor strain values*

### 8.4.5 Influence of Discharge Energy on Major Strain and Minor Strain

Figure 8.23 illustrates the effect of discharge energy on the maximum major and minor strain. As the discharge energy increases, the maximum major strain and maximum minor strain increases and it shows the linear relationship before the failure. According to Cheng et al. [55], the Mg content in the alloy results in greater strengthening effect under high strain rate forming. The presence of Mg in aluminum alloy hold back the dislocation motion under high strain rate forming which results in a strengthening of the material.

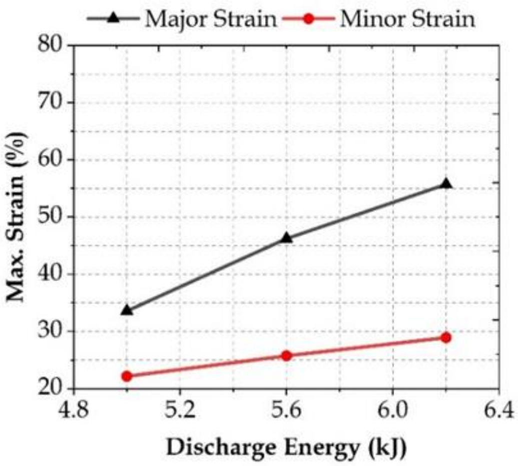

***Figure 8.23*** *The effect of discharge energy on the maximum major and minor strains*

### 8.4.6 Effect of High Strain Rate Forming on the Hardness

Electromagnetic forming is a high strain rate forming. It has some advantages over the conventional forming such as less spring back, less wrinkle formation and strain hardening. EM forming makes material harder and stronger through plastic deformation. To study this effect, Vickers microhardness test has been carried out. The test is carried out at 100 g load with 20 sec dwell time. The measurements are taken along the thickness of the tube, and it is observed that the hardness of the tubes increases after the EM forming because of the strain hardening effect. Figure 8.24 shows the variation of hardness with discharge energies. The hardness of the tube before experiment is 104 HV. There is a 25.23% increase in hardness is observed. The increase in hardness is due to residual strain induced by the high strain rate forming process.

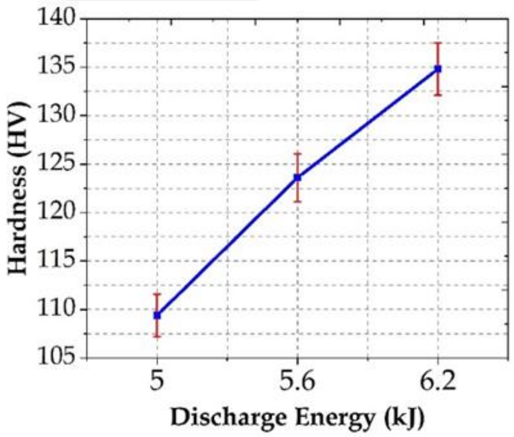

***Figure 8.24*** *Variation of hardness with discharge energy*

### 8.5 Conclusion

i. Lorentz forces drive the EM forming and developed FEM model can easily calculate the Lorentz force generated in the process at various conditions. When the coil is positioned one or two turns out from any end, tube deformation is non-uniform along the length, and the deformation at the end is more than the center deformation. This end effect is because of the maximum magnetic field and hence the maximum Lorentz forces are available at the end of the tube. At 6.2 kJ discharge energy and when coil covers the total length of the tube, generated maximum Lorentz forces covers more region where deformation is required and results in maximum and uniform deformation in the central region compared to other cases.

ii. Radial deformation increases with increase in discharge energy. Almost 96% gap filling is obtained at 6.2 kJ discharge energy. Coupled simulation is developed in LS-DYNA at the same discharge energy. The radial deformation obtained in the simulation is of 95% agreement with experimental results.

iii. The maximum major strain is in the order of 34% to 55%, which shows the increase of formability of material in EM forming. The strain obtained all lower discharge energies are well below the failure strain. The strain values are near to the plane strain region as well as in the biaxial region of forming limit diagram.

iv. After forming, a 25.23% increase in hardness (HV) is observed. Hardness values reveal that the EM forming process increases the hardness of the tube through-thickness direction due to peening effect.

# Chapter 9

# Conclusion and Scope of Future Work

## 9.1 Conclusion

In this thesis, research work is carried out on providing an alternative and effective way to tackle disadvantages being faced by a conventional shearing and forming process. Important conclusions and recommendation from the thesis work are summarised below,

- Feasibility of electromagnetic forming and perforation process has been carried out. This process eliminates the sub operations involved in conventional manufacturing of deformed perforated tube and hence it can be the alternative way of manufacturing of deformed perforated tubes. Along with the shearing of material, strain hardening i.e. strengthening of the tube material is also observed.
- The performed comparison between EM and quasi-static die-less perforation shows that the EM perforation process overcomes various disadvantages of the quasi-static perforation process. Overall, in this novel comparison the holes produced by the EM perforation process with a concave punch are secondary crack free unlike the quasi-static perforation. Also, the edge characteristics show that the EM perforation enhances the edge surface finish compared to conventional process.
- Further the experiments are carried out on EM forming of Al muffler which results in a single piece of component of desired shape, hence eliminates the weld zone to extend the working life of muffler. The formability study shows the strengthening of the material which justifies the use of aluminum for manufacturing of muffler tube.
- As the EM forming and perforation is a novel high strain rate process and it is very difficult to find some parameters experimentally which show the need of development of numerical solutions for the process. Here in this study, a non-coupled and coupled simulation models are developed and numerical results are found almost 96% agreement with experimental finding. It is seen that non-coupled simulation captures initiation of shearing at lower discharge energies and on the other hand coupled simulation results are closer to the experimental finding. So it is suggested that for better physical interpretation non-coupled model can be used, however, for accurate results coupled simulation is preferred.

Overall, the work carried out shows the feasibility of advanced techniques and can replace the conventional processes. Here the developed electromagnetic forming and perforation can be used for manufacturing of the deformed perforated tubes whereas electromagnetic forming of muffler tube can be used for the near net shape manufacturing of muffler tube used in automobiles. The results obtained through developed numerical models are in good agreement with general finding in experiments which shows the prediction capability of developed models. The present study concluded that the EM techniques are advantageous over conventional processes. Finally, by modifying the elements in this study one can commercialize these applications of EM forming processes.

## 9.2 Future Work

### 9.2.1 Electromagnetic Forming and Perforation

The present research confirmed the feasibility of electromagnetic forming and perforation process, opens the door for the future investigators to explore many other aspects regarding development of the process which may allow one to use this process commercially.

- In the present study two types of punches were used namely pointed and concave punch, one can design and develop some other geometries of punches to study the effect of different geometries of punches on the electromagnetic shearing.
- Because of the limitations of the available setup only one material i.e. Al 6061 is used in this study, the future investigator may use other material such as alloy of steel which may have many applications.
- Varieties of deformed perforated tubes are used in the various application like in filter element, exhaust systems etc. Here by changing the die punch arrangement, the present study can be further used for manufacturing of different deformed perforated elements.

### 9.2.2 Electromagnetic Forming of Muffler Tube

The reported study show that the near net shape manufacturing of muffler tube is possible with electromagnetic forming technique. In future the presented study further can be extended by following ways,

- Further the study can be advanced by changing the material die, i.e. by using lower conductivity of the die, the efficiency of the process can be increased.
- Because of the working capacity of available electromagnetic forming machine, the presented study reports the experimental and numerical analysis of only half part

of muffler tube. In future the electromagnetic forming of complete muffler tube can be done.

# List of Publications

- **Award Received**
  - Received **"Gold Award"** in CII Most Innovative Low-Cost Automation (MILCA) AWARD 2020, Organized by *Confederation of Indian Industry (CII)* India, on 29th Dec 2020.

- **International Journals**
  - **Published / Accepted**

1. **Sagar Pawar,** Dinesh Ray, Sachin D. Kore and Arup Nandy (2021). Electromagnetic forming and perforation of tubes: Modeling, simulation and validation. *Journal of Manufacturing Science and Engineering (ASME),* 143(6), 061003.
2. **Sagar Pawar,** Sachin D. Kore and Arup Nandy (2020). Comparison of sheared edge zones developed in electromagnetic and Quasistatic dieless perforation. *Journal of Materials Engineering and Performance*, 21(2), 1-10.
3. **Sagar Pawar,** Ravi Valecha, Sachin D. Kore (2020). Finite element analysis to study the shearing mechanism in punchless electromagnetic perforation of aluminium tubes. *International Journal of Materials and Product Technology*, 60(1), 1-17.
4. **Sagar Pawar,** Sachin D. Kore (2019). Electromagnetic forming and perforation of Al tubes. *Journal of Mechanical Science and Technology*, 33(12), 5999-6007.
5. **Sagar Pawar,** Pravin Ghatule, Sachin D. Kore (2017). Finite element modeling of electromagnetic forming of tractor muffler. *Progress in Industrial Ecology, an International Journal*, 11(3), 269-283.
6. **Sagar Pawar**, Sachin D. Kore and Arup Nandy (2021). Loose coupled simulation method for FEA of electromagnetic forming of muffler. *Journal of The Institution of Engineers (India): Series C,* 102 (1), 1-10.
7. **Sagar Pawar,** Sachin D. Kore and Arup Nandy (2020). FE analysis of effect of variation in coil length and coil-tube relative positions on establishment of magnetic fields and distribution of velocities in electromagnetic forming of muffler tube. *Procedia Manufacturing*, 47, 659-664.
8. Deepak Kumar, **Sagar Pawar**, Sachin D. Kore and Arup Nandy (2020). Comparison of coupled and non-coupled finite element models for joining of Cu-SS tubes by electromagnetic forming. *Procedia Manufacturing*, 47, 673-677.

- **Communicated / Under Review**

9. **Sagar Pawar**, Sachin D. Kore and Arup Nandy. FEM and experimental study on effect of coil-tube overlap distance on die filling during forming of muffler tube. *International Journal of Advanced Manufacturing Technology*. (Under Review)

- **Book Chapters**

1. **Sagar Pawar,** Sachin D. Kore and Arup Nandy (2019). Magnetic pulse forming and punching of al tubes: A novel technique for forming and perforation of tubes. *In Advances in Forming, Machining and Automation* (pp. 67-77). Springer, Singapore.
2. **Sagar Pawar,** Dinesh Ray, Sachin D. Kore and Arup Nandy (2021). Comparison of two different simulation methods for the finite element analysis of electromagnetic forming and perforation (EMFP) of tubes. *In Industry 4.0 and Advanced Manufacturing* (pp. 99-109). Springer, Singapore.
3. **Sagar Pawar**, Sachin D. Kore and Arup Nandy (2021). Recent advancement in electromagnetic forming processes. *In Recent Advances in Mechanical Engineering* (pp. 147-155). Springer, Singapore.

- **Presentations / Conference attended**

1. **Sagar Pawar,** Sachin D. Kore and Arup Nandy (2019). Magnetic pulse forming and punching of al tubes: A novel technique for forming and perforation of tubes, Presented during the 7th International and 28th All India Manufacturing Technology, Design and Research Conference (AIMTDR 2018), *College of Engineering Guindy, Anna University, Chennai, India*, Dec 2018.
2. **Sagar Pawar,** Dinesh Ray, Sachin D. Kore and Arup Nandy (2019). Comparison of two different simulation methods for the finite element analysis of electromagnetic forming and perforation (EMFP) of tubes, Presented during 1st International Conference on Industry 4.0 and Advanced Manufacturing (I4AM'19), *Indian Institute of Science, Bangalore, India, June* 2019.
3. **Sagar Pawar**, Sachin D. Kore and Arup Nandy (2019). Loose coupled simulation method for FEA of electromagnetic forming of muffler. Presented during 7th International Conference on Advancements and Futuristic Trends in Mechanical and Materials Engineering (AFTMME 2019), *Indian Institute of Technology Ropar, Punjab, India*, Dec 2019.
4. **Sagar Pawar**, Sachin D. Kore and Arup Nandy (2020). Recent advancement in electromagnetic forming processes. Presented during International Conference on Recent Developments in Mechanical Engineering (ICRAME 2020), *National Institute of Technology Silchar, Assam, India*, Feb 2020.

5. **Sagar Pawar**, Sachin D. Kore and Arup Nandy (2020). FE analysis of effect of variation in coil length and coil-tube relative positions on establishment of magnetic fields and distribution of velocities in electromagnetic forming of muffler tube. Presented in 1st virtual ESAFORM Conference and 23rd International Conference on Material Forming, Brandenburg *University of Technology (BTU) Cottbus-Senftenberg, Cottbus, Germany,* May 2020.

# References

[1] Mamalis, A. G., Manolakos, D. E., Kladas, A. G., & Koumoutsos, A. K. (2004). Electromagnetic forming and powder processing: trends and developments. Applied Mechanics Reviews, 57(4), 299-324.

[2] Lippmann, H., & Schreiner, H. (1964). On the physics of metal forming with pulsed magnetic fields of high energy. Zeitschrift Fur Metallkunde, 55(12), 737-740.

[3] Psyk, V., Risch, D., Kinsey, B. L., Tekkaya, A. E., & Kleiner, M. (2011). Electromagnetic forming—A review. Journal of Materials Processing Technology, 211(5), 787-829.

[4] Takatsu, N., Masana, K. A. T. O., & Toshimi, T. O. B. E. (1988). High-speed forming of metal sheets by electromagnetic force. JSME International Journal Ser. 3, Vibration, Control Engineering, Engineering for Industry, 31(1), 142-148.

[5] Gayakwad, D., Dargar, M. K., Sharma, P. K., & Rana, R. S. (2014). A review on electromagnetic forming process. Procedia Materials Science, 6, 520-527.

[6] Bay, F., Jeanson, A. C., & Zapata, J. A. (2014). Electromagnetic forming processes: Material behaviour and computational modelling. Procedia Engineering, 81, 793-800.

[7] Oliveira, D. A., Worswick, M. J., Finn, M., & Newman, D. (2005). Electromagnetic forming of aluminum alloy sheet: free-form and cavity fill experiments and model. Journal of Materials Processing Technology, 170(1), 350-362.

[8] Alle Navee kumar and Mashuq-Un-Nabi (2009). Finite element modeling and simulation of electromagnetic forces in electromagnetic forming processes: Case studies using COMSOL Multiphysics. COMSOL Conference Bangalore.

[9] Zhang, H., Murata, M., & Suzuki, H. (1995). Effects of various working conditions on tube bulging by electromagnetic forming. Journal of Materials Processing Technology, 48(1-4), 113-121.

[10] Ghatule P., Kore S. D. (2013) Coupled 3D finite element modeling of electromagnetic free expansion of Al tube, International Journal of Advanced Materials Manufacturing and Characterization, 3(1), 95-98.

[11] Gourdin, W. H. (1989). Analysis and assessment of electromagnetic ring expansion as a high-strain-rate test. Journal of Applied Physics, 65(2), 411-422.

[12] Song, F. M., Zhang, X., Wang, Z. R., & Yu, L. Z. (2004). A study of tube electromagnetic forming. Journal of Materials Processing Technology, 151(1), 372-375.

[13] Shang, J., Hatkevich, S., & Wilkerson, L. (2012). Comparison between experimental and numerical results of electromagnetic tube expansion. In 12th International Ls-Dyna Users Conference,1-10.

[14] Shin, C., Jin, H. H., Lee, J. G., Lee, D. J., Rhee, C. K., & Hong, J. H. (2008). Expansion of a low conductive metal tube by an electromagnetic forming process: finite element modeling. Metals and Materials International, 14(1), 91-97.

[15] Siddiqui, M. A., Correia, J. P., Ahzi, S., & Belouettar, S. (2009). Electromagnetic forming process: estimation of magnetic pressure in tube expansion and numerical simulation. International Journal of Material Forming, 2, 649-652.

[16] Chunfeng, L., Zhiheng, Z., Jianhui, L., Yongzhi, W., & Yuying, Y. (2002). Numerical simulation of the magnetic pressure in tube electromagnetic bulging. Journal of Materials Processing Technology, 123(2), 225-228.

[17] Suzuki, H., Murata, M., & Negishi, H. (1987). The effect of a field shaper in electromagnetic tube bulging. Journal of Mechanical Working Technology, 15(2), 229-240.

[18] Bradley, J. R., Lovell, M. H., Marks, K. R., Kent, T. A., & Cotton, D. W. (2012). U.S. Patent No. 8,099,989. Washington, DC: U.S. Patent and Trademark Office.

[19] Mamalis, A. G., Manolakos, D. E., Kladas, A. G., & Koumoutsos, A. K. (2006). Electromagnetic forming tools and processing conditions: numerical simulation. Materials and Manufacturing Processes, 21(4), 411-423.

[20] Bartels, G., Schaetzing, W., Scheibe, H. P., & Leone, M. (2009). Simulation models of the electromagnetic forming process. Acta Physica Polonica-Series A General Physics, 115(6), 1128.

[21] Vivek, A., Kim, K. H., & Daehn, G. S. (2011). Simulation and instrumentation of electromagnetic compression of steel tubes. Journal of Materials Processing Technology, 211(5), 840-850.

[22] Demir, O. K., Psyk, V., & Tekkaya, A. E. (2010). Simulation of tube wrinkling in electromagnetic compression. Production Engineering, 4(4), 421-426.

[23] Karch, C., & Roll, K. (2005). Transient simulation of electromagnetic forming of aluminium tubes. Advanced Materials Research, Trans Tech Publications, 6, 639-648.

[24] Gharghabi, P., Dordizadeh, P., & Niayesh, K. (2011). Impact of metal thickness and field shaper on the time-varying processes during impulse electromagnetic forming in tubular geometries. Journal of the Korean Physical Society, 59(61), 3560-3566.

[25] Chaharmiri, R., & Arezoodar, A. F. (2017). The Effect of Stepped Field Shaper on Magnetic Pressure and Radial Displacement in Electromagnetic inside Bead Forming: Experimental and Simulation Analyses Using Maxwell and Abaqus Software. Journal of Manufacturing Science and Engineering, 139(6), 061003.

[26] Arezoodar, A. R. F., Garzan, E., Ebrahimi, H., & Crossroad, V. (2012) Effect of various field shapers on magnetic pressure in electromagnetic inward tube forming. Advances in Fluid Mechanics and Heat & Mass Transfer, 1.

[27] Murakoshi, Y., Takahashi, M., Sano, T., Hanada, K., & Negishi, H. (1998). Inside bead forming of aluminum tube by electro-magnetic forming. Journal of Materials Processing Technology, 80, 695-699.

[28] Haiping, Y. U., Chunfeng, L. I., & Jianghua, D. E. N. G. (2009). Sequential coupling simulation for electromagnetic–mechanical tube compression by finite element analysis. Journal of materials processing technology, 209(2), 707-713.

[29] Yu, H. P., & Li, C. F. (2007). Effects of coil length on tube compression in electromagnetic forming. Transactions of nonferrous metals society of China, 17(6), 1270-1275.

[30] Bartels, G., Schätzing, W., Scheibe, H. P., & Leone, M. (2009). Comparison of two different simulation algorithms for the electromagnetic tube compression. International Journal of Material Forming, 2(1), 693.

[31] Min, D. K., & Kim, D. W. (1993). A finite-element analysis of the electromagnetic tube-compression process. Journal of Materials Processing Technology, 38(1-2), 29-40.

[32] Reid, S. R., & Ghosh, S. K. (1981). Piercing of cylindrical tubes. Journal of Pressure Vessel Technology, 103, 255.

[33] Nishida, M., & Tanaka, K. (2006). Experimental study of perforation and cracking of water-filled aluminum tubes impacted by steel spheres. International Journal of Impact Engineering, 32(12), 2000-2016.

[34] Schwer, L. E., & Windsor, C. A. (2009). Aluminum plate perforation: a comparative case study using Lagrange with erosion, multi-material ALE, and smooth particle hydrodynamics. In 7th European LS-DYNA Conference.

[35] Børvik, T., Langseth, M., Hopperstad, O. S., & Malo, K. A. (2002). Perforation of 12mm thick steel plates by 20mm diameter projectiles with flat, hemispherical and conical noses: part I: experimental study. International Journal of Impact Engineering, 27(1), 19-35.

[36] Børvik, T., Hopperstad, O. S., Berstad, T., & Langseth, M. (2002). Perforation of 12mm thick steel plates by 20 mm diameter projectiles with flat, hemispherical and conical noses: part II: numerical simulations. International Journal of Impact Engineering, 27(1), 37-64.

[37] Rusinek, A., Rodríguez-Martínez, J. A., Zaera, R., Klepaczko, J. R., Arias, A., & Sauvelet, C. (2009). Experimental and numerical study on the perforation process of mild steel sheets subjected to perpendicular impact by hemispherical projectiles. International Journal of Impact Engineering, 36(4), 565-587.

[38] Atkins, A. G., & Liu, J. H. (1998). Necking and radial cracking around perforations in thin sheets at normal incidence. International journal of impact engineering, 21(7), 521-539.

[39] Manes, A., Pagani, M., Saponara, M., Mombelli, D., Mapelli, C., & Giglio, M. (2014). Metallographic characterization of Al6061-T6 aluminium plates subjected to ballistic impact. Materials Science and Engineering: A, 608, 207-220.

[40] Backman, M. E., & Goldsmith, W. (1978). The mechanics of penetration of projectiles into targets. International Journal of Engineering Science, 16(1), 1-99

[41] Johnson, G. R., & Cook, W. H. (1983, April). A constitutive model and data for metals subjected to large strains, high strain rates and high temperatures. In Proceedings of the 7th International Symposium on Ballistics, 1983, 541-547.

[42] Teng, X., & Wierzbicki, T. (2006). Evaluation of six fracture models in high velocity perforation. Engineering Fracture Mechanics, 73(12), 1653-1678.

[43] Johnson, G. R., & Cook, W. H. (1985). Fracture characteristics of three metals subjected to various strains, strain rates, temperatures and pressures. Engineering Fracture Mechanics, 21(1), 31-48.

[44] LS-DYNA keyword user's manual, (2007). Livermore Software Technology Corporation. 7374, 354.

[45] L'Eplattenier, P., Cook, G., Ashcraft, C., Burger, M., Imbert, J., & Worswick, M. (2009). Introduction of an electromagnetism module in ls-dyna for coupled mechanical-thermal-electromagnetic simulations. Steel Research International, 80(5), 351-358.

[46] Mamalis, A. G., Manolakos, D. E., Kladas, A. G., & Koumoutsos, A. K. (2005). Physical principles of electromagnetic forming process: a constitutive finite element model. Journal of materials processing technology, 161(1-2), 294-299.

[47] Boldyrev, I. S., Shchurov, I. A., & Nikonov, A. V. (2016). Numerical simulation of the aluminum 6061-t6 cutting and the effect of the constitutive material model and failure criteria on cutting forces prediction. Procedia Engineer, 150, 866-870.

[48] A. S. T. M Standard. (2004). E8 Standard test method for tension testing of metallic materials. West Conshohocken (USA), ASTM.

[49] Kiliclar, Y., Demir, O.K., Engelhardt, M., Rozgić, M., Vladimirov, I.N., Wulfinghoff, S., Weddeling, C., Gies, S., Klose, C., Reese, S., & Tekkaya, A.E. (2016). Experimental and numerical investigation of increased formability in combined quasi-static and high-speed forming processes. Journal of Materials Processing Technology, 237, 254-269.

[50] Schwer, L.E., & Windsor, C.A. (2009). Aluminum plate perforation: a comparative case study using Lagrange with erosion, multi-material ALE, and smooth particle hydrodynamics. In 7th European LS-DYNA conference, 28.

[51] Garrison, W. M., & Moody, N. R. (1987). Ductile fracture, Journal of Physics and Chemistry of Solids, 48(11), 1035-74.

[52] Golowin, S. M. (2008). Path Actuators for Magnetic Pulse Assisted Forming and Punch-less Electro-Magnetic Shearing (Doctoral dissertation, The Ohio State University).

[53] Tekiner, Z., Nalbant, M., & Gürün, H. (2006). An experimental study for the effect of different clearances on burr, smooth-sheared and blanking force on aluminium sheet metal. Materials & design, 27(10), 1134-1138.

[54] Hertzberg, R. W. (1997). Deformation and fracture mechanics of engineering materials. Journal of Materials Education, 19, 227-232.

[55] Cheng, J., & Nemat-Nasser, S. (2000). A model for experimentally-observed high-strain-rate dynamic strain aging in titanium. Acta materialia, 48(12), 3131-3144.

[56] Qiu, L., Han, X., Peng, T., Ding, H., Xiong, Q., Zhou, Z., Jiang, C., Lv, Y., & Li, L. (2012). Design and experiments of a high field electromagnetic forming system. IEEE Transactions on Applied Superconductivity, 22, 3700504.

[58] Ozturk, F., Sisman, A., Toros, S., Kilic, S., & Picu, R. C., (2010). Influence of aging treatment on mechanical properties of 6061 aluminum alloy. Materials and Design, 31(2), 972-975.

[59] Meguid, S. A., & Sun, Y. (2004). On the tensile and shear strength of nano-reinforced composite interfaces. Materials and Design, 25(4), 289-296.